ABSTRACT

Surface quality problems in continuous cast steel are greatly affected by heat transfer across the interfacial layers in the gap between the solidifying steel shell and the mold. A quantitative understanding of heat transfer mechanisms within the interfacial gap is essential for maintaining high levels of quality in continuous-cast steel slabs. A mathematical model has been developed to simulate heat transfer within the continuous casting mold. A detailed description of the interface between shell and mold has been integrated into the CON1D mathematical model to simulate the transient behavior of the interfacial region as the steel solidifies. In order to apply the interface model to actual casting conditions, experiments have been performed to quantify the thermal characteristics of common mold powders. Thermal properties of the tested mold powders are calculated from both conduction and conduction-plus-radiation mathematical models which were applied to the experimental data. Measurements of shell growth were obtained from an intact breakout shell, which were used to compare against predictions from the CON1D mathematical model. A complete documentation is provided of the mold geometry, casting conditions, and derived solidification time as a function of distance down the breakout shell. Mold temperatures and cooling water temperature increase were measured for similar casting conditions using a mold instrumented with 106 thermocouples. Microstructures are presented which show the dendrites and both primary and secondary arm spacing measurements are included. The final grain structure is presented for several different macro-etched sections. Matching the solidification times of individual shell locations produced good correlations between model predictions and shell measurements.

TABLE OF CONTENTS

Page

LIST OF TABLES

LIST OF FIGURES

NOMENCLATURE

a	Flux absorption coefficient (m^{-1})
Bi	Biot number (-)
C_p	Specific Heat (J/kg-K)
C_p^*	Effective Specific Heat (J/kg-K)
d	Distance (m)
d_m	Mold copper thickness (m)
d_{osc}	Effective mark thickness (volume)
d_s, d_l	Thickness of solid, liquid flux layers (m)
d_{oeff}	Effective osc. mark depth (mm) (thermal)
d_{mark}	Max. osc. mark depth (mm)
f	fraction (-)
f_s	Solid fraction for shell thickness location (-)
g	Gravity (ms^{-2})
h	Convection heat transfer coefficient ($Wm^{-2}K^{-1}$)
H	Total interface thickness (m)
k	Thermal conductivity ($Wm^{-1}K^{-1}$)
K_{mark}	Oscillation mark conductivity ($Wm^{-1}K^{-1}$)
K_f	Conductivity of rest of gap ($Wm^{-1}K^{-1}$)
K_r	Radiative gap conductivity ($Wm^{-1}K^{-1}$)
L_{mark}	Width of oscillation marks (mm)
L_{pitch}	Ratio of casting speed to oscillation frequency (mm)

m	Power-law exponent for flux viscosity (-)
n	Flux refractive index (-)
N	Slab thickness (m)
P	Pressure (MPa)
Pr	Prandtl number (-)
$\dot{q}$, Q	Heat flux (W/m^2)
Q_f	Mold flux consumption ($kg\ m^{-2}$)
Q_w	Secondary cooling zone water flux ($l\ m^{-2}s^{-1}$)
R	Interface resistance ($m^2\ K\ W^{-1}$)
R_o	Mold outer radius (m)
Re	Reynolds number (-)
St	Stokes number (-)
Ste	Stefan number (-)
t	time (s)
T	Temperature (K)
T_{Cu}	Mold surface temperature (ßC)
T_{Fe}	Steel surface temperature (ßC)
T_{fsol}	Flux solidification temperature (ßC)
V_c , S	Casting speed ($m\ s^{-1}$)
V_l	Liquid flux velocity ($m\ s^{-1}$)
V_s	Solid flux velocity ($m\ s^{-1}$)
W	Slab width (m)

z_{mold}	Working mold length (m)
α	Heat transfer coefficient ($Wm^{-2}K^{-4}$)
δ	Position of solidification front (m)
θ	Non-dimensional temperature (-)
μ	Viscosity ($kg\ m^{-1}s^{-1}$)
ρ	Density ($kg\ m^{-3}$)
σ	Stefan Boltzman constant ($Wm^{-2}K^{-4}$)
ε_{Fe}, ε_{Cu}	Steel, mold surface emissivities (-)

Subscripts

1	Thermocouple set 1
2	Thermocouple set 2
air	Air gap
C	Copper thermocouple near cold face
cold	Cold-side
cond	Conductive
cr	Chromium
Cu	Copper
eff	effective
Fe	Steel
f, flux	Flux
G	Gap
gap	Pertaining to gap
H	Copper thermocouple near hot face

hot	Hotface
hotc	Hotface copper surface
I, int	Interface
l, liq	Liquid
m, mold	Mold
mi	Inner mold radius
mo	Outer mold radius
mprime	Interface between mold-side flux layer and the air gap between the mold and flux layer
ni	Nickel
poly	Polynite
rad	Radiative
s, steel, shell	Steel shell
scale	Scale layer in water channel
slag	Flux film
sol	Solid
spray	Secondary cooling zone water spray
total	Total
water	Cooling water

1 INTRODUCTION

Over 80% of the steel produced in North America is through continuous casting. Figure 1.1 [1] shows a schematic of the process. Molten steel is poured from a ladle into a tundish, which controls the flow of the steel into the caster. Primary solidification is achieved by contact with a water-cooled copper mold, which oscillates in order to prevent the steel from sticking to the mold. Heat is transferred from the molten steel to the mold to obtain a thin shell, strong enough to support the rest of the liquid after the strand exits the mold. After the mold, the steel is drawn through a series of support rolls and air-mist sprays in a region called the secondary cooling zone. It is here that the steel strand undergoes straightening. Once the strand is flat, torches cut the steel into sections. These sections are then sent through a series of rolling processes to obtain a certain shape that can be sold.

1.1 Importance of Mold Heat Transfer in Continuous Casting

A key mechanism in initial shell solidification is the heat transfer within the mold. Figure 1.2 [2] is an enlarged drawing showing an instance of time when the steel shell is solidifying. The rate and uniformity of heat transfer within the mold are key variables to maintaining high product quality. Frequent variations in heat transfer can occur within the mold region if process variables, such as taper, water velocity and temperature, are not kept in control. Typical variations include reduced heat transfer in mold corners (due to 2-D effects caused by thermal contraction of the shell) and heat transfer increase/decrease due to inadequate mold taper. These phenomena can lead to surface and subsurface defects, as well as contributing to costly breakouts. Thus, a quantitative understanding of mold heat transfer is essential to sustaining high product quality and competitive advantages within the steel industry.

In comparing all the possible mechanisms for heat transfer within the mold region (which include conduction through the solidified shell and convection within the liquid pool), the most dominant is heat transfer across the gap formed between the copper mold and the solidifying shell [3]. This gap is filled with a material, called mold flux, which is designed to aid in strand heat transfer and lubrication. Mold flux is added as a powder to the top surface, where it insulates the molten steel from both heat loss and contamination by the atmosphere. The powder sinters and melts to form a layer of liquid that floats on the surface of the molten steel. The liquid flux then infiltrates into the gap between the solidifying steel shell and the mold walls. Here it acts as a lubricant to prevent sticking of the shell to the mold. It also controls the rate of heat conduction across the interfacial gap that in turn governs heat removal from the shell.

Heat transfer across the interfacial gap greatly affects steel quality. For example, the lower heat transfer rate near the meniscus associated with high-solidification-temperature mold fluxes improves the surface quality of crack-sensitive peritectic (0.1-0.2%C) steel grades [4] and reduces longitudinal cracks. [5] The uniformity of this initial heat transfer rate, as well as its magnitude, is very important [6, 7]. Non-uniform heat transfer generates thermal stresses in the shell, which are worsened by differences in thermal contraction of δ austenite and γ ferrite. This produces non-uniform shell growth, which leads to a variety of quality problems including deep oscillation marks (and subsequent transverse cracks), localized hot, weak regions which concentrate strain and form longitudinal cracks, and surface shape problems such as rhomboidity [8]. In the extreme, breakouts may occur when the tapers of the mold walls do not match the shell shrinkage. Insufficient taper (related to unexpectedly high heat transfer) might cause an air gap, where regions of the shell become too weak to support the liquid pool below the mold. Excessive taper, (related to unexpectedly low heat transfer), may cause jamming of the shell in the mold. These problems are best avoided by understanding and controlling heat transfer across the interfacial gap.

1.2 Plant Observations

Depending on the powder properties and casting conditions, liquid mold flux can solidify into a crystalline or glassy solid phase. In the crystalline phase, the solid contains microcracks and bubbles. Through this crystalline flux layer, heat transfer occurs primarily through conduction mechanisms. In the glassy phase, the solid can radiate energy due to it being free of the refractive defects that the crystalline phase has, and heat is transferred through both conduction and radiation mechanisms. Usually, the thermal conductivities of crystalline phases are higher than those of glassy phases due to increased defects in the prior phase. The percentages of these phases present in the gap between the solidifying shell and copper mold, along with any air gaps that may be present due to inadequate mold taper, control the heat transfer which is dominant in initial solidification.

1.3 Importance of Studying Mold Heat Transfer

There are numerous variables that directly influence heat transfer mechanisms within the mold. Casting variables that have been studied include casting speed, frequency of mold oscillation, SEN design, and mold geometry. Steel chemistry has also been analyzed as to its effect on heat transfer, as is the case with peritectic-grade steels. However, in general, mold heat transfer is greatly dependent on variables that define the gap between the mold and steel shell. Mold powder properties play a major role in defining this gap.

Selecting the correct mold flux powder composition and properties is essential in order to prevent defect formation. Air gaps may form if all the liquid flux solidifies in the mold and the mold taper does not match the shrinkage of the steel shell. Air gaps severely hinder heat transfer due to air s low conductivity. These gaps can lead to irregular shell growth and possible breakouts. Also, high heat fluxes near the meniscus can be suppressed depending on the conductive and radiative properties of the mold flux powder. Thus, in order to achieve high confidence in any continuous casting process utilizing mold powders, the thermal behavior of mold powders and their influence on interfacial heat transfer must be thoroughly understood.

1.4 Previous Studies in Interface Modeling

Several models have been developed in an attempt to model the heat transfer between the shell and the mold. Jenkins [3] developed a mathematical model of the interface region that includes conduction and radiation effects. The model characterizes the slag film as a series of flux layers, and are modeled as individual nodes of constant temperature. The model assumes that the steady-state flux absorptivity and emissivity are equal, and all non-absorbed radiation is transmitted through the layer. These assumptions allow for the resistances associated with emission, absorption and transmission through the slag layers to be expressed only as a function of slag emissivity. All nodes in the model can interact through radiation, but only adjacent nodes can interact through conduction. Jenkins concluded that uncoupled interaction between radiation and conduction heat transfer underestimates the heat flux by less than 10% for intermediate optical thicknesses.

Hiraki [9] developed a lubrication model to characterize the flux film behavior and its effect on longitudinal surface cracking in high speed slab casting. The model accounted for mold oscillation and its effect on liquid flux supply to the interfacial gap. Increases in mold powder melting temperature, as well as decreasing the amplititude of oscillation stroke, was shown to decrease powder consumption and increase the occurrence of longitudinal crack formation.

Bommaraju [10] developed a mathematical model of the mold flux film and its effect on heat transfer between the shell and the mold. Radiation heat transfer through the liquid flux layer is neglected in this model. Shear and normal stresses on the flux film and steel shell are calculated by assuming Couette flow of the liquid flux between the mold and the steel. Solid-solid friction between the shell and flux film is assumed when the flux temperature drops below its solidification point. Flux film contraction is not accounted for, as air gaps due to oscillation marks and flux solidification are neglected.

DiLellio [11] modeled the mold flux region based on a lubrication approximation. Conduction-dominated temperature fields in the mold, flux film, shell and liquid steel were derived from an evolution equation for the progression of the shell s solidifying front. The interface model assumed a temperature-dependent viscosity of the mold flux, and allowed for flux solidification below its solidification temperature. Parametric studies were performed to observe system responses to changing casting speeds, nozzle superheat flux input, mold temperatures and mold powder properties.

1.5 Objectives of Work

Mathematical models can increase our understanding of interfacial heat transfer in continuous casting, and help to determine how to avoid and minimize problems and defects in the casting process. The objective of this work is to achieve the following:

- Develop a mathematical model of interfacial heat transfer in the continuous casting process. The model will be validated by comparison with the analytical solution.

- Laboratory experiments will be conducted to simulate the conditions experienced by the liquid mold flux in the mold/steel gap, near the meniscus, in the continuous casting process. Data from these experiments will be used to characterize the thermal properties of the mold flux used during the casting of the breakout shell. This data will be used to compare the experimental measurements with actual data, obtained form mold thermocouple measurements.
- The mathematical model will be used to predict the shell growth of a continuous-cast thin slab that was cast during a breakout condition. Heat transfer rates, taken from a similar casting run, and determined from thermocouple measurements from the copper mold, will be used to predict the shell growth. Predicted values of shell growth will be compared with actual breakout shell measurements for model calibration.
- Applicability of the mold flux experimental data will be evaluated with respect to future mathematical modeling efforts.

The effort in this research is a critical first step in analyzing the effects of mold flux on the final cast product. To further improve quality and decrease cost, a quantitative fundamental understanding of heat transfer in the continuous casting process is essential.

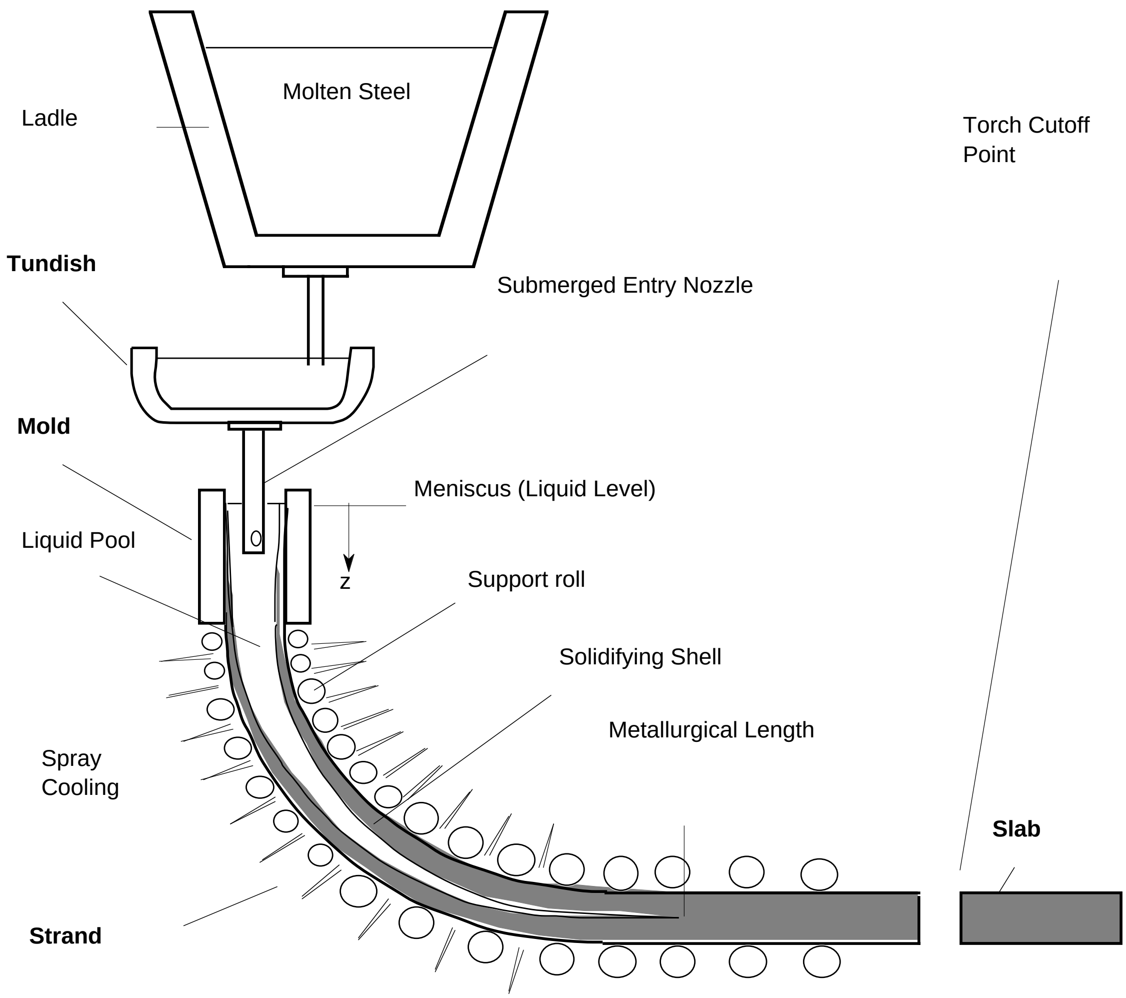

Figure 1.1: Schematic of Continuous Casting Process [1]

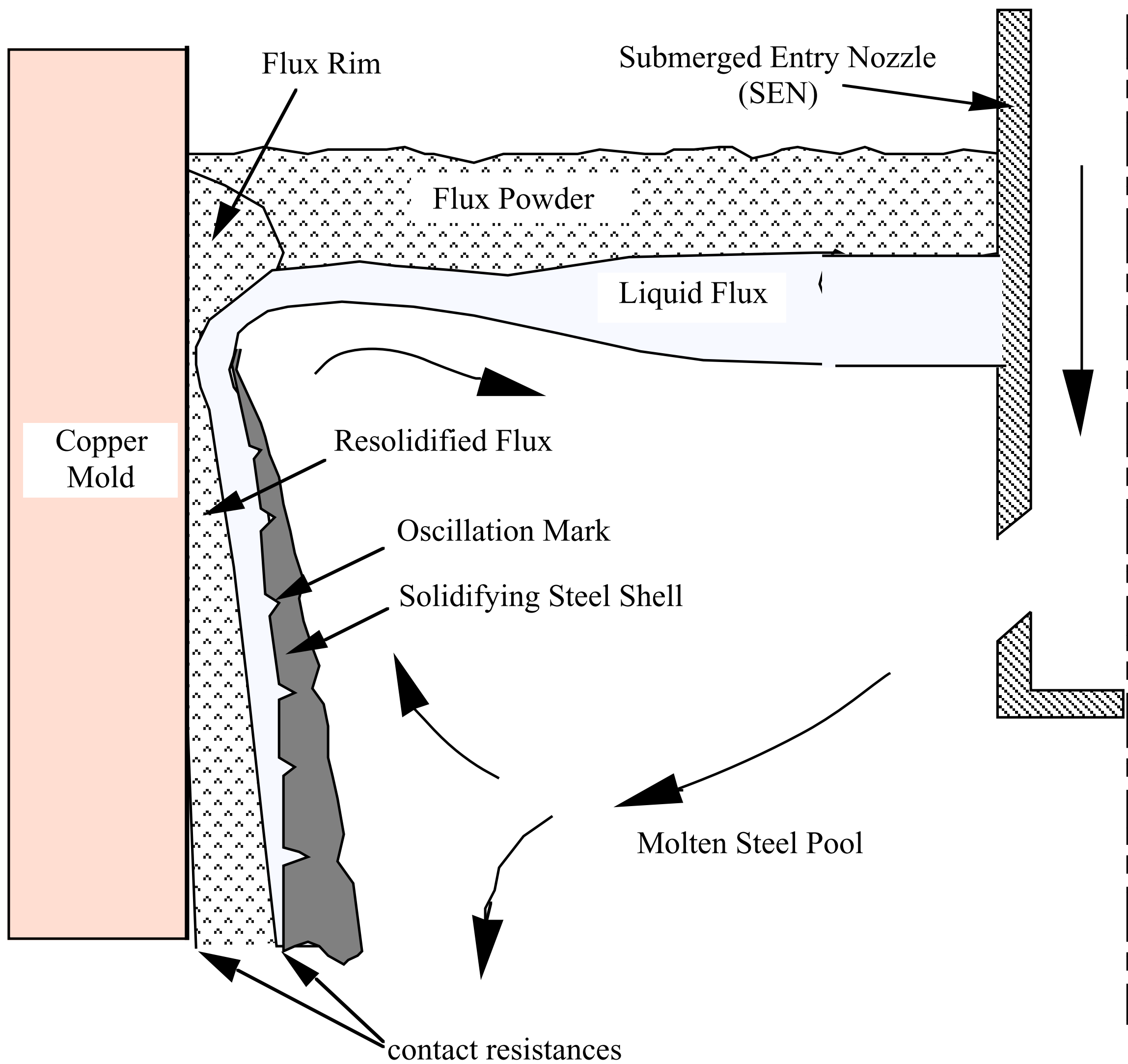

Figure 1.2: Schematic of Meniscus Region of Continuous Caster, illustrating Mold Flux Function in Initial Solidification [2]

2 MODEL FORMULATION: CON1D

Numerical models allow for complex equations, which can be dependent on several variables, to be evaluated in a relatively quick and efficient manner. Heat transfer within the continuous casting mold is a function of numerous parameters, which deal with product composition and shape, process parameters, and mold powder properties. Within the scope of this work, an established in-house numerical model named CON1D has been improved to include new submodels of steel and mold flux behavior. The improved model will be used to evaluate mold heat transfer during a breakout condition, and the results will be compared with plant measurements.

2.1 Description of Model

The CON1D numerical model was developed by Ho and Thomas [12] to model heat transfer and solidification within the continuous casting process. A copy of an example input file is provided in Appendix A. CON1D integrates several heat transfer submodels, which attempt to simulate the system s overall thermal performance. Figure 2.1 illustrates the functionality of CON1D: by inputting process parameters which are usually defined (such as mold geometry, steel properties, casting variables), the model provides several outputs such as:

- Temperatures: mold hot face, cold face, shell surface and shell interior, cooling water
- Shell thickness (including positions of liquidus, solidus, and shell isotherms);
- Heat flux leaving the shell (across the interfacial mold / shell gap);
- Ideal mold taper (based on 1D shrinkage calculations), and
- Thickness and velocity of solid and liquid flux layers in the mold/shell interfacial gap.

The following description of CON1D is an abridged form of information within the program s user manual. Further details on the equations and/or their derivation may be found in the user manual.

2.2 Mathematical modeling of Heat Transfer within CON1D

Heat transfer occurs in four main regions within the continuous casting process: the solidifying steel shell, the water-cooled copper mold, the interface between the shell and mold, and in the secondary cooling zone below the mold.

2.2.1 Heat Transfer within the Solidifying Steel Shell

The temperature within the solidifying shell is governed by the 1-D transient heat conduction equation:

$$\rho C_p^* \frac{\partial T}{\partial t} = \nabla(k\nabla T) = k\frac{\partial^2 T}{\partial x^2} + \frac{\partial k}{\partial T}\left(\frac{\partial T}{\partial x}\right)^2 \qquad (2.1)$$

In the above equation, C_p^*, the effective specific heat for the solidifying steel, is defined as:

$$C_p^* = \frac{dH}{dT} = C_p - \Delta H_L \frac{df_s}{dT} \qquad (2.2)$$

In CON1D, the solid fraction f_s is assumed to vary linearly between the steel s solidus and liquidus temperatures, such that:

$$C_p^* = C_p + \frac{\Delta H_L}{T_{liq} - T_{sol}} \qquad (2.3)$$

Equation 2.1 is applied to the simulation domain, which includes a 1-D slice through the liquid and solid steel. This domain is shown graphically in Figure 2.2[12]. Thermophysical properties of both carbon and stainless steels are available in CON1D, which also allows for user-defined properties to be used.

2.2.1.1 Superheat Input to Steel Domain

Typically, liquid steel enters the mold area at a temperature that is higher than its liquidus temperature. In order to start solidifying, the liquid steel must first cool to its liquidus temperature and, thus, dissipate its superheat energy. Turbulent convection within the liquid steel distributes this energy in a non-uniform manner. CON1D provides two options to the user for modeling superheat dissipation: through user-input data or from a small database collected from an independent 3-D fluid flow model. This database is used to determine the heat flux delivered to the solid / liquid interface due to the superheat dissipation, as a function of distance below the meniscus, q_{sh}. An example of this function is shown graphically in Figure 2.3[12], which represents results for a typical bifurcated, downward-directing nozzle. User-defined values for superheat input have been modeled for complex geometries, such as the ARMCO nozzle [13] that was used in a breakout event. CON1D dissipates this superheat energy and imposes an initial temperature boundary condition on the inside surface of the steel shell, which is the liquidus temperature.

2.2.2 Heat Transfer within the Mold

Heat transfer within the continuous casting mold occurs by conduction through the mold and any coatings, and through convection to the cooling water. By knowing the heat fluxes into the water-side cold face of the mold (q_{cold}), the mold/steel interface (q_{int}), and the effective heat transfer coefficient to the cooling water (h_{water}), temperatures throughout the mold can be calculated. Several models are incorporated to simulate heat transfer within the different regions of the mold, which are shown in Figure 2.4[12].

2.2.2.1 Heat Transfer near the Meniscus

A two dimensional, steady state temperature distribution within a rectangular section through the mold is calculated in the upper portion of the mold. By assuming constant thermal conductivity in the upper mold and constant heat transfer coefficient between the mold cold face and the water channel along the casting direction, the heat conduction equation for mold temperature modification in the meniscus region is the following Laplace equation:

$$\frac{\partial^2 T}{\partial x^2} + \frac{\partial^2 T}{\partial z^2} = 0 \qquad (2.4)$$

The solution methodology to this equation, with boundary conditions representative of a continuous caster, is provided in the CON1D user manual. To account for any mold coatings, the following equation is used to adjust the mold hot face temperature (T_{hot}) calculations:

$$T_{hot} = T(d_m, z) + q_{int}\left(\frac{d_{ni}}{k_{ni}} + \frac{d_{cr}}{k_{cr}} + \frac{d_{poly}}{k_{poly}} + \frac{d_{air}}{k_{air}}\right) \qquad (2.5)$$

2.2.2.2 Mold Heat Transfer below the Meniscus Region

Below the 2-D meniscus region, signified by the value of the zana variable (usually around 50mm), heat transfer within the mold is simulated by using a one-dimensional model. The temperatures of the hotface, copper surface (T_{hotc}) are calculated knowing the copper thickness (d_m), water-side heat transfer coefficient (h_{water}) , and the heat flux at the mold/flux interface (q_{int}) through:

$$T_{hotc} = T_{water} + q_{int}\left(\frac{1.}{h_{water}} + \frac{d_m}{k_m}\right) \qquad (2.6)$$

Other mold temperatures of interest include the temperature of the outermost mold coating (T_{hot}) and the temperature at the interface between the mold-side solid flux layer and the air gap between the mold and the flux layer (T_{mprime}). These temperatures are calculated using mold coating/air gap data in the input file, and the following equations:

$$T_{hot} = T_{water} + q_{int} \left(\frac{1.}{h_{water}} + \frac{d_m}{k_m} + \frac{d_{ni}}{k_{ni}} + \frac{d_{cr}}{k_{cr}} + \frac{d_{poly}}{k_{poly}} \right) \qquad (2.7)$$

$$T_{mprime} = T_{water} + q_{int} \left(\frac{1.}{h_{water}} + \frac{d_m}{k_m} + \frac{d_{ni}}{k_{ni}} + \frac{d_{cr}}{k_{cr}} + \frac{d_{poly}}{k_{poly}} + \frac{d_{air}}{k_{air}} \right) \qquad (2.8)$$

Within the above equations, CON1D varies the mold copper thickness d_m as a function of the mold s curvature, by:

Outer radius: (2.9)

$$d_m = (d_{mo} - d_{ch}) + \sqrt{R_o^2 - \left(\frac{z_{mold}+z_{men}}{2}\right)^2} - \sqrt{R_o^2 - \left(\frac{z_{mold}+z_{men}}{2}\right)^2 - (z+z_{men})^2}$$

Inner radius: (2.10)

$$d_m = (d_{mI} - d_{ch}) - \sqrt{R_I^2 - \left(\frac{z_{mold}+z_{men}}{2}\right)^2} + \sqrt{R_I^2 - \left(\frac{z_{mold}+z_{men}}{2}\right)^2 - (z+z_{men})^2}$$

To calculate the temperature at the root of the water channel (or at the interface between the water channel and possible scale layers), CON1D utilizes the following equation which is dependent on the water-side heat transfer coefficient and the interfacial heat flux:

$$T_{cold} = T_{water} + \frac{q_{int}}{h_{water}} \qquad (2.11)$$

2.2.2.3 Heat Transfer within the Mold Cooling Water Channels

Figure 2.5[12] shows a schematic of the mold where cooling water serves to remove heat from the mold. CON1D determines an effective heat transfer coefficient between the cooling water and water-side mold cold face through:

$$h_{water} = \frac{1}{\frac{d_{scale}}{k_{scale}} + \frac{1}{h_{fin}}} \qquad (2.12)$$

which accounts for scale buildup within the water channels. In this equation, h_{fin} is the heat transfer coefficient between the mold-side mold cold face and cooling water. This coefficient is derived by treating the sides of the water channels as fins, and calculated from the following equation:

$$h_{fin} = \frac{1}{L_{ch}} * \sqrt{2h_w * k_m * (L_{ch} - w_{ch})} * \tanh\left[\sqrt{\frac{2h_w*(d_{m1} - d_{ch})}{k_m*(L_{ch} - w_{ch})}}\right] + \frac{h_w*w_{ch}}{L_{ch}} \qquad (2.13)$$

As shown above, the heat transfer coefficient between the cooling water and the water channel, h_w, is needed to calculate h_{fin}. This coefficient is calculated through use of the Sleicher-Rouse correlation [14], which is derived for turbulent flow through a pipe:

$$h_w = \frac{k_{water}}{D}\left(5 + 0.015\, Re^a\, Pr^b\right) \qquad (2.14)$$

where D is the equivalent diameter of the water channel, and a and b are empirical constants:

$$D = \frac{4 w_{ch} d_{ch}}{2(w_{ch} + d_{ch})} \qquad (2.15)$$

$$a = 0.88 - \frac{0.24}{4 + Pr} \qquad (2.16)$$

$$b = 0.333 + 0.5\, e^{-0.6\, Pr} \qquad (2.17)$$

$$Re = \frac{\rho_{water}\, v_{water}\, D}{\mu_{water}} \qquad (2.18)$$

$$Pr = \frac{\mu_{water}\, Cp_{water}}{k_{water}} \qquad (2.19)$$

Water properties are evaluated at the film temperature, which is half-way between the water and mold wall temperatures. Temperature changes within the mold cooling water is calculated by:

$$\Delta T_{cooling\ water} = \sum_{mold} \frac{q_{int} \cdot V_c \cdot \Delta t \cdot L_{ch}}{\rho_{water} \cdot Cp_{water} \cdot V_{water}(m/s) \cdot w_{ch} \cdot d_{ch}} \quad (2.20)$$

where V_c is the casting speed.

2.2.3 Heat Transfer across Mold/Steel Interface

Heat extraction from the continuous casting mold is controlled primarily by heat transfer across the mold/steel interface. Figure 2.6 [12] illustrates the temperature profiles that CON1D calculates across this interface. Energy transfer within this interfacial regions is comprised of radiation across any liquid flux layers present, conduction across the solid flux layer, conduction across any material within the shell s oscillation marks, and conduction across the shell/flux and flux/mold contact resistances (comprised mostly of air).

2.2.3.1 Mathematical Derivation of Interface Heat Transfer Model

An estimation/scaling analysis of the mass, momentum and energy conservation equations may be performed to better understand the phenomena occurring in the interfacial gap. In order to model this gap, the velocity distribution of the mold flux powder must be determined. Figure 2.7 [12] shows a sketch describing the problem. Table 2.1 provides generic material properties of mold powders and mold materials that are representative of this system. It is assumed that this is a two-dimensional problem (no variation across the mold faces in the y-direction), therefore only references to the x and z directions will be made in the governing equations.

2.2.3.1.1 Scaling of the Flux Continuity Equation

The continuity equation (for constant density) in two-dimensional form is:

$$\nabla \bullet \vec{V} = 0 \qquad (2.21)$$

$$\frac{\partial V_x}{\partial x} + \frac{\partial V_z}{\partial z} = 0 \qquad (2.22)$$

Defining non-dimensional parameters:

$$V_x^* = \frac{V_x}{V_c} \qquad (2.23)$$

$$V_z^* = \frac{V_z}{V_c} \qquad (2.24)$$

$$x^* = \frac{x}{H} \qquad (2.25)$$

$$z^* = \frac{z}{L} \qquad (2.26)$$

, where V_c is the casting speed, H is the thickness of the flux layer, and L represents the length of the mold. Substituting these non-dimensional parameters into Equation 2.22 gives:

$$\frac{V_c}{H}\frac{\partial V_x^*}{\partial x^*} + \frac{V_c}{L}\frac{\partial V_z^*}{\partial z^*} = 0 \qquad (2.27)$$

Comparing the constants multiplying the non-dimensional derivatives shows that the x-components are much more dominant than the z-component since H<< L. Thus the non-dimensional mass conservation equation can be reduced to:

$$\frac{\partial V_x^*}{\partial x^*} = 0 \qquad (2.30)$$

2.2.3.1.2 Scaling of the Momentum Conservation Equations

The 2-D momentum conservation equations, assuming constant density, are:

$$\rho\left(\frac{\partial V_x}{\partial t} + V_x\frac{\partial V_x}{\partial x} + V_z\frac{\partial V_x}{\partial z}\right) = -\frac{\partial P}{\partial x} + \mu\left(\frac{\partial V_x}{\partial x} + \frac{\partial V_x}{\partial z}\right) + \rho g_x \quad (2.31)$$

$$\rho\left(\frac{\partial V_z}{\partial t} + V_x\frac{\partial V_z}{\partial x} + V_z\frac{\partial V_z}{\partial z}\right) = -\frac{\partial P}{\partial z} + \mu\left(\frac{\partial V_z}{\partial x} + \frac{\partial V_z}{\partial z}\right) + \rho g_z \quad (2.32)$$

Since H << L, a lubrication approximation can be made, resulting in the x-direction momentum equation reducing to:

$$\frac{\partial P}{\partial x} = 0 \qquad (2.33)$$

Additional non-dimensional parameters need to be defined in order to scale the z-direction momentum equation. These are:

$$t^* = \frac{t}{L/V_c} \qquad (2.34)$$

$$\mu^* = \frac{\mu}{\mu_o} \qquad (2.35)$$

In these parameters, L/V_c represents a characteristic time within the continuous casting mold. The variable μ_o represents a characteristic viscosity of the mold powder at a given temperature (usually 1300 °C). In CON1D s interface model, the mold powder s viscosity is modeled by a power-law relationship:

$$\mu = \mu_o \left(\frac{T_o - T_{fsol}}{T - T_{fsol}} \right)^m \qquad (2.36)$$

Substituting these non-dimensional parameters into Equation 2.32 gives:

$$\frac{\rho_f V_c H^2}{\mu_0 L} \left(\frac{\partial V_z^*}{\partial t} + v_x^* \frac{\partial V_z^*}{\partial x^*} + v_z^* \frac{\partial V_z^*}{\partial z^*} \right) = \frac{H^2 P_c}{\mu_0 V_c L} \left(-\frac{\partial p^*}{\partial z^*} \right)$$

$$+\mu^* \frac{\partial V_z^*}{\partial x^*} + \frac{H^2}{L^2} \mu^* \frac{\partial V_z^*}{\partial z^*} + \frac{\rho_f H^2 g_z}{\mu_0 V_c} \qquad (2.37)$$

To evaluate the significance of the individual terms in this equation, the values of their respective non-dimensional constants must be calculated:

$$\frac{H^2}{L^2} = \frac{(0.001)^2}{(1.2)^2} = 6.94E^{-7}$$

$$\frac{\rho_f V_c H^2}{\mu_0 L} = \frac{2700 * 1.143 * (0.001)^2}{0.4 * 1.2} = 0.0064$$

$$\left(\frac{H^2}{\mu_0 V_c L}\right)^{-1} = P_c = \left(\frac{(0.001)^2 * 60}{0.4 * 1.143 * 1.2}\right)^{-1} = 0.009 MPa$$

$$\frac{\rho_f H^2 g_z}{\mu_0 V_c} = \frac{2700 * (0.001)^2 * 9.8 * 60}{0.4 * 1.143} = 3.472$$

Looking at the values of these constants, the entire left-hand side of the momentum equation (accounting for the transient and advection terms) can be neglected since their corresponding constants are much less than one. The body force term (last term on the right-hand side) is not negligible, and must be left in the equation. It is not clear what the importance of the characteristic pressure is in evaluating this process. Based on these findings, the momentum equation can be simplified into the following form:

$$-\frac{dP}{dz} + \mu\left(\frac{\partial V_z}{\partial x}\right) = 0 \qquad (2.38)$$

$$\text{where } \frac{dP}{dz} = \left(\rho_S - \rho_f\right) g \qquad (2.39)$$

2.2.3.1.3 Scaling of the Energy Conservation Equation

The generic form of the energy balance equation, in terms of latent heat, is:

$$\rho C_p \left(\frac{\partial H}{\partial t} + \bar{v} \bullet \nabla H\right) = \nabla(k \bullet \nabla T) + \rho r + \frac{1}{2} S : \dot{\gamma} \qquad (2.40)$$

$$H = C_p\left(T - T_o\right) + H_f * f_l * T(t) \qquad (2.41)$$

To reduce this equation into a suitable 2-D form, it is assumed that properties are constant, no internal heat generation, and negligible viscous dissipation. The equation now becomes:

$$\rho_f C_p\left(\frac{\partial T}{\partial t}+V_x\frac{\partial T}{\partial x}+V_z\frac{\partial T}{\partial z}\right)+\rho_f H_f\frac{df_l}{dT}\frac{\partial T}{\partial t}=k\left(\frac{\partial^2 T}{\partial x^2}+\frac{\partial^2 T}{\partial z^2}\right) \qquad (2.42)$$

Using the previously defined non-dimensional parameters, as well as the following parameter scaling the temperature, the equation becomes:

$$\theta=\frac{T-T_{sol}}{T_{liq}-T_{sol}} \qquad (2.43)$$

$$\frac{\rho_f C_p H^2 V_c}{kL}\left(\frac{\partial\theta}{\partial t^*}+V_x^*\frac{\partial\theta}{\partial x^*}+V_z^*\frac{\partial\theta}{\partial z^*}\right)+\frac{\rho_f H_f H^2 V_c}{k\Delta TL}\frac{df_l}{d\theta}\frac{\partial\theta}{\partial t^*}=\frac{\partial^2\theta}{\partial x^{*2}}+\frac{H^2}{L^2}\frac{\partial^2\theta}{\partial z^{*2}} \qquad (2.44)$$

Evaluating the non-dimensional parameters:

$$\frac{\rho_f C_p H^2 V_c}{kL}=\frac{2700*0.001*(0.001)^2*1.143}{60*2*1.2}=2.1*10^{-8}$$

$$\frac{\rho_f H_f H^2 V_c}{k\Delta TL}=\frac{2700*3E5*1.143*(0.001)^2}{60*2*20*1.2}=0.3215$$

$$\frac{H^2}{L^2}=\frac{(0.001)^2}{(1.2)^2}=6.94*10^{-7}$$

From these values, it can be seen that the transient and advection terms can be considered negligible. Also, the term multiplying the latent heat component is not small enough (with respect to conduction in the x-direction) to be neglected. Therefore, the evolution of the powder s latent heat must be accounted for in any complete interface/gap model. Finally, the term multiplying the z-direction conduction component is very small, so this component can be neglected in this analysis.

2.2.3.1.4 Summary of Scaling Analysis

Several important conclusions can be made based on the scaling analysis of the governing equations. The relationship between x- and z- velocity was found from the continuity equation. This relationship contained an H/L term, which is usually much less than one (H ~ 1 mm, L ~ 1 m). Thus, components of the momentum and energy balance equations containing an x-component of velocity were found to be negligible. From scaling of the momentum equation, the transient and advection terms were determined to be negligible, as well as viscous dissipation in the axial (z-z) direction. From the energy balance equation, only the x-direction conduction and latent heat terms were found to be important. These conclusions greatly simplify the mathematical aspects of an interfacial model, in that it can be treated as a steady-state problem without introducing substantial error. Also, conduction and viscous terms need to be considered only in one direction (x and z, respectively). The following equations represent the estimated conservation equations for the mold/shell interface region:

Mass: $$\frac{\partial V_x^*}{\partial x^*} = 0 \qquad (2.30)$$

Momentum: $$-\frac{dP}{dz} + \mu\left(\frac{\partial V_z}{\partial x}\right) = 0 \qquad (2.38)$$

where $$\frac{dP}{dz} = \left(\rho_s - \rho_f\right)g \qquad (2.39)$$

Energy: $$\frac{\rho_f H_f H^2 V_c}{k \Delta T L} \frac{df_l}{d\theta} \frac{\partial \theta}{\partial t^*} = \frac{\partial^2 \theta}{\partial x^{*2}} \qquad (2.45)$$

The mass conservation equation can also be written in terms of mold powder consumption through the following relationship:

$$\frac{Q_f}{\rho \cdot 2(W+N)} = V_s d_s + \int_0^{d_l} V_l(x)dx \qquad (2.46)$$

In order to evaluate this relationship, equations for flux layer thickness and velocity must be derived.

2.2.3.1.5 Derivation of Flux Layer Thickness and Velocity Relationships

In order to obtain quick results for flux layer thickness and velocities, the latent heat term in equation 2.45 will be ignored. The energy conservation equation, in dimensional form, now becomes:

$$\frac{d^2T}{dx^2} = 0 \qquad (2.47)$$

Integrating this equation with the following boundary conditions gives:

$$T(x) = c_1 x + c_2$$

$$T(x = 0) = T_{mold}$$

$$T(x = H(z)) = T_{shell}$$

$$T(x) = \frac{T_{shell} - T_{mold}}{H(z)} x + T_{mold} \qquad (2.48)$$

Analytical relationships for liquid and solid flux layer thickness can be calculated from equation 2.48 by observing that:

$$T(x = d_s) = T_{fsol} \qquad (2.49)$$

$$d_l = H(z) - d_s \qquad (2.50)$$

$$d_s = \frac{T_{fsol} - T_{mold}}{T_{shell} - T_{mold}} H(z) \qquad (2.51)$$

$$d_l = \frac{T_{shell} - T_{fsol}}{T_{shell} - T_{mold}} H(z) \qquad (2.52)$$

The analytical solution for the flux layer velocity is obtained through integrating the estimated momentum conservation equation. To help in the solution, the viscosity power-law relationship (Equation 2.36) will use a modified characteristic viscosity μ_s, which is defined at the shell surface at temperature T_{shell}:

$$\mu = \mu_s \left(\frac{T_{shell} - T_{fsol}}{T - T_{fsol}} \right)^m \qquad (2.53)$$

Incorporating equations 2.51 and 2.52 gives:

$$\frac{\mu}{\mu_s} = \left(\frac{T_{shell} - T_{fsol}}{T - T_{fsol}} \right)^m = \frac{\left(\dfrac{T_{shell} - T_{fsol}}{T_{shell} - T_{mold}} \right)^m}{\left(\dfrac{T - T_{fsol}}{T_{shell} - T_{mold}} \right)^m}$$

$$= \left(\frac{\dfrac{d_l}{H(z)}}{\dfrac{x - d_s}{H(z)}} \right)^m = \left(\frac{d_l}{x - d_s} \right)^m \qquad (2.54)$$

Integrating the reduced momentum conservation equation with the following boundary conditions gives:

$$\begin{aligned} V_z(x = 0) &= V_s \\ V_z(x = H(z)) &= V_c \end{aligned} \qquad (2.55a,b)$$

$$V_z(x') = V_s + (V_c - V_s)\left[\left(\frac{x'}{d_l} \right)^{m+1} - \frac{\tilde{\rho} g d_l^{\,2}}{(m+2)\mu_s (V_c - V_s)} \left[\left(\frac{x'}{d_l} \right)^{m+1} - \left(\frac{x'}{d_l} \right)^{m+2} \right] \right] \qquad (2.56)$$

where

$$\begin{aligned} x' &= x - d_s \\ \tilde{\rho} &= \left(\rho_s - \rho_f \right) \end{aligned} \qquad (2.57a,b)$$

2.2.3.1.5.1 Derivation of Stokes-based Flux Layer Thickness and Velocities

In reviewing equation 2.56, a non-dimensional Stokes-type group can be identified. This modified Stokes number, which represents the ratio of viscous forces to forces from gravity and pressure gradients, is defined as:

$$St = \frac{\mu_s (V_c - V_s)}{\tilde{\rho} g d_l{}^2} \qquad (2.58)$$

In analyzing the numerator of equation 2.58, the range of values for this non-dimensional group can vary largely as the liquid layer solidifies further down the mold. For large Stokes values, viscous forces dominate the system behavior and the velocity equation 2.56 can be rewritten as:

$$V_z(x') = V_s + (V_c - V_s)\left[\left(\frac{x'}{d_l}\right)^{m+1}\right] \qquad (2.59)$$

Substituting equation 2.59 as the liquid layer velocity in equation 2.46 gives the following relationships for flux layer thicknesses:

$$d_l = \frac{Q_f}{2\rho(W+N)} \frac{1}{\left[V_s + \left(\frac{V_c + V_s}{m+2}\right) + V_s\left(\frac{T_{fsol} - T_{mold}}{T_{shell} - T_{fsol}}\right)\right]} \qquad (2.60)$$

$$d_s = \frac{Q_f}{2\rho(W+N)} \frac{\left(\frac{T_{fsol} - T_{mold}}{T_{shell} - T_{fsol}}\right)}{\left[V_s + \left(\frac{V_c + V_s}{m+2}\right) + V_s\left(\frac{T_{fsol} - T_{mold}}{T_{shell} - T_{fsol}}\right)\right]} \qquad (2.61)$$

$$H(z) = d_s + d_l \qquad (2.62)$$

For Stokes values of order one, and following the same method of solution as above, the flux thickness relationships become

$$d_l{}^3 + a d_l + b = 0$$
$$a = -\frac{\mu_s (m+2)^2 (m+3)}{\tilde{\rho} g}\left[V_s\left(\frac{T_{shell} - T_{mold}}{T_{shell} - T_{fsol}}\right) + \frac{(V_c - V_s)}{(m+2)}\right] \text{(2.63a-c)}$$
$$b = \frac{\mu_s Q_f (m+2)^2 (m+3)}{2\rho\tilde{\rho} g (W+N)}$$

$$d_s = \frac{T_{fsol} - T_{mold}}{T_{shell} - T_{fsol}} d_l \qquad (2.64)$$

2.2.3.1.6 Characterization of Oscillation Mark Geometry

Oscillation marks, which are surface depressions in the steel slab, are formed by the oscillation of the copper mold [2]. These depressions affect the heat removal from the steel by increasing thermal resistance between the shell and the mold. Depending on the slab s surface temperature and position within the mold, these oscillation marks may be filled with either mold flux (in liquid or solid form) or air. Oscillation marks that are filled with air present irregularities in interfacial heat transfer, and results in the marks being hotter than the slab surface between them. Temperature differences such as these can result in diminished surface quality if not properly accounted for in mold powder development.

In CON1D, oscillation marks are treated as an additional thickness that defines the gap between the steel and the mold. Figure 2.8 [12] shows a schematic of the domain used to analyze these marks. In an earlier analysis by Ho [15], the following relation is used to characterize the oscillation marks in the interface model:

$$d_{eff} = \frac{L_{mark} d_{mark}}{L_{pitch}\left(1 + \frac{d_{mark}}{d_{gap}}\right) + L_{mark}} \qquad (2.65)$$

As shown in Figure 2.8, these variables are easily measured with a representative section of a steel slab that has a section of repeating oscillation marks.

2.2.3.1.7 Calculation of Interfacial Heat Transfer Coefficients

Heat transfer across the mold/shell interface is characterized by:

$$q_{gap} = h_{gap}\left(T_{shell} - T_{mold}\right) \qquad (2.66)$$

The method for calculating the gap heat transfer coefficient, h_{gap} , is dependent on whether a liquid flux layer is present at the time and mold position of interest. A schematic representation of the heat transfer network analogy is shown in Figure 2.9. Conduction and radiation are the dominant mechanisms of heat transfer within this region, and are assumed to act parallel with one another such that:

$$q_{gap} = q_{cond} + q_{rad} \quad (2.67)$$

Conduction heat transfer occurs across solid flux layers (both glassy and crystalline), as well as any contact resistances between the flux layer and its interface with the shell and mold. It is assumed that the solid flux layers, with their many cracks and voids, will diffuse any radiation that they encounter. Thus, radiation heat transfer occurs exclusively across any liquid flux layer that exists. The following equations are used to characterize conductive and radiative heat transfer across the mold/shell gap:

Only liquid layer present:

$$h_{gap} = \frac{1}{\left(\frac{d_l}{k_l} + \frac{d_{eff}}{k_{eff}}\right)} + \frac{n^2\sigma\left(T_{Fe}^2 + T_{hot}^2\right)\left(T_{Fe} + T_{hot}\right)}{.75a\left(d_l + d_{eff}\right) + \frac{1}{\varepsilon_{mold}} + \frac{1}{\varepsilon_{steel}} - 1} \quad (2.68)$$

Liquid and solid layers present:

$$h_{gap} = \frac{1}{\left(\frac{d_{air}}{k_{air}} + \frac{d_{sol}}{k_{sol}} + \frac{d_l}{k_l} + \frac{d_{eff}}{k_{eff}}\right)} + \frac{n^2\sigma\left(T_{Fe}^2 + T_{hot}^2\right)\left(T_{Fe} + T_{hot}\right)}{.75a\left(d_l + d_{sol}\right) + \frac{1}{\varepsilon_{slag}} + \frac{1}{\varepsilon_{steel}} - 1} \quad (2.69)$$

Only solid layer present:

$$h_{gap} = \frac{1}{\left(\frac{d_{air}}{k_{air}} + \frac{d_{sol}}{k_{sol}} + \frac{d_{eff}}{k_{eff}}\right)} \quad (2.70)$$

Values for mold, slag, and steel emissivities are input by the user, while the flux index of refraction, n, is a weighted average of the powder s components [16].

2.2.4 Heat Transfer within Secondary Cooling Zones

Figure 2.10 [12] shows a schematic of the secondary cooling zone, which is located underneath the continuous casting mold. This cooling system further solidifies the steel slab to its final metallurgical thickness. This system also straightens the slab, and prepares it to be cut into lengths that are easy to roll and process.

Heat transfer within this system is governed primarily through forced convection, as water is sprayed on the slab s surface by strategically placed nozzles. This convective heat transfer coefficient is calculated through use of the following correlation:

$$h_{spray} = \frac{1570}{4} Q_w^{0.55} (1 - 0.0075 T_o) \qquad (2.71)$$

Heat transfer within this region is also enhanced by conduction through the support rolls and possible nucleate boiling if the slab surface is below 550 °C.

2.3 Model Validation against Analytical Solution

To evaluate the accuracy of the CON1D mathematical model, its results were compared to those of an analytical model, derived by Hills [17], which calculates steady-state two-dimensional shell growth based on the values of a few non-dimensional parameters.

2.3.1 Derivation of Hills Analytical Model

Hills analytical solution can be more easily understood by looking at a one dimensional, transient model of solidification. Figure 2.11 shows the problem and model domain. Assuming the temperature distribution within the solid shell is linear, The heat flux in the solid shell at the mold interface is:

$$q\big|_{x=0} = k_{steel} \frac{T_\infty - T_{steel}}{\delta} \qquad (2.72)$$

The heat flux across the interface between shell and mold is:

$$q\big|_{x=0} = h_{gap}\left(T_{steel} - T_{mold}\right) \quad (2.73)$$

Substituting equation 2.65 into 2.66 and eliminating the surface temperature leaves:

$$q\big|_{x=0} = q\big|_{x=\delta} = \frac{T_\delta - T_{mold}}{1/h_{gap} + \delta/k_{steel}} \qquad (2.74)$$

At the interface between the liquid and solid steel, latent heat is evolved and the heat flux can also be defined as:

$$q\big|_{x=\delta} = \rho_{steel} H_f \frac{d\delta}{dt} \quad (2.75)$$

From equations 2.67 and 2.68, the transient position of the liquid-solid interface can be derived by integrating across the thickness of the solid shell:

$$\delta = \frac{h_{gap}\left(T_\delta - T_{mold}\right)}{\rho_{steel} H_f} t - \frac{h_{gap}}{2k_{steel}} \delta^2 \quad (2.76)$$

C.M. Adams derived the solution to this problem without making the assumption of linear temperature behavior within the shell. Adams solution is similar to equation 2.69, with an additional variable:

$$\begin{aligned} \delta &= \frac{h_{gap}\left(T_\delta - T_{mold}\right)}{\rho_{steel} H_f a} t - \frac{h_{gap}}{2k_{steel}} \delta^2 \\ a &\equiv \frac{1}{2} + \sqrt{\frac{1}{4} + \frac{C_p^{steel}\left(T_\delta - T_{mold}\right)}{3H_f}} \end{aligned} \qquad (2.77a,b)$$

Hills solution applies two modifications to these results. First, the one-dimensional transient analysis is converted to a steady state, two-dimensional analysis by transforming time into distance down the mold, y, divided by the casting speed S:

$$t = \frac{y}{S} \quad (2.78)$$

Also, the steel s latent superheat is accounted for by defining an effective latent heat of fusion:

$$H_f' = H_f + C_p^{steel}\left(T_p - T_\delta\right) \quad (2.79)$$

Incorporating Equations 2.78 and 2.79 into Adams solution gives the following equation for shell growth:

$$\delta = \frac{h_{gap}\left(T_\delta - T_{mold}\right)}{\rho_{steel} H_f' a}\frac{y}{S} - \frac{h_{gap}}{2k_{steel}}\delta^2$$
$$a \equiv \frac{1}{2} + \sqrt{\frac{1}{4} + \frac{C_p^{steel}\left(T_\delta - T_{mold}\right)}{3H'_f}} \quad (2.80a,b)$$

The key parameters of this equation can be represented in terms of the Biot and Stefan Numbers, and Y^*, which is a nondimensional distance down the mold:

$$Bi \equiv \frac{h_{gap}\delta}{k_{steel}} \quad (2.81)$$

$$Ste \equiv \frac{C_p^{steel}\left(T_{steel} - T_{mold}\right)}{H'_f} \quad (2.82)$$

$$Y^* \equiv \frac{h_{gap}^2 y}{S \cdot k_{steel}\rho_{steel}C_p^{steel}} \quad (2.83)$$

Figure 2.12 shows the thickness of the solidifying shell as a function of distance down the mold. Notice that for increasing Stefan Number the thickness of the shell increases.

2.3.2 Comparison of Numerical and Analytical Models

In order to validate CON1D against Hills analytical solution, the model is modified to provide a constant heat transfer coefficient between the shell and mold. This modification disables the interfacial model, which Hills analysis does not take into consideration. Mold water and material properties are kept constant, and air gaps are not allowed to form. The constants used for this comparison are shown in Table 2.2.

Figure 2.13 shows a plot of both models predictions. The value for the inverse Stefan number used to derive Hills analytical results is 0.366. Predictions from the numerical model are bounded by the analytical model s values for (Ste^{-1}) of 0.3 and 0.4. This shows that the numerical model is predicting reasonable values for the shell growth with respect to the analytical solution.

An enlarged view of the area in interest, as well as Hills model prediction for the same inverse Stefan number, is shown in Figure 2.14. These results show that the numerical model is reasonably predicting shell growth behavior, although values are slightly less that of the analytical model.

Next, both the numerical and analytical models were used to predict shell growth, based on data obtained from an instrumented mold of a thin slab caster. Three cases were investigated. In Case 1, the numerical model was calibrated with the industrial data. This case incorporated all of the models complex functions, including superheat and interfacial behavior. Varying heat transfer coefficients for the gap were obtained by exercising the full functionality of the numerical model. In Case 2, the numerical model was modified the same way as it was in the model validation section. The value of the constant heat transfer coefficient was obtained by matching the values of average mold heat removal, between original and modified model, to within 1%. Case 3 applied Hills analytical model to the casting conditions, using the same heat transfer coefficient as in case 2. The constants used for this comparison are shown in Table 2.3.

Figure 2.15 shows the shell growth profile for each of the three cases, plotted in terms of the non-dimensional parameters. By viewing the results, it is clear that all three cases produces results that are within +/- 5% of each other. This shows that, for simple models of continuous casting, the assumption of a constant heat transfer coefficient in the mold is not a bad first guess. This exercise shows that the numerical model produces values that closely match those of Hills analytical solution.

2.4 Summary

This chapter has described the numerous aspects of the CON1D numerical model for simulating the continuous casting process. The individual aspects of heat transfer within the process have been described, with the interfacial heat transfer model being described in depth. After describing the model, CON1D was validated against Hills analytical solution for shell growth. The validation effort showed the numerical predictions to be within 5% of analytical results.

In the next chapter, experiments will be run to characterize the thermal behavior of the mold flux layer as it cools from a liquid to a solid state. Liquid and solid flux conductivity as a function of temperature is difficult to obtain for casting fluxes, as these parameters are greatly dependent on powder composition. A simple apparatus has been developed to measure flux conductivity with varying temperatures. This data will be used to predict shell thickness profiles from a breakout shell.

Table 2.1: Process Parameters used to evaluate estimation equations

Parameter	Value
Mold Length, L	1.2 m
Casting Speed, V_c	1.143 m/min
Flux Film Thickness, H	0.001 m
Flux Conductivity, k	2.0 W/m*K
Flux Density, ρ_f	2700 kg/m^3
Flux Specific Heat, C_p	0.001 J/kg*K
Flux Viscosity at 1300 C, μ_o	0.4 kg/m*s
Flux Latent Heat of Fusion, H_f	3.0E5 J/kg

Table 2.2: Process Parameters used in CON1D Validation against Hills Analytical Solution

Parameter	Value
Distance from meniscus to end of mold, X	1.096 m
Casting Speed, u	0.589 m/min
Mold heat transfer coefficient, h	1000 W/m^{2}K
Steel Conductivity, k	27 W/mK
Steel Density, ρ	7270 kg/m^3
Steel Specific Heat, C_p	0.569 kJ/kgK
Steel Latent Heat of Fusion, H_f	304 kJ/kg
Pour Temperature	1560 C
Solidus Temperature	1460 C

Table 2.3: Process Parameters used in Comparing CON1D Results against Hills Analytical Solution for Thin Slab Caster

Parameter	Value
Distance from meniscus to end of mold, X	1.096 m
Casting Speed, u	1.143 m/min
Mold heat transfer coefficient, h	1405 W/m^2*K
Steel Conductivity, k	27 W/m*K
Steel Density, ρ	7270 kg/m^3
Steel Specific Heat, C_p	0.569 kJ/kg*K
Steel Latent Heat of Fusion, H_f	304 kJ/kg
Pour Temperature	1560 C
Solidus Temperature	1460 C

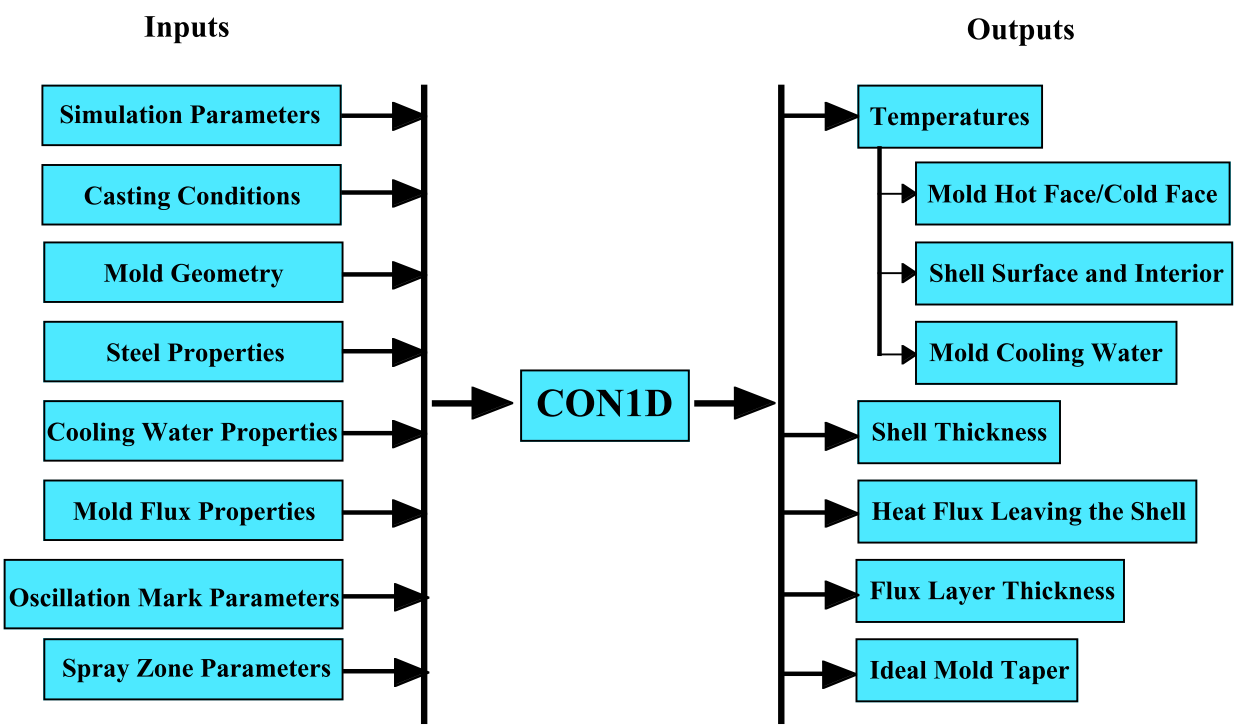

Figure 2.1: Flowchart for CON1D numerical model parameters

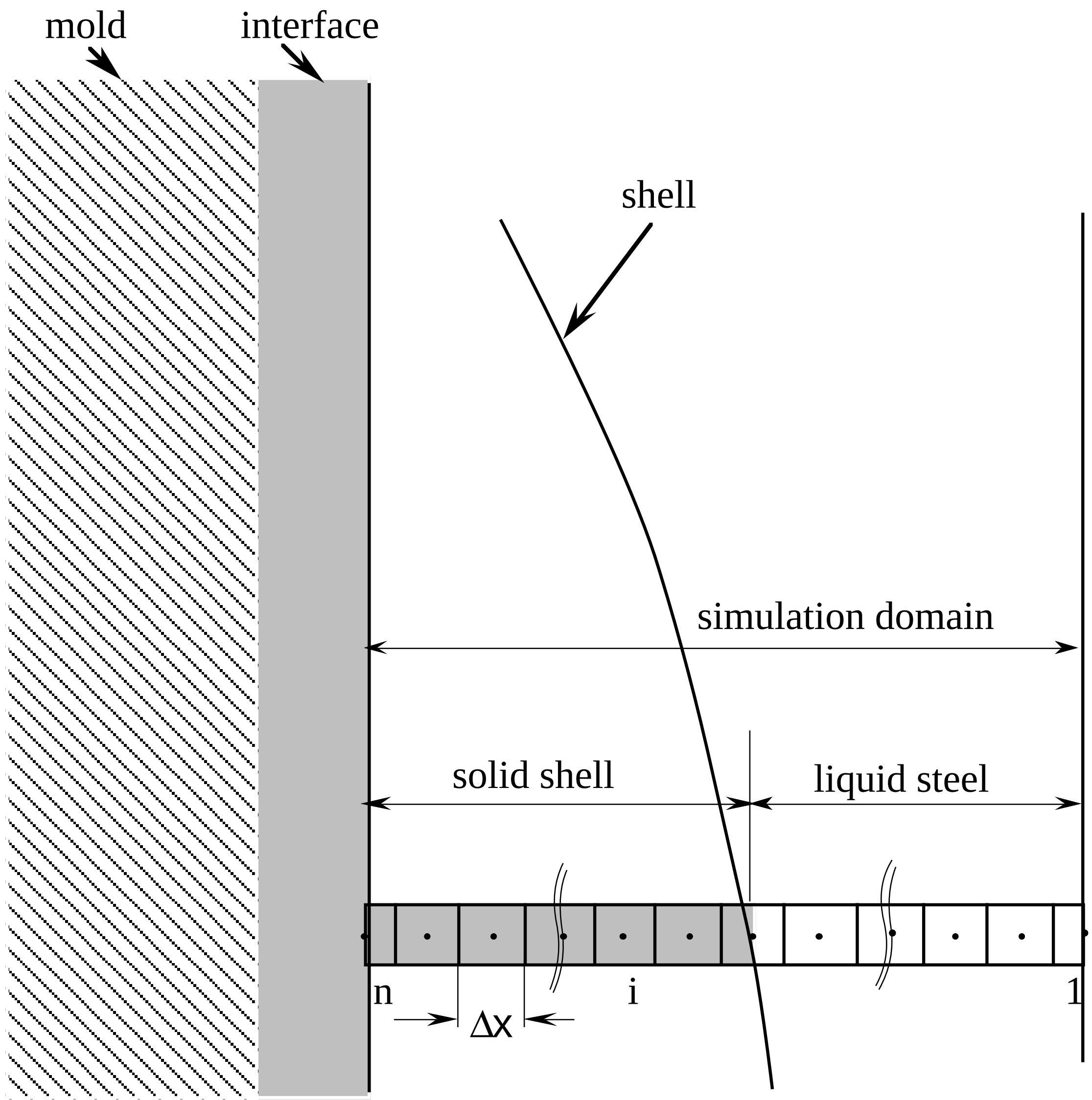

Figure 2.2: CON1D numerical model domain [12]

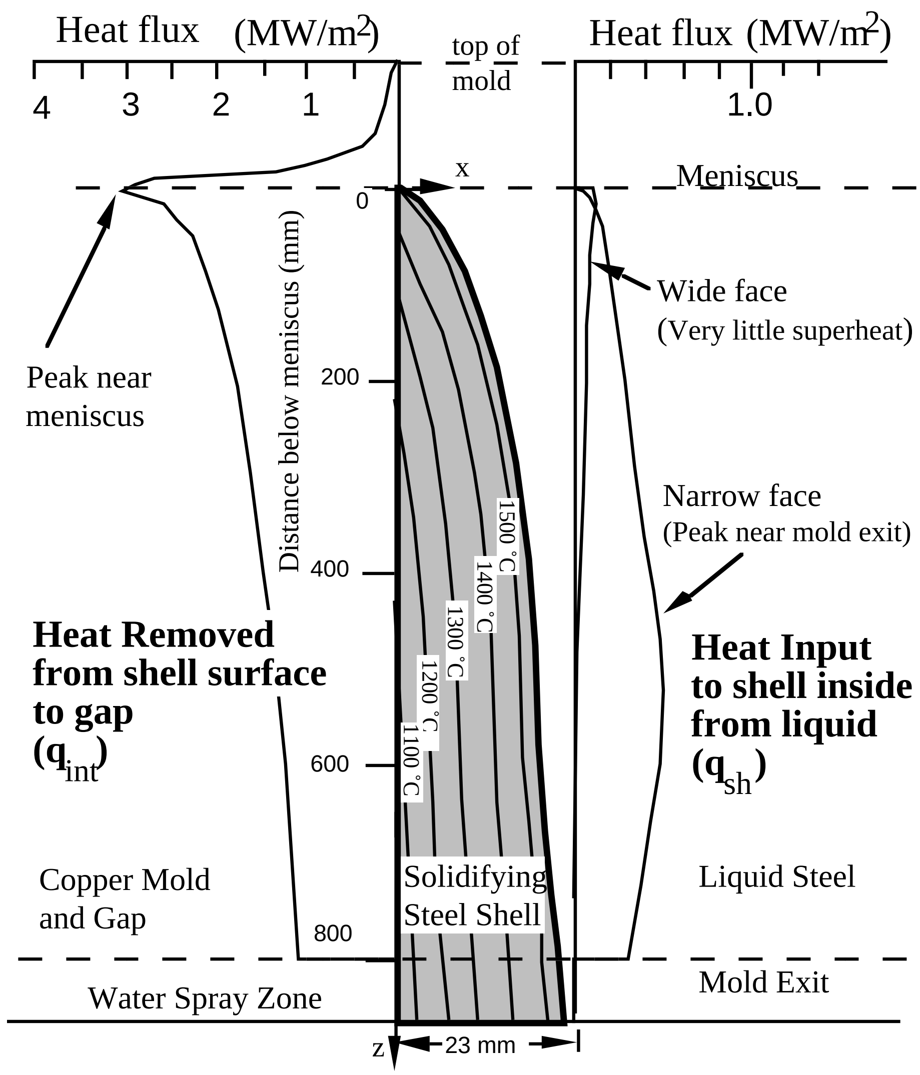

Figure 2.3: Superheat Dissipation as a function of Distance below the meniscus [12]

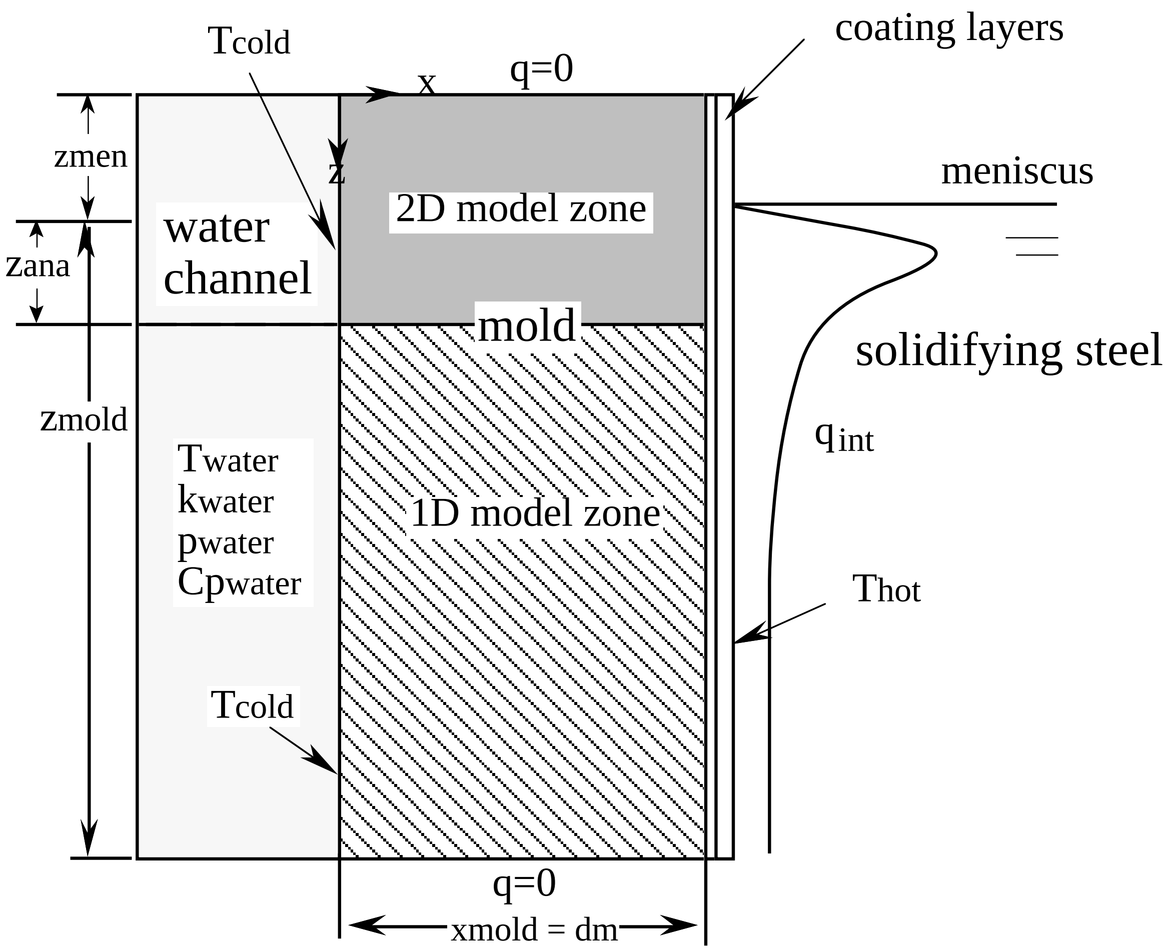

Figure 2.4: Description of mathematical models used to calculate heat transfer within the mold region [12]

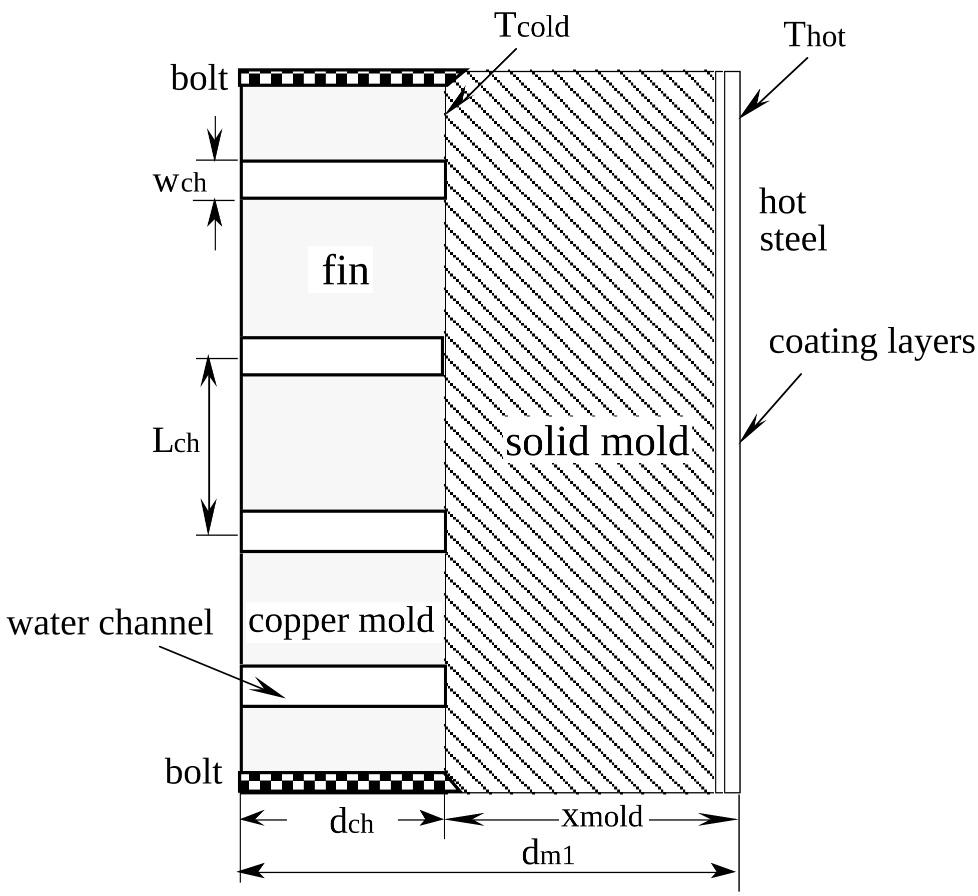

Figure 2.5: Schematic of Water Channel Model Domain [12]

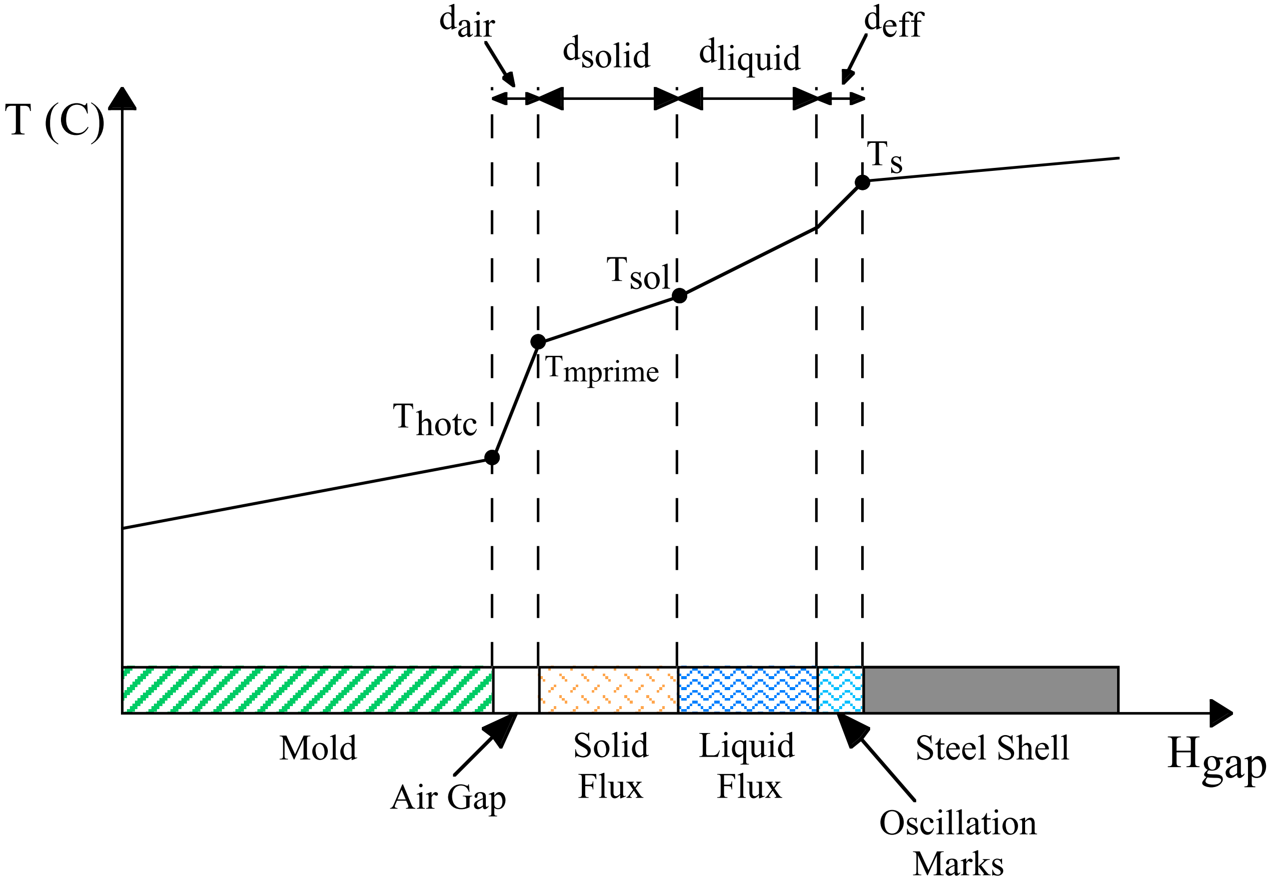

Figure 2.6: Schematic of Temperature Distribution through CON1D model domain

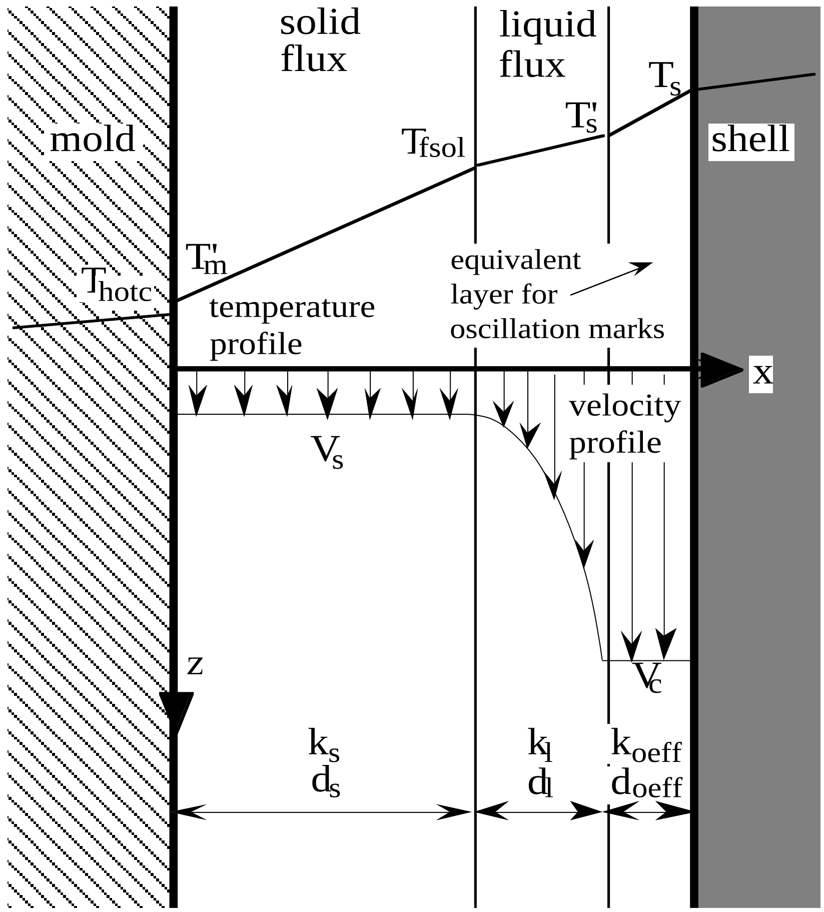

Figure 2.7: Schematic of Velocity and Temperature Distribution through Mold Flux Film [12]

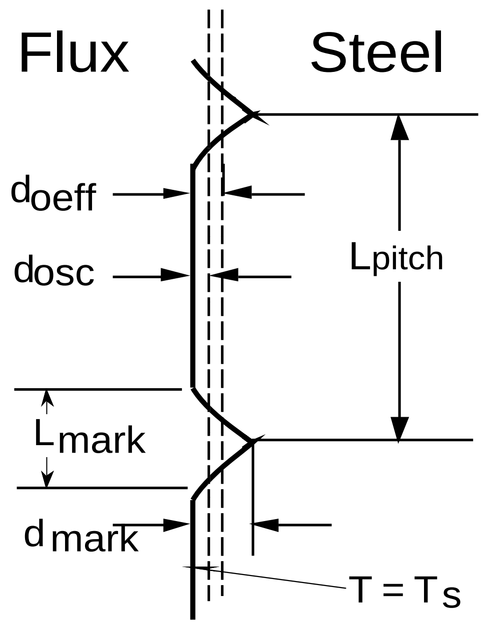

Figure 2.8: Schematic of oscillation marks in steel slab, with variables used in CON1D [12]

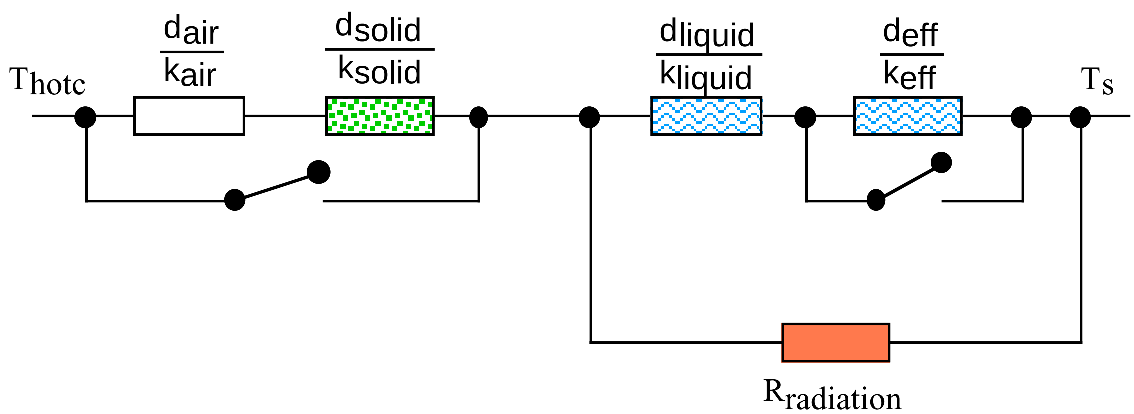

Figure 2.9: Electrical Resistance Description of CON1D Interfacial Heat Transfer Model

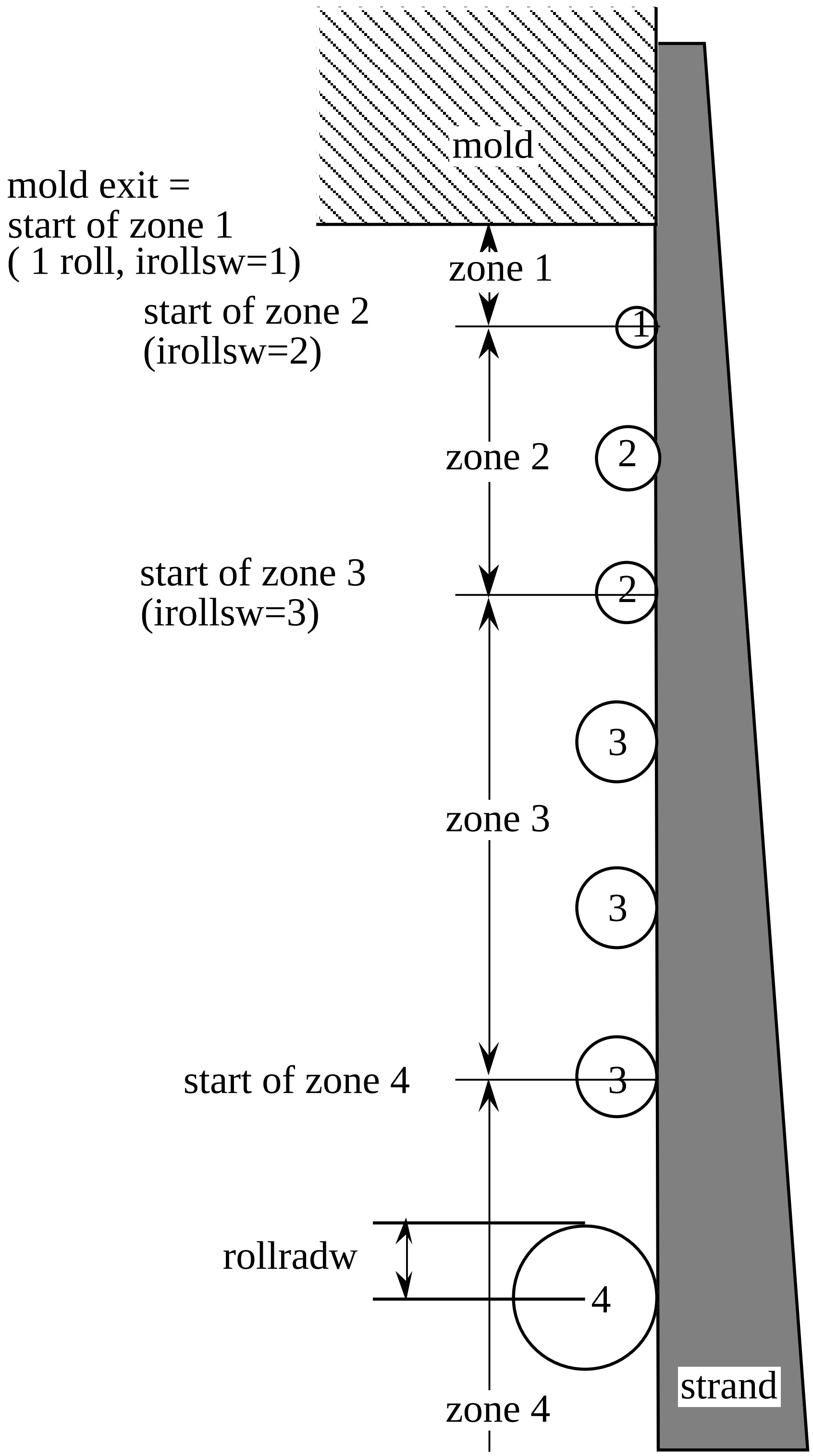

Figure 2.10: Schematic of Secondary Cooling Zone Modeled in CON1D [12]

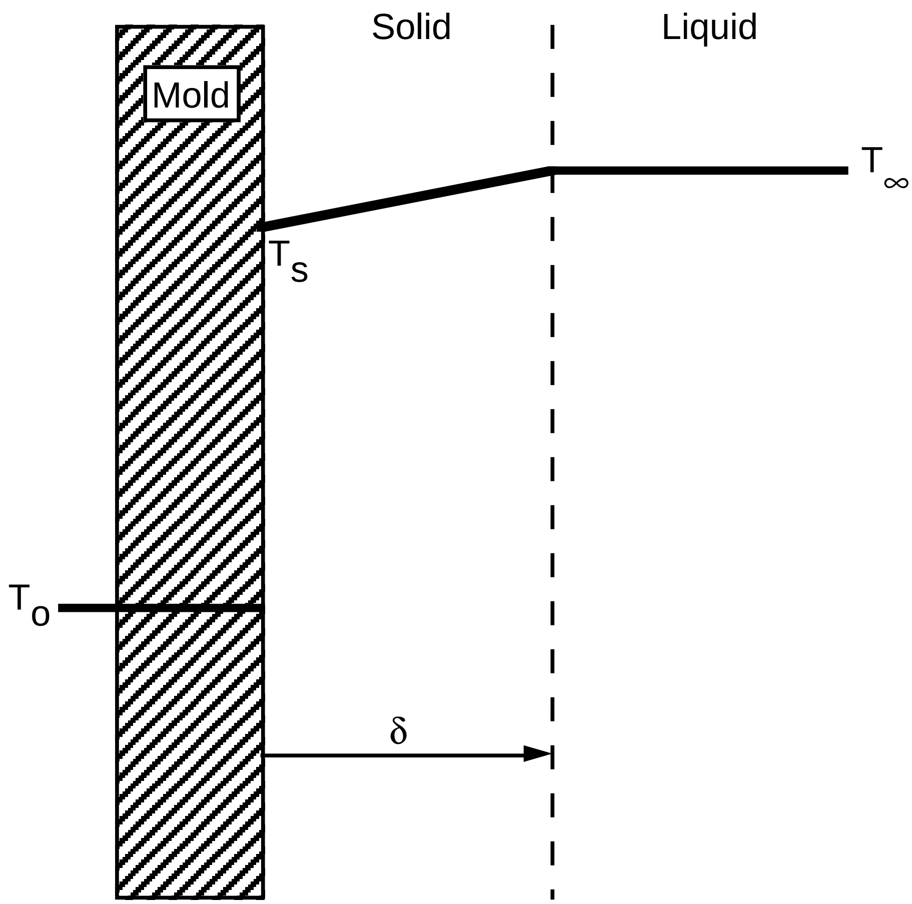

Figure 2.11: Model Domain for Hills analytical Solution

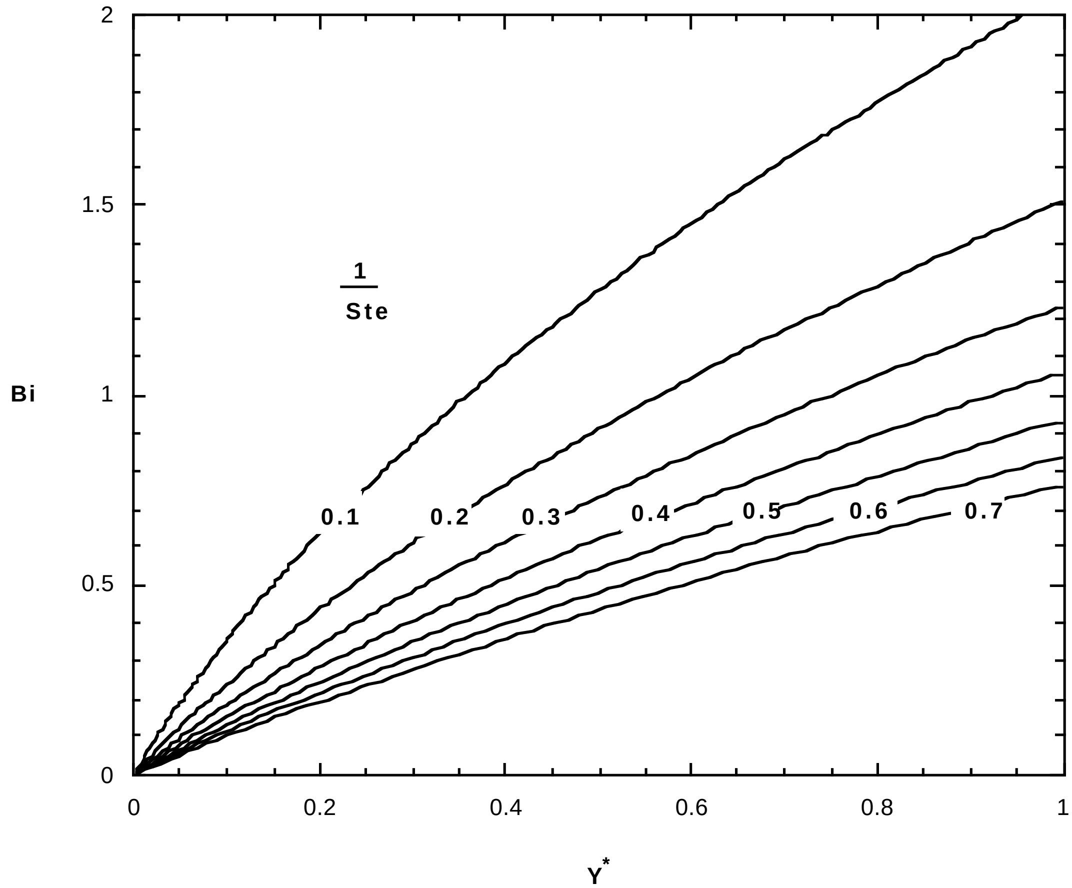

Figure 2.12: Hills analytical solution for steel thickness as a function of distance down the mold

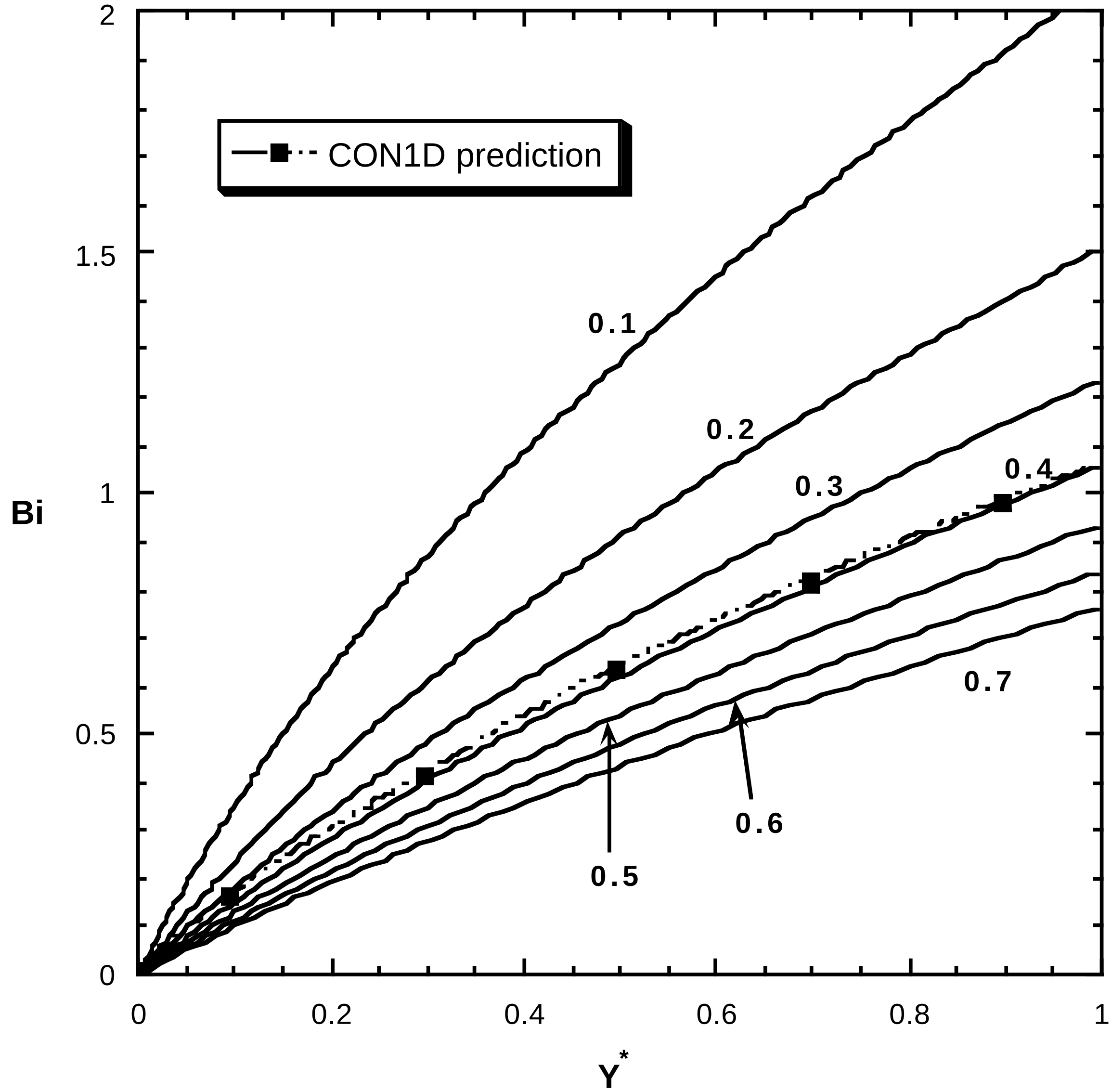

Figure 2.13: Comparison of Hills Analytical Solution to CON1D Numerical Predictions

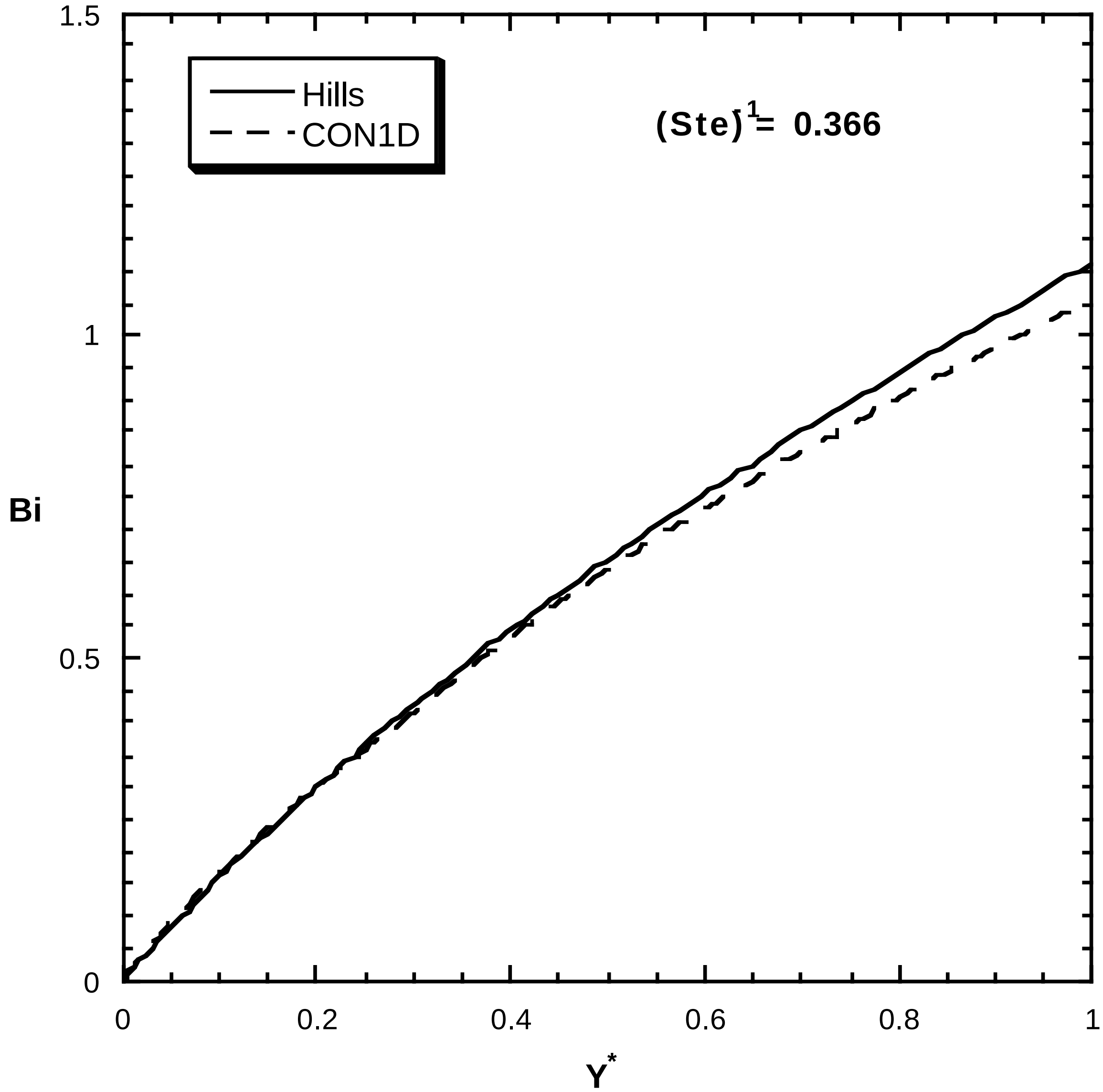

Figure 2.14: Closeup, Comparison of Hills Analytical Solution to CON1D Numerical Predictions

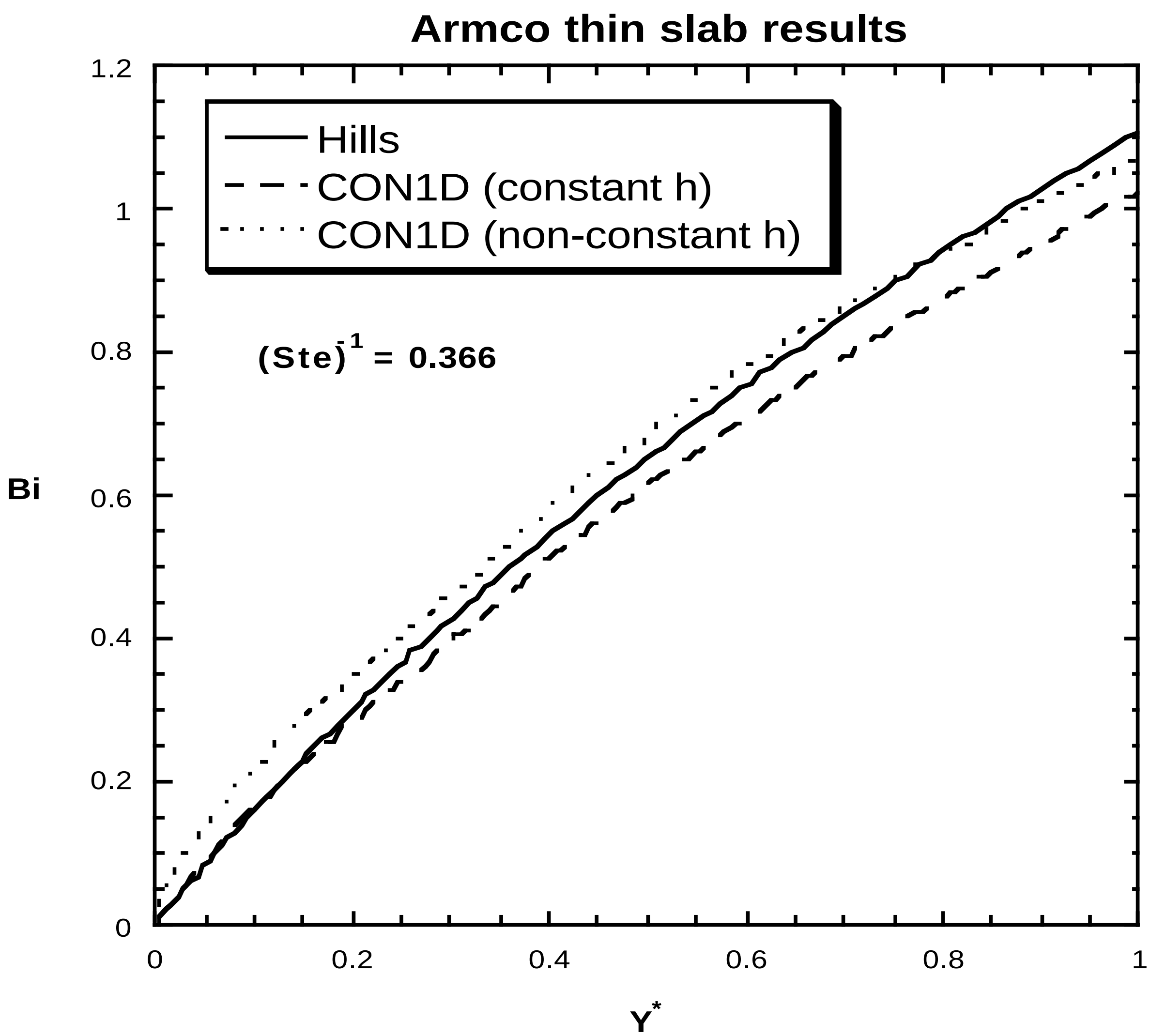

Figure 2.15: Effect of constant mold heat transfer coefficient on predictions; last case based on Industrial Data

3 MOLD FLUX EXPERIMENTS

In the previous chapter that described the mathematical model CON1D it was shown that by supplying the model with process parameters, the user gains extensive insight into product behavior and potential quality concerns. Most of the process parameters needed by the model are quantifiable through measurements, such as mold geometry, steel temperature and chemistry. The rate of heat transfer across the interfacial gap depends mainly on the properties of the mold flux filling the gap. These properties include phonon and photon conductivity [18], radiative properties such as emissivity and absorption coefficient [19], and contact resistances, especially where the flux is solid. The extremely small scale of the interfacial heat transfer region, which is on the order of one millimeter, prohibits real-time measurement of these properties. Thus, laboratory experiments are often used to quantify the thermal characteristics of mold powder materials.

This chapter documents a set of experiments, conducted at the Armco Research Center, that attempt to simulate the gap between the continuous casting mold and solidifying steel shell. An ocy-acetylene torch is used to input heat to the experimental apparatus, while thermocouples measure the system's transient temperature response. These temperatures are then used to model the radiative and conductive resistances of the mold flux. Initial findings of these experiments have been reported elsewhere [20], and further analysis of the test data are shown here.

3.1 Literature Review

Several researchers have performed experiments to measure the thermal properties of mold fluxes under thermal conditions designed to simulate those in the gap during continuous casting of steel. The measured properties depend greatly on the model used to derive those properties, so experiments and models must be discussed together.

Ohmiya [21] simulated the mold/strand gap by lowering a cooled copper block into a layer of molten mold flux that was resting on a steel plate heated by an electric current. Heat transfer through the powder was measured by three thermocouples (two in the copper mold and one on the steel). Data was obtained for several test materials (with known conductivities) and three commercial mold powders. Effective thermal conductivity, k_{gap}, quantifies heat transfer across the entire gap width, d_{gap}, from all mechanisms combined together, including standard (phonon) conduction, radiation (photon) conduction, and the effect of contact resistances:

$$\dot{q} = k_{gap} \frac{T_{Fe} - T_{Cu}}{d_{gap}} \quad (3.1)$$

where T_{Fe} and T_{Cu} are the surface temperatures of the hot steel and cold copper that face the gap. In addition to reporting the raw data and gap conductivities, thermal properties can be obtained by fitting the data to an equation that includes both conduction and radiation terms (acting independently).

$$\dot{q} = \gamma_1 (T_{Fe} - T_{Cu}) + \gamma_2 (T_{Fe}^4 - T_{Cu}^4)$$
$$where \;\; \gamma_1 = \frac{k_{flux}}{d_{gap}} \;\; and \;\; \gamma_2 = \frac{m^2 \sigma}{0.75 a d_{gap} + 1/\varepsilon_{Fe} + 1/\varepsilon_{Cu} - 1} \quad (3.2)$$

Values of mold flux thermal conductivity, k_{flux}, calculated in this way ranged between 0.22 and 0.43 W/mK. The radiation component was significant. Furthermore, the fitted parameters were still strong functions of the thickness of the flux layer, indicating that these thermal properties are not fundamental. This is likely due to the temperature dependence of the properties, especially the absorption coefficient, a, which is reported to be a strong function of wavelength and increases if crystallization occurs [6, 19]. The error (underprediction of heat flux) due to ignoring the interaction between the conduction and radiation terms is predicted to be less than 6% [3].

Mills and coworkers have conducted many experimental measurements of mold flux properties [6, 19, 22]. The thermal conductivity of mold powders and solidified mold flux films were extracted using the laser pulse method. In this method, a laser pulse is directed onto the front face of the specimen and the temperature transient of the rear face is recorded continuously. Thermal conductivity is derived by estimating the thermal diffusivity and taking the density, ρ, and specific heat, C_P, from previous measurements:

$$k_{gap} = \rho C_P \frac{0.1388\, d_{gap}{}^2}{t_{0.5}} \qquad (3.3)$$

Here, $t_{0.5}$ is the time taken to reach half of the maximum temperature rise. Molten flux conductivities of 1.3 to 2.5 W/mK were reported, with values of glassy films being much lower than those of partially crystalline films. This conductivity is an effective value, which includes both conduction and radiation components. After extensive investigation, Mills concluded that variations in heat transfer between different trials were not caused by any composition dependence of the flux conductivity.

The absorption coefficient of glassy films can be predicted the empirical relation [23] $a(m^{-1})$= 910 * (%FeO). For crystalline slags, absorption is much greater, with reported extinction coefficients of 100,000 m^{-1} [19]. Even in predominantly glassy films, where radiation conduction is more important, its contribution to the total heat flux (the second term in Eq. 2) was predicted to be less than 10% under continuous casting conditions [6]. Total normal emissivities of around 0.9 were measured.

Mikrovas [18] utilized the "copper finger" method to measure the thermal properties of thick slag layers. In this method, a chilled copper cylinder is immersed in a bath of molten flux, and temperatures measured within the flux and copper. A transient model was used to extract the effective conductivity (Eq. 3.1). Conductivities of 1.2 to 1.5 W/mK were measured near the melting temperature, while values up to 4.0 W/mK were obtained when the slag was superheated by 400 ˚C. The increase was attributed to the greater importance of radiation at the higher temperatures and in thicker flux layers. Mikrovas also observed a drop in conductivity with increasing TiO_2 content. Finally, additional experiments and calculations estimated the interfacial resistance between the copper cylinder and the mold flux layer to be 8.8 $\times 10^{-4}$ m^2K/W together with an effective conductivity of 3.0 W/mK.

Jenkins [24], using a more sophisticated copper finger apparatus, obtained values of thermal conductivity of around 1.0 W/mK, and absorption coefficients of around 350m^{-1}. Contact resistances of 1 - 3 $\times 10^{-4}$ m^2K/W were measured. Jenkins also investigated the effect that doping mold powders with transition metal oxides had on radiative heat transfer across the mold/strand gap.

Susa [23] utilized the hot strip method to measure thermal conductivity, thermal diffusivity, and specific heat of mold powders containing iron oxides. Many different chemical compositions of mold powders were tested, and values of thermal conductivity were measured to be between 1.5 and 2.2 W/mK at temperatures below 1200 K. Above 1200 K, conductivity values decreased with increasing temperature, which is possibly due to the increased dominance of radiation in total mold heat transfer. Mold flux specific heat increases with increasing temperature, especially above the glass transition temperature.

Yamauchi [25] simulated the mold/strand gap by heating previously solidified mold flux samples between a heated AlN plate and a cooled block of 304 stainless steel. Four different powders were tested, and data was evaluated with a 1-D heat transfer model.

$$\dot{q} = \frac{T_{Fe} - T_{Cu}}{d_{gap} / k_{eff} + R_{int}} \qquad (3.4)$$

Most of the test conditions were well below the flux solidification temperatures, and conductivities of 0.6 to 1.3 W/mK were reported. Further investigation into the radiative component of the heat transfer revealed that the radiation conductivity was approximately 20%

of the total heat transfer. Interfacial air gaps of between 0.004-0.008 m^2K/W were observed for solid fluxes. Negligible resistances were measured above the flux melting temperature. Also, k_{eff} was observed to decrease with increasing mold powder basicity (CaO/SiO_2).

This section has illustrated the variety of previous experiments and models that have been used to quantify the thermal properties of mold fluxes. The present work aims to measure mold flux properties under conditions that match the thermal histories experienced by the liquid flux in the continuous casting process. In addition, extra thermocouples will be used in the interfacial gap, in order to distinguish the contributions of the flux conductivity and interface resistances. Any changes in the properties with time will be observed.

3.2 Description of Experimental Apparatus

An apparatus was constructed to simulate the conditions experienced by the liquid mold flux in the gap near the meniscus in the continuous casting process. Figure 3.1 shows a schematic of the test apparatus, which includes a machined block of 99.9% pure copper to represent the mold, and a 3.17- mm thick plate of 409 stainless-steel hot band to represent the surface of the solidifying steel shell. The thickness of the gap was controlled by inserting stainless steel spacers of known thickness between the steel plate and copper block prior to bolting them together. To minimize contact between the hot steel and cold copper, one of the spacers was a thin (1.0-mm diameter) stainless steel wire.

Heat was provided to the outside of the steel plate by an oxy-acetylene torch. Figure 3.2 shows the test stand setup, along with the torch. The torch position was adjustable in order to control the steel temperature. The copper mold was cooled by flowing 25 ßC water at 0.08-0.11 liter/s through 9.525 mm (3/8) diameter copper tubing, which was formed into a flat coil and squeezed against the back of the copper mold using bolts. This cooling system is shown in Figure 3.3.

The design of the copper mold and thermocouple placement is shown in Figures 3.4 and 3.5. The steel hot band was connected to the copper mold by seven steel bolts. Seven thermocouples are used to measure temperatures within the apparatus. Steel surface temperature, T_{Fe}, is measured with a type-S thermocouple that is spot-welded to the gap side of the steel plate. Figure 3.6 shows a representative plate with the thermocouple spot-welded to it. The thermocouple leads were fed through an alumina sleeve in the copper mold, and connected to the data acquisition system. Also shown in Figure 3.6 is a U-shaped spacer which was used to define the gap between the steel and copper. Two type-K thermocouples are placed at predefined depths within the flux gap to measure flux film temperatures, T_{G1} and T_{G2}. Two pairs of type-K thermocouples are silver-soldered into the copper mold to measure mold temperatures (T_{H1} and T_{C1}, T_{H2} and T_{C2}) and to calculate two sets of heat fluxes. Note that set 1 is near the center of the heat input, while set 2 is lower down. The thermocouples are connected through an A/D serial board, to a laptop data acquisition system. This setup is shown in Figure 3.7. Temperatures are recorded from each thermocouple every three seconds (0.33 Hz). The assembled apparatus is surrounded by refractory brick, zirconium paper, and Kao-wool to reduce heat losses. The assembled test fixture is shown in Figure 3.8.

3.2.1 Mold Flux Preparation

Mold powder samples were decarburized at 1100 ßC for about eight hours prior to each experiment. The powder was then melted in a graphite crucible inside an induction furnace. Argon was introduced through a layer of alumina insulation placed between the crucible and the furnace in order to protect the crucible from oxidation. The furnace s argon purge system is shown in Figure 3.9. Once the liquid flux reached about 200 ßC above its crystallization temperature, a sample of molten flux was scooped up with a steel spoon and poured into the top of the mold apparatus. The composition of each of the four mold fluxes tested is given in Table 3.1, along with other properties provided by the manufacturers.

3.2.2 Experimental Procedure

First, the mold apparatus was preheated with the torch until the steel temperature reaches about 1300 ˚C and the data acquisition system was started. Then, the liquid flux was poured into the apparatus, the cooling system was turned on, and the top covered with Kao-wool. Torch position was adjusted to maintain the steel temperature at about 1300 ˚C. Data was recorded for about 1-2 minutes. The torch was then moved to carefully lower the steel temperature in 100 ˚C increments to 900 ˚C. Temperature was maintained at each increment in order for steady state to develop. To investigate reproducibility and the importance of time in the apparatus, the steel temperature was increased to 1300 ˚C again and the step cooling sequence repeated. After the system had cooled to ambient, the apparatus was carefully taken apart and the final position of the gap thermocouples, flux layer thickness, and plate shape was measured. Finally, micrographs of the flux microstructures were taken.

Table 3.2 summarizes the conditions of the 16 experiments performed, which include three different initial gap sizes (1.5, 2.5, and 3.5 mm) for the four different mold fluxes. Gap sizes less than 1.5 mm were not obtainable with the design of this test apparatus, as liquid flux would solidify at the top of the gap opening, and not allow liquid to fill the gap. Figure 3.10 shows an example of this phenomenon.

Experiments one through three used an early design of the mold apparatus. There are two major differences between the two mold designs. The thermocouples within the early mold design were spaced two millimeters apart, whereas the spacing is 19 millimeters in the later design. The spacing was increased because thermocouple measurements in the early design produced temperature differences that were within the measurement error of the sensor (± 2.0 °C). Also, mold cooling systems differed between the two designs. Figure 3.11 shows the cooling system used in the earlier design. Holes were drilled in the copper block, and water flowed through these holes throughout operation. This configuration produced temperature gradients, which did not conform to the one-dimensional methodology of the experimental apparatus for measuring heat flow. The cooling system was redesigned to allow for more uniform cooling. Figure 3.3 shows the cooling coil that was used in the later design.

3.3 Data Analysis Methodology

The idealized temperature profile through the experimental apparatus during a typical test is shown in Figure 3.5. This figure defines the thermocouple temperatures and distances used in the following equations. It also illustrates the large size of the thermocouples relative to the gap dimensions. This is one source of uncertainty in the interpretation of the measurements, especially those in the gap.

Total heat flux was derived from each pair of thermocouples in the copper mold. As will be explained later in section 3.4.1.1, calculations using a 2-D model revealed that two-dimensional effects were negligible, so the following 1-D equation could be employed with reasonable accuracy:

$$\dot{q} = k_{Cu}\frac{(T_{H1} - T_{C1})}{d_C - d_H} \;\; or \;\; k_{Cu}\frac{(T_{H2} - T_{C2})}{d_C - d_H} \qquad (3.5)$$

Copper conductivity, k_{Cu}, was assumed to be 388 W/mK. [26]

3.3.1 One-Dimensional Model Formulation

Several sets of mathematical models were applied to the test data to compare the resulting predictions to previous literature findings. First, a set of one-dimensional models were applied to the test data, to obtain predictions for gap conductivity, flux film conductivity, contact resistance between mold and flux film, and contact resistance between flux film and steel. Some key assumptions were made of the test apparatus, in developing these models. It was assumed that the gap thickness, d_{gap}, did not change with time, and the position of the gap thermocouples did not move.

In the calculations that follow, different values are obtained depending on whether heat flux is calculated using mold thermocouples from set 1 or set 2. These can be compared to illustrate the variability. Effective conductivity across the gap is derived from the heat flux via:

$$
\begin{aligned}
k_{gap} &= \frac{\dot{q}\ d_{gap}}{T_{Fe} - T_{ICu}} \\
\textit{where} \quad T_{ICu} &= T_H + \frac{\dot{q}\ d_H}{k_{Cu}}
\end{aligned}
\qquad (3.6)
$$

The final gap thickness, d_{gap}, is included in Table 3.2, as the final location of the Fe thermocouple. Next, the gap thermocouples were used to isolate the relative contributions of radiation, conduction and contact resistance on the effective gap conductivity. Specifically, flux conductivity was estimated by:

$$
k_{flux} = \frac{\dot{q}\ (d_{G1} - d_{G2})}{T_{G1} - T_{G2}} \qquad (3.7)
$$

The flux/mold contact resistance was then estimated by:

$$
\begin{aligned}
R_{Cu} &= \frac{(T_{IG} - T_{ICu})}{\dot{q}} \\
\textit{where} \quad T_{IG} &= T_{G2} - \frac{\dot{q}\ d_{G2}}{k_{Flux}}
\end{aligned}
\qquad (3.8)
$$

The flux/steel contact resistance was estimated by:

$$
\begin{aligned}
R_{Fe} &= \frac{(T_{Fe} - T_{FeG})}{\dot{q}} \\
\textit{where} \quad T_{FeG} &= T_{G1} + \frac{\dot{q}\ (d_{gap} - d_{G1})}{k_{Flux}}
\end{aligned}
\qquad (3.9)
$$

3.3.2 Yamauchi Model Formulation

Next, models previously applied to test data from Yamauchi et al. [25] were applied to the present set of test data. Yamauchi models the effective thermal conductivity by defining a total thermal resistance, R_T, such that:

$$R_T = (R_{Fe} + R_{Cu}) + \frac{d_{flux}}{K_{flux}} \qquad (3.10)$$

When R_T is plotted against flux film thickness and a linear curve fit is applied to the test data, values for the flux thermal conductivity and interfacial resistance can be determined from the inverse of the slope and the intercept, respectively.

The Yamauchi model for radiative heat transfer across the interface assumes that the conductive and radiative heat fluxes act in an additive fashion towards their contribution to the total system heat flux:

$$q_{total} = q_{cond} + q_{rad} \qquad (3.11)$$

The conductive and radiative heat fluxes are formulated as:

$$q_{cond} = \frac{(T_{Fe} - T_{ICu})}{\left(\frac{d_{gap}}{k_{gap}} + R_{INT}\right)} \qquad (3.12)$$

$$\text{where } R_{INT} = R_{Fe} + R_{Cu} \qquad (3.13)$$

$$q_{rad} = \alpha_r \left(T_{Fe}^4 - T_{ICu}^4\right) \qquad (3.14)$$

$$\text{where } \alpha_r = \frac{n^2 \sigma}{\left(0.75 a d_{flux} + \varepsilon_m^{-1} + \varepsilon_s^{-1} - 1\right)} \qquad (3.15)$$

is the radiative heat transfer coefficient, in units of W/m^2K^4. Substituting Equations 3.12 through 3.15 into Equation 3.11, and assuming negligible contact resistance, gives:

$$\frac{q_{total}}{\left(T_{Fe}-T_{ICu}\right)}=\frac{1}{R_T}=\frac{k_{gap}}{d_{gap}}+\alpha_r\frac{\left(T_{Fe}^4-T_{ICu}^4\right)}{\left(T_{Fe}-T_{ICu}\right)} \qquad (3.16)$$

Thus by plotting ($1/R_T$) versus (T_{Fe}^4-T_{ICu}^4)/(T_{Fe}-T_{ICu}) and applying a linear curve fit to the data, the curve s slope is equal to the radiative heat transfer coefficient, and y-intercept is equal to the conductive thermal conductivity divided by the flux film thickness. The radiative heat flux can also be defined as:

$$q_{rad}=\frac{K_{rad}\left(T_{Fe}-T_{ICu}\right)}{d_{flux}} \qquad (3.17)$$

$$\text{where}\quad K_{rad}=\alpha_r d_{flux}\frac{\left(T_{Fe}^4-T_{ICu}^4\right)}{\left(T_{Fe}-T_{ICu}\right)} \quad (3.18)$$

is the radiative thermal conductivity, in units of W/mK.

3.4 Data Analysis: One-dimensional Model

Equations 3.5 through 3.9 were applied to the experimental data to model the system s thermal characteristics. Specifically, values for heat flux, conductivities of the gap and flux film, and contact resistances between the mold, flux film and steel were calculated.

3.4.1 Heat Flux Anomalies Observed from Model Calculations

Several observations were made from the test data. One of the most noticeable characteristics in the model calculations is the difference in heat flux values derived from the set 1 and set 2 thermocouples within the mold. In most of the experiments, set 2 values are greater than the set 1 values. Values for mold heat flux vary significantly for each experiment, with maximum differences approaching 35% or 0.1 MW/m^2 between set 1 and set 2 readings. Difference in heat flux values are largely attributable to increased temperature readings of the sensor, in set 2, that was closer to the mold hot face (surface closer to the flux film). Figure 3.12 shows an enlarged view of the mold temperatures during Experiment 8. Thermocouple readings near the cooling coil are almost identical in value. Differences between the hotface thermocouples are as large as 5 °C. This five-degree difference in sensor readings accounts for the 0.1 MW/m^2 variance in heat flux values obtained from the one-dimensional model. Experiments one through three exhibit the opposite behavior, as heat flux values derived from set 1 sensors are higher than those from set 2 sensors. Figure 3.13 shows an enlarged view of the mold temperatures during Experiment 3. Thermocouple readings show that both hot and cold-side readings for the set 1 sensors are higher than the set 2 hotface reading. Also, temperature differences between the set 1 thermocouples are slightly higher than the set 2 values. This system behavior is indicative of two or three-dimensional heat flow within the mold, possibly due to the early design of the mold cooling system (shown previously in Figure 3.11). Based on this analysis, the data in Experiments one through three should be considered biased since the one-dimensional heat transfer models do not apply here. This data will be evaluated in a qualitative aspect for comparison purposes only (i.e. behavior of Flux A compared to Flux B2, etc.).

Although the above analysis described why the heat flux measurements were giving different values, it was still unclear what caused the difference in thermocouple measurements. Possible mechanisms include: heat flow through the apparatus that didn t conform to the one-dimensional model assumptions, non-uniform heat flow into the apparatus, and deformation of the steel plate due to thermal expansion effects.

3.4.1.1 ANSYS Analysis

To investigate the possibilities of non-uniform system heat flow, a two-dimensional heat transfer model of the apparatus was developed, using ANSYS [27]. Figure 3.14 shows a schematic of the ANSYS model domain. This model attempts to quantify the effects of several boundary conditions on hotface thermocouple measurements. In particular, the effects of heat loss through the sides of the mold, non-uniform heat flow in the system from conduction through the wire spacer, and spatial variations in torch heat flux input. The model was verified by imposing a known set of boundary conditions, and comparing the model results with those of a one-dimensional analytical solution. The model domain was modified for the verification efforts, as contact resistance conductivities were all set to 2.5 W/mK and flux conductivities were the same as the steel spacer (27.0 W/mK). Figure 3.15 shows the modified model domain used for verification purposes. Table 3.3 compares results from the mathematical model to those of the analytical solution. Predictions from the mathematical model are directly comparable, within rounding errors, to those derived from the analytical solution.

Five different cases of boundary conditions were investigated using the ANSYS model. Table 3.4 provides the values of boundary conditions used in each case. Cases 1 and 2 vary the side heat loss coefficient from 0 to 10 W/m^2K to quantify the effect of side heat losses on the hotface mold thermocouples. Cases 2 and 3 vary the minimum torch heat values from 0.2 to 0.1 MW/m^2 to illustrate the effect of small differences in minimum torch heat values to hotface thermocouple temperatures. Cases 3 and 4 increase the minimum torch heat values from 0.1 to 0.4 MW/m^2 to compare bell-shaped torch heating profiles to uniform heating profiles. Cases 3 and 5 vary the maximum torch heating value from 0.5 to 1.0 MW/m^2 to illustrate the effect of torch heating gradients on hotface thermocouple readings. Table 3.5 shows values for the system parameters used in all cases.

Table 3.6 shows the results of the ANSYS parametric analyses, providing predictions of thermocouple readings for the different test cases. For Cases 1 and 2 (comparing effect of side heat losses), differences between hotface temperatures within each test case are approximately 0.1 °C for both set 1 and set 2 thermocouples. This behavior is also observed when comparing Cases 2 and 3 (effect of small variances of minimum torch inputs) and Cases 3 and 4 (effect of bell-shaped torch input to uniform torch input). Figure 3.16 shows a typical temperature contour plot for the test cases that were investigated. In comparing Cases 3 and 5 (effect of maximum torch input values), difference in set 1, 2 hotface temperatures are approximately 0.1 °C for Case 3 and 0.3 °C for Case 5.

From these parametric analyses, it is clear that side heat losses, torch heating profiles and variances in minimum heat flux values are not responsible for the differences in hotface thermocouple measurements in the mold powder experiments. Variances in maximum torch heat flux are possible mechanisms for thermocouple differences, although they don t account for the total magnitude of measurement variances (0.3 versus 5.0 °C). The most likely cause for the difference in hotface thermocouple readings is thermal distortion of the steel plate due to the torch heat input. The set 1 thermocouples were closer to the center of the mold (see Figure 3.4) where the flux layer was thicker due to outward distortion of the steel plate. Figure 3.17 compares the initial and final flux layer thicknesses and plate dimensions for different locations and experiments. This figure shows that the final flux layer is always about 10% thicker near the center. Figure 3.17 also confirms that the plate expands the most in the center. It is likely that this expansion away from the flux film generates a slightly larger air gap at the center, which also contributes to the set 1 values being lower. Only the final dimensions could be measured, but the evolution of the plate shape during the experiment is likely responsible for most of the differences between the two thermocouple sets.

3.4.2 Investigation of Temperature Transients at Time of Flux Pour

A striking feature, observed in all experiments, is a sharp spike in the temperature of all thermocouples in the first few seconds after pouring the liquid flux into the mold. An apparent spike in the heat flux and gap conductivity accompanies this phenomenon. Calculations using a simple transient model predict that the thin layer of mold flux should solidify against the chilled copper in one to five seconds, depending on the gap thickness. During this brief initial time, heat is supplied to the mold by the heat content of the molten flux and not by a high rate of conduction. The recorded peaks in both the gap thermocouples and mold surface temperatures are consistent with these calculations. A similar effect is likely to occur at the meniscus in an operating caster. Steady state is reached after only a few seconds, so this transient effect does not explain the persistence of high temperatures, and correspondingly high heat fluxes, that are observed after longer times in some experiments.

Just after pouring in the flux, the steel surface temperature dips slightly, which causes a corresponding drop in all of the temperatures. This is due to the delay in increasing heat input from the torch to maintain the greatly increased heat transfer across the now-highly conductive gap. This is a second reason for the sharp initial drop in heat flux.

3.4.3 Application of 1-D Heat Flux Model

Figures 3.18 through 3.21 show mold heat flux calculations as a function of steel temperature for fluxes A, B2, C, and D. Legends for these figures, as well as for those presenting one-dimensional model calculations, depict the experiment and the initial gap thickness for each set of data shown. Several measured values for final gap thickness are shown in Table 3.2, although not all gap thicknesses were measured. Values for mold heat flux vary linearly with temperature, and increase with decreasing gap thickness. Heat flux values for flux A range from 0.05 to 0.3 MW/m^2. Heat flux values for flux B2 range from 0.1 to 0.35 MW/m^2. Heat flux values for flux C range from 0.06 to 0.34 MW/m^2. Heat flux values for flux D range from 0.06 to 0.4 MW/m^2. Note that the model used to calculate heat flux is derived completely from mold sensor parameters, and do not depend on gap parameters.

3.4.4 Application of 1-D Gap Conductivity Model

Figures 3.22 through 3.25 show gap conductivity calculations as a function of steel temperature for fluxes A, B2, C, and D. In general, values for gap conductivity increase linearly as temperature increases. As representative of flux properties for flux A, its gap conductivity displays no significant trend or behavior. As explained earlier, flux A was tested with an earlier version of the test apparatus, and differences in mold thermocouple measurements were within the sensors error ranges. In experiment 3, which displayed the most consistent behavior of the flux A experiments, values for gap conductivity ranged from 0.4 to 0.85 W/mK. Experiments for fluxes B2 through D represented similar behavior, as gap conductivity increased linearly with temperature. At specific steel temperatures, calculated values for gap conductivity spanned as much as 0.5 W/mK. Gap conductivity values for flux B2 range from 0.3 to 0.75 W/mK. Gap conductivity values for flux C range from 0.28 to 0.8 W/mK. Gap conductivity values for flux D range from 0.27 to 0.8 W/mK. Values calculated using the 1-D gap conductivity model compare well with thermocouple measurements of the steel temperature, as there is a direct relationship between steel temperature and gap conductivity.

3.4.5 Application of 1-D Flux Conductivity Model

Figures 3.26 through 3.29 show flux conductivity calculations as a function of steel temperature for fluxes A, B2, C, and D. Flux conductivity values for flux A, that were replicated several times, range from 0.7 to 1.5 W/mK. Flux conductivity values for flux B2 range from 0.3 to 4.9 W/mK. Flux conductivity values for flux C range from 0.5 to 4.0 W/mK. Flux conductivity values for flux D range from 0.25 to 2.1 W/mK.

From looking at the graphs of flux conductivity versus steel temperature for the four mold powders analyzed, it is apparent that flux conductivity values calculated from the one-dimensional model do not always exhibit a linear dependence on steel temperature. Although the majority of the data does show a linear-like profile, a few experiments exhibit behavior that questions the validity of the assumptions made in deriving the model equations. Recall that the gap dimensions, including position of the thermocouples within the flux film, were assumed to be fixed and not able to move with time. In comparing Figures A and D for each experiment, Experiments 5, 8, and 10 stand out as cases which do not behave as expected. Figure 3.30 plots steel temperature, gap thermocouple temperatures, and flux conductivity versus time for Experiment 5. Calculated values for flux conductivity appear to increase (from 2.44 to 4.89 W/mK) as steel temperature decreases (from 1240 to 1105 C) between 600 and 850 seconds from time of pour. During this time in the experiment, differences in gap thermocouple temperatures decrease in a pattern that isn't replicated elsewhere in the experiment. According to Equation 3.7, as the difference between TG1 and TG2 decrease, calculated values of flux conductivity should increase. Two possible mechanisms can explain this behavior: either the conductivity of the mold flux film does indeed increase in this region (perhaps due to some crystallization phenomena), or the position(s) of the thermocouples within the flux film move. Figure 3.31 plots steel temperature, gap thermocouple temperatures, and flux conductivity versus time for Experiment 8. Calculated values for flux conductivity appear to decrease (from 2.2 to 0.9 W/mK) as steel temperature increases (from 1100 to 1300 C) between 98 and 365 seconds from time of pour. In a familiar phenomena representative of Experiment 5, differences in gap thermocouple temperatures increase in this region, in a manner that is not replicated elsewhere in the experiment.

As shown in Figure 3.32, Experiment 10 exhibits behavior that seems like a combination of what occurs in Experiment 5 and 8. Calculated values for flux conductivity appear to increase (from 2.1 to 3.7 W/mK) as steel temperature decreases (from 1300 to 900 C) between 235 to 815 seconds from time of pour, and appear to decrease (from 3.7 to 1.52 W/mK) as steel temperature increases (from 900 to 1300 C) between 830 to 1040 seconds from time of pour. These behaviors in gap thermocouple reading do not appear to be attributable to solidification phenomena, as they do not occur near or within quantified temperatures corresponding to crystallization or solidification (approximately 1135 to 1180 C) of the B2 and D mold powders tested with these experiments. Movement of the gap thermocouples from their initial positions seems to be a plausible mechanism for these three circumstances. All cases show a decrease in gap thermocouple temperature differences as steel temperature decreases. Likewise, gap thermocouple temperature differences increase as steel temperature decreases. This behavior mimics somewhat of a compressive characteristic of the flux film. By noticing that this behavior is only seen within the first temperature cycle between 1300 and 900 C suggests that this compressive behavior is present at temperatures above a critical point where the flux film becomes rigid.

The analysis of the 1-D gap conductivity calculations has provided evidence to question the assumption that was made, of the gap thermocouples not moving throughout the experiment. As will be discussed in the following sections, contact resistance values will also be affected by this discovery.

3.4.6 Application of 1-D Mold/Flux Contact Resistance Model

Figures 3.33 through 3.36 show mold/flux contact resistance calculations as a function of steel temperature for fluxes A, B2, C, and D. Mold/flux contact resistance values for flux A, that were replicated several times, range from 0.0002 to 0.0018 m^2K/W. Mold/flux contact resistance values for flux B2 range from 0.0001 to 0.0031 m^2K/W. Mold/flux contact resistance values for flux C range from 0.0001 to 0.003 m^2K/W. Mold/flux contact resistance values for flux D range from 0.0002 to 0.003 m^2K/W.

Values for the contact resistance between the mold and flux film for the present set of experiments vary widely. Also, the higher contact resistance limits do not agree with the numerous findings [3, 18, 25] of mold/flux contact resistances on the order of 20 to 50 μm in thickness (0.0003 to 0.0008 m^2K/W). As described in Equation 3.8, model calculations for the mold/flux contact resistance depends on the heat flux, as well as mold hotface temperatures extrapolated from both flux (T_{IG}) and copper (T_{ICu}) media. While mold parameters such as heat flux, thermocouple location and copper conductivity are well defined, parameters within the flux film, such as gap thermocouple position and flux conductivity, are much less defined. The previous section looked at examples of uncharacteristic changes in flux conductivity calculations, which could be explained by movement of the gap thermocouple from their original pre-test locations. If gap thermocouple movement was responsible for this behavior then calculated values of the flux-extrapolated hotface temperature T_{IG} should be examined for their validity. Parameters that define the flux-side hotface temperature are the heat flux, temperature and position of the T_{G2} gap thermocouple, and the calculated flux conductivity. It is apparent from Equation 3.8 that the flux-side hotface temperature is highly dependent on gap parameters which are somewhat uncertain in their accuracy, based on 1-D model behavior. It is difficult to support the values for mold/flux contact resistance which are calculated from these 1-D models after the first five to ten seconds when the flux should logically solidify against the mold and form a fixed contact resistance thickness.

3.4.7 Application of 1-D Flux/Steel Contact Resistance Model

Figures 3.37 through 3.40 show flux/steel contact resistance calculations as a function of steel temperature for fluxes A, B2, C, and D. Flux/steel contact resistance values for flux A, which were repeated several times, range from 0.00005 to 0.0015 m^2K/W. Flux/steel contact resistance values for flux B2 range from 0.0003 to 0.005 m^2K/W. Flux/steel contact resistance values for flux C range from 0.0005 to 0.003 m^2K/W. Flux/steel contact resistance values for flux D range from 0.0002 to 0.0035 m^2K/W. The minimum contact resistance values seem to agree with reported measurements of 20-50 μm. However, the maximum contact resistance values seem significantly larger than any reported values, with thicknesses reaching between 90 and 310 μm. Values of contact resistance between the flux film and steel show several trends of behavior ranging from following the steel temperature in a linear fashion, to behaving inversely to the steel temperature, to being insensitive to steel temperature fluctuations. Several mechanisms could explain this unpredictable behavior of the contact resistance values. One mechanism is that these contact resistances do not follow predictable behaviors, which does not seem believable. Another mechanism is that the mold flux behavior that aids to forming contact resistances is extremely sensitive to process parameters such as heat flux, temperature and temperature gradients. These types of process parameters vary with time and experiment, so this mechanism could possibly explain this contact resistance behavior. Another mechanism is the combined effects of steel and flux film expansion and contraction coefficients, as these coefficients may depend differently on temperature and temperature gradient. A fourth possible mechanism is movement of the gap thermocouples within the gap, coupled with the thermal expansion effects of the steel and flux film. This mechanism seems the most likely, based on the results of the previous sections dealing with flux conductivity and mold/flux contact resistance calculations.

3.4.8 Review of 1-D Transient Model Results

In reviewing the values of heat flux, gap and flux conductivity, and mold/flux and flux/steel contact resistance, numerous examples seen within various experiments suggest that the assumptions made in developing the 1-D models may not be valid for these circumstances. In particular, the assumptions of gap thickness and gap thermocouples not changing during the experiments do not hold true at all times. Post-test measurements of gap thermocouple position, solidified flux thickness, and steel plate distortion (as shown in Table 3.2 and Figure 3.17) validate these concerns. While the behavior of the gap sensors is not quantified, and extremely difficult to derive from the test data, calculated values for the mold flux properties of concern (gap and flux conductivities) are within reported values in the literature and will be used for the rest of this study. Future work should focus on quantifying the behavior of the steel plate and gap thermocouples, and their influence on flux film and gap conductivity values.

3.4.9 Mold Flux Microstructure

Figures 3.41 and 3.42 show the final microstructures of sections of the gap taken through typical solidified flux samples. The particular fluxes illustrated, C and D, exhibit a complex multiple layered structure that is similar in appearance to flux samples removed from operating continuous casting molds. More different layers can be distinguished by their unique colors than is obvious in these two figures. Most of the layers appear mainly crystalline, which could explain the apparent lack of sensitivity of the conductivities to temperature. This is consistent with the findings of Mills that radiation makes less than a 10% difference to the heat transfer. Only samples taken of flux A revealed a fully glassy structure.

These microstructures also reveal many voids that are believed to be gas bubbles that are evolved during solidification of the flux. These gas bubbles were clearly visible in every sample, except for the glassy flux A. This finding is consistent with the observations of Cramb and coworkers [28], who photographed such gas bubble formation during solidification of small samples of mold flux. Figure 3.41 shows that the bubbles sometimes form in just one of the layers, in this case the center. The drop in conductivity that should accompany these bands of gas voids is consistent with the observed low conductivity of the three crystalline fluxes.

3.4.10 Analysis of 1-D Steady-State Model Results

The transient data collected for each experiment was divided into data points according to time periods where conditions such as temperature remained constant for at least 100s. Plots of conductivity and interface resistance were made for these data points in order to investigate the effects of gap thickness, temperature, and powder composition on the thermal properties.

Figure 3.43 shows the gap conductivity results, based on Equation 3.6. Figure 3.44 shows the flux conductivity predictions, based on Equation 3.7. There is a great of scatter in the results, and no significant trends can be seen for the effect of gap thickness or steel surface temperature on either of these conductivities. The gap conductivity ranges from 0.3-0.7 W/mK (0.6 average). The flux conductivities are always higher and have more scatter, with a range of 0.5-2.0 W/mK (1.0 average).

An interesting observation is that flux A had a much higher conductivity in one experiment (# 2) (0.9 W/mK gap conductivity). The observation of higher conductivity for flux A is consistent with its observed glassy structure, relative to the mainly crystalline structures of the other fluxes (B2, C, and D). This finding suggests that crystallinity is the only significant effect of flux composition on thermal properties, which agrees with the previous findings of Mills.

Figures 3.45 and 3.46 show that the interface resistances also exhibit a great deal of scatter. They are also relatively insensitive to temperature, flux composition, and gap thickness. It is interesting that both interface resistances are equally large, ranging from 0 - 0.003 m^2-K/W. The mold/flux resistance sometimes showed negative values, which indicates both excellent contact and experimental error (variation). It was expected that the contact resistance should drop when temperature increases above the flux melting temperature, especially at the flux/steel interface. This was not observed, which implies that the minor increase in plate warping at higher temperatures was more important.

3.5 Data Analysis: Yamauchi Model Correlation

To compare the test data to values reported in the literature, mathematical models derived by Yamauchi, and shown in Equations 3.10 to 3.18, were applied to the present test data. Values for flux film thickness were measured from samples taken from the experimental apparatus, which are shown graphically in Figure 3.17. Measurements taken from the center of the test apparatus are used for test data correlation, as they were in close proximity to the temperature measurements used in this effort.

Table 3.7 presents the results of plotting total gap resistance, R_T, against $(T_{Fe}^4-T_{ICu}^4)/(T_{Fe}-T_{ICu})$ for the four different mold powders tested, to derive the gap conductivity, k_{gap}, and radiation heat transfer coefficient, α_r. Values for gap conductivity ranged from 0.37 to 0.60 W/mK, while values for the radiation heat transfer coefficient ranged from 5.02E-9 to 3.55E-8 W/m^2K^4. Gap conductivity values derived from the Yamauchi model compare well with values that were derived from the one-dimensional model, and are on the same order as those found in the literature (0.3 to 1.3 W/mK) [21, 25]. Also, radiation heat transfer coefficient values are on the same order as those reported by Yamauchi [25], although it is apparent that conduction across the flux film and contact resistances overshadowed any radiation effects. Radiation heat transfer effects across the flux film were negligible in the overall heat flux calculations. Measurements during experiments for mold powder A were not consistent enough to produce valid results from the model.

Table 3.8 presents the results of plotting total gap resistance, R_T, against flux film thickness, from Equation 3.10, for the different mold powders to derive the flux conductivity, k_{flux}, and total system interfacial resistance, $(R_{Cu}+R_{Fe})$. Figures 3.47 through 3.49 show plots of total gap resistance versus flux film thickness for Flux B2, C, and D, respectively, along with the linear curve fits through the data points. Values for flux conductivity ranged from 0.51 to 1.15 W/mK, while values for total system interfacial resistance ranged from 0.0008 to 0.0040 m^2K/W. Flux conductivity values compare closely with those reported in the literature (0.3 to 2.1 W/mK), as well as the low-end values for the interfacial thermal resistance. High-end values of the interfacial thermal resistance are not largely seen in the literature. These values correspond to an air gap of about 0.25 mm thickness, which wouldn t normally occur in a continuous caster except in corners where the shell always pulls away from the mold. Values of interfacial thermal resistance are slightly higher for the set 1 measurements, which would be explained by the measured plate distortion profiles that show larger plate bowing near the middle of the mold where the set 1 sensors are located.

The values calculated from the Yamauchi models are based on parameters which were directly measured in the present experiments (steel temperature, flux film thickness), or on parameter values extrapolated from the well-defined mold configuration. These values are less likely to be influenced by apparatus behavior and/or error which is not quantifiable from the test data (such as movement in gap thermocouple position). However, the Yamauchi model for radiation neglects the presence of contact resistances, which were prominent in the present work. Future work will focus on expanding the Yamauchi radiation model to account for contact resistances, as well as expanding the one-dimensional models to filter out the contact resistances effects on flux and gap conductivity predictions.

3.6 Summary

A series of experiments were conducted to simulate the thermal behavior of casting fluxes during initial solidification of a steel slab. An apparatus was constructed to simulate the gap that is formed between the steel shell and water-cooled copper mold. Thermocouples were placed in the copper mold, on the steel shell, and in the simulated gap area to measure flux film temperatures and mold heat flux. A set of one-dimensional models were applied to the experimental data to evaluate several thermal characteristics of the apparatus and flux film, including mold heat flux, gap conductivity, flux conductivity, and contact resistances between the mold and flux film, and between the flux film and steel. Models from the literature were also applied to the experimental data, which produced conductivity and contact resistance values which compared well with those reported in the literature. This information was used to predict shell growth in a continuous cast, stainless steel slab which was obtained from a breakout event that occurred at the Armco slab caster in Mansfield, Ohio. The following section will describe the breakout conditions in detail, and compare measured shell parameters with those predicted from the CON1D mathematical model.

Table 3.1: Compositions (mass percent) and other Properties of Tested Mold Powders

	Flux A	Flux B2	Flux C	Flux D
SiO_2	33.80	29.93	38.40	40.80
CaO	33.90	39.41	39.20	36.70
Al_2O_3	6.20	4.58	5.00	5.60
MgO	2.40	0.79	3.40	3.40
Na_2O	10.60	9.04	2.00	2.16
F	5.70	12.93	9.30	7.20
Total Carbon	4.10	2.18	2.60	
CaO/SiO_2	1.00	1.32	1.02	0.90
Viscosity at 1300 C (poise)	2.30	0.30	2.00	4.00
Crystallization Temperature (C)	1146	1180	1135	1110

Table 3.2: Experimental Conditions

Experiment	Mold Flux	Initial Gap (mm)	Final Gap (mm)	Thermocouple locations (distance from mold hot face - mm)*					
				G1	G2	H1	C1	H2	C2
1	A	2.5	N/A	2.00	0.75	-1.0	-3.0	-1.0	-3.0
2		3.5	N/A	3.00	1.50	-1.0	-3.0	-1.0	-3.0
3		3.5	N/A	3.00	1.50	-1.0	-3.0	-1.0	-3.0
4	B2	2.5	3.0	2.00	1.00	-1.0	-20.0	-1.0	-20.0
5		2.5	2.8	2.54	1.32	-1.0	-20.0	-1.0	-20.0
6		3.5	N/A	3.00	1.50	-1.0	-20.0	-1.0	-20.0
7		3.5	N/A	2.82	1.64	-1.0	-20.0	-1.0	-20.0
8	C	2.5	2.7	1.92	1.23	-1.0	-20.0	-1.0	-20.0
9		2.5	3.1	2.39	1.02	-1.0	-20.0	-1.0	-20.0
10		3.5	N/A	3.00	1.55	-1.0	-20.0	-1.0	-20.0
11	D	1.5	1.7	1.23	0.51	-1.0	-20.0	-1.0	-20.0
12		1.5	N/A	1.00	0.50	-1.0	-20.0	-1.0	-20.0
13		2.5	N/A	2.00	1.00	-1.0	-20.0	-1.0	-20.0
14		2.5	N/A	2.00	1.00	-1.0	-20.0	-1.0	-20.0
15		3.5	3.8	3.11	1.97	-1.0	-20.0	-1.0	-20.0
16		3.5	4.0	3.20	1.50	-1.0	-20.0	-1.0	-20.0

* negative numbers reference distances towards back of mold
N/A: Final gap dimensions were not measured

Table 3.3: Comparison of ANSYS Results with 1-D Analytical Solution

Temperature	1-D Analytical Solution (C)	2-D ANSYS Model Results (C)
T_1	1381.15	1381.16
T_2	1322.35	1322.37
T_3	572.35	572.367
T_4	528.26	528.274
T_5	286.60	286.614
T_6	253.87	253.882
T_7	37.27	37.2764
T_8	25.0	25.0

Table 3.4: Summary of Boundary Conditions used in ANSYS Analysis

	Case 1	Case 2	Case 3	Case 4	Case 5
Max Q(r) (MW/m^2)	0.5	0.5	0.5	0.5	1.0
Min Q(r) (MW/m^2)	0.2	0.2	0.1	0.4	0.1
Side Heat Loss Coefficient h (W/m^2K)	10	0	0	0	0
Liquid Flux Conductivity (W/mK)	1.0	1.0	1.0	1.0	1.0
Solid Flux Conductivity (W/mK)	1.0	1.0	1.0	1.0	1.0

Table 3.5: System Parameter Values for ANSYS Model Analyses

Material	Thermal Conductivity (W/mK)	Thickness (mm)
Steel Plate	27.0	3.175
Contact Resistance 3	0.06	0.09
Contact Resistance 1,4,5	0.06	0.03
Liquid Flux	1.0	1.191
Solid Flux	1.0	1.191
Steel Spacer	27.0	2.5
Contact Resistance 2	0.06	0.06
Mold	388.0	25.4
Cooling Coil	388.0	9.525

Table 3.6: Results of ANSYS Analyses of Test Apparatus

	Case 1	Case 2	Case 3	Case 4	Case 5
T_{fe} (°C)	1184.9	1186.1	1039.5	1479.1	4098.1
T_{G1} (°C)	732.5	733.3	635.1	929.7	2814.2
T_{G2} (°C)	420.3	465.4	398.6	543.9	2237.1
T_{H1} (°C)	178.2	178.6	145.8	244.4	457.1
T_{C1} (°C)	165.7	166.1	135.5	227.3	412.5
T_{H2} (°C)	178.3	178.7	145.8	244.5	457.4
T_{C2} (°C)	165.8	166.1	135.5	227.4	412.8

Table 3.7: Yamauchi Model Calculations for Gap Conductivity, Radiation Heat Transfer Coefficient

Flux: mold sensors used to measure heat flux	Gap Conductivity k_{gap} (W/mK)	Radiation Heat Transfer Coefficient α_r (W/m^2K^4)
A: set 1	*	*
A: set 2	*	*
B2: set 1	0.38	1.29E-8
B2: set 2	0.56	1.38E-8
C: set 1	0.44	5.02E-9
C: set 2	0.60	3.55E-8
D: set 1	0.37	1.50E-8
D: set 2	0.54	2.68E-8

*: Not reliable due to measurement error (close proximity of two Cu thermocouple locations)

Table 3.8: Yamauchi Model Calculations for Flux Conductivity, Interfacial Thermal Resistance

Flux: mold sensors used to measure heat flux	Flux Conductivity k_{flux} (W/mK)	Interfacial Thermal Resistance ($R_{Cu}+R_{Fe}$) (m^2K/W)
A: set 1	*	*
A: set 2	*	*
B2: set 1	0.81	.0026
B2: set 2	0.92	.0012
C: set 1	1.15	.0040
C: set 2	0.80	.0008
D: set 1	0.51	.0009
D: set 2	0.96	.0014

*: Not reliable due to measurement error (close proximity of two Cu thermocouple locations)

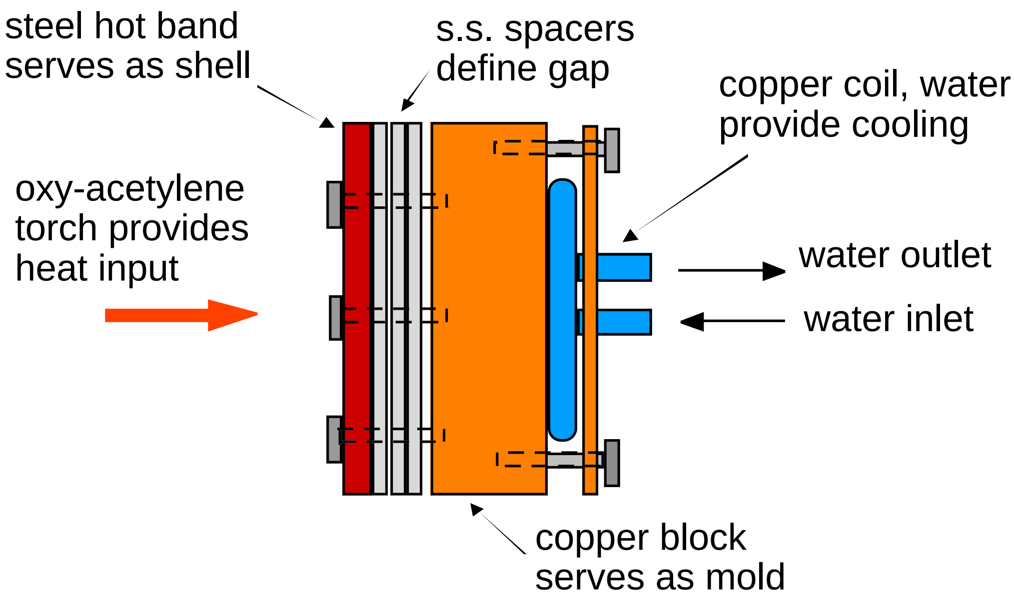

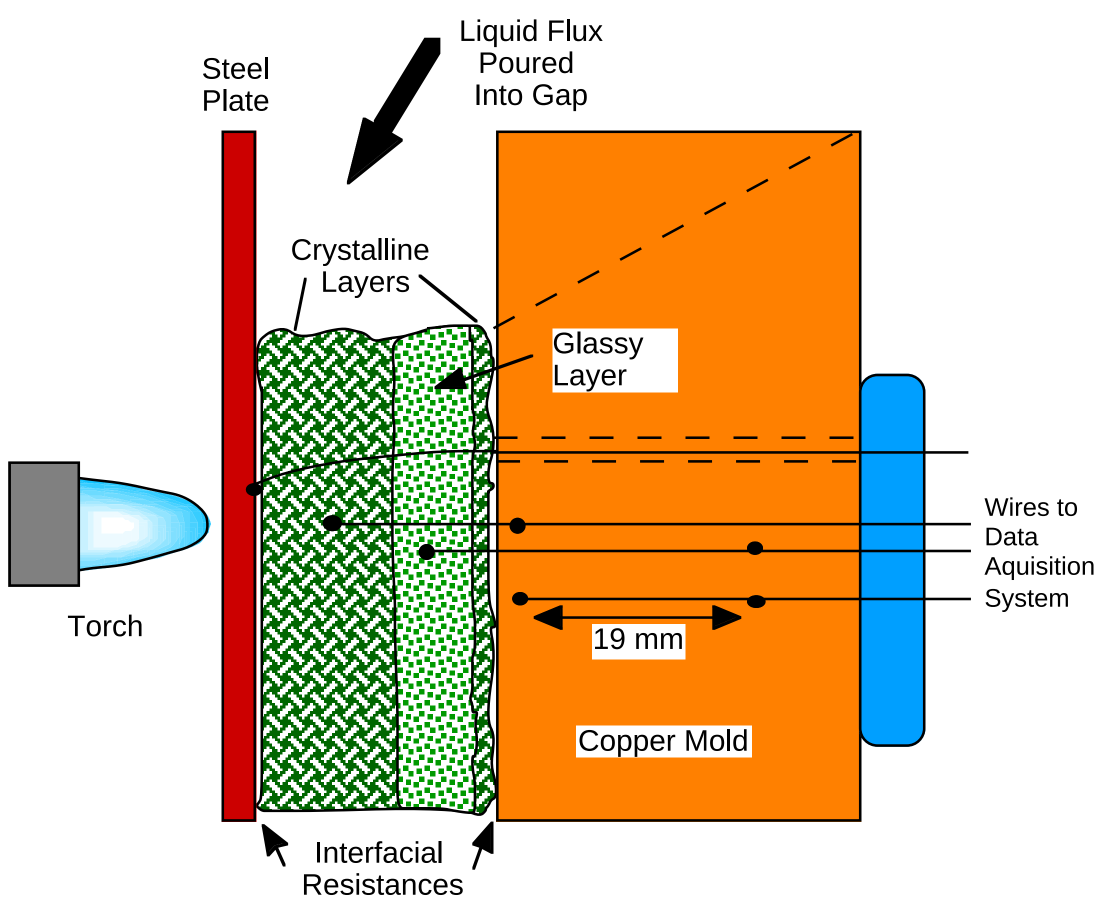

Figure 3.1: Schematic of Test Apparatus

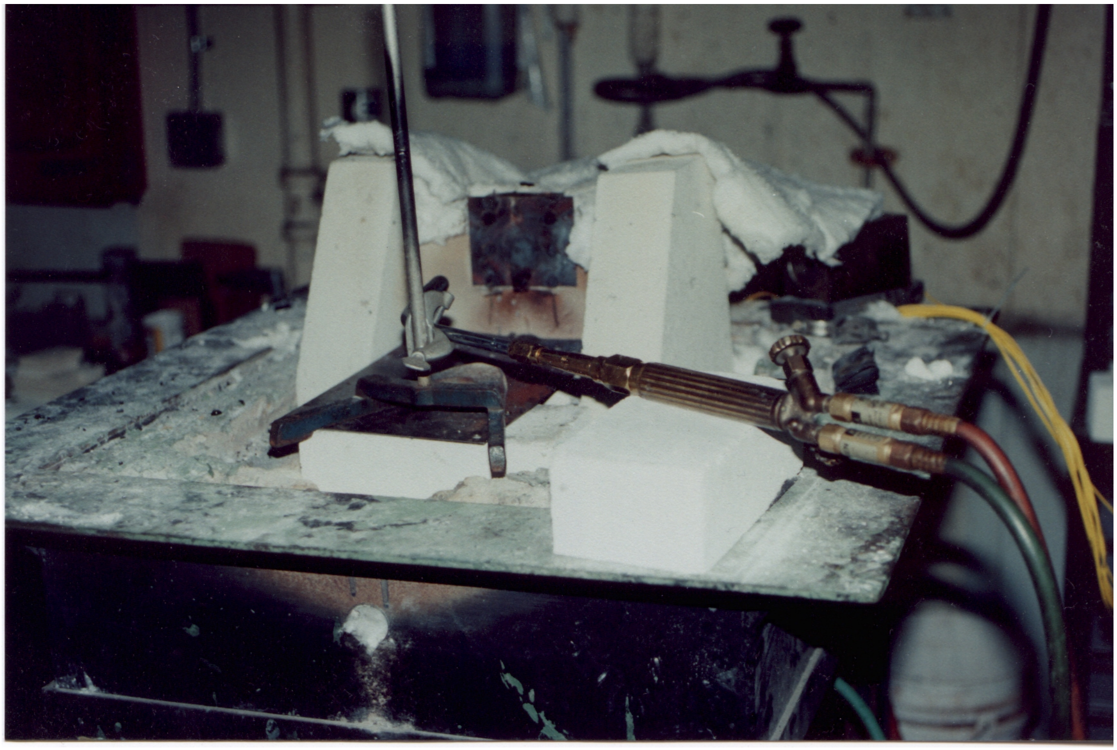

Figure 3.2: Assembled Test Fixture, with Torch Heat Input

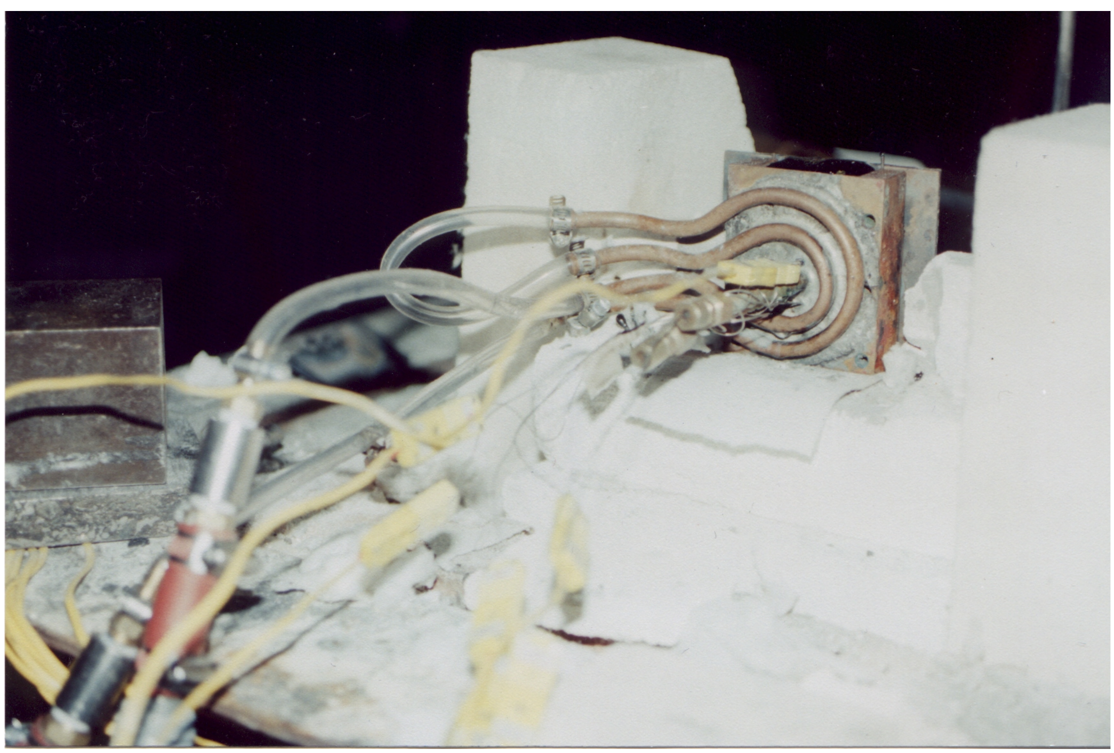

Figure 3.3: Mold Cooling System, showing thermocouple Connectors

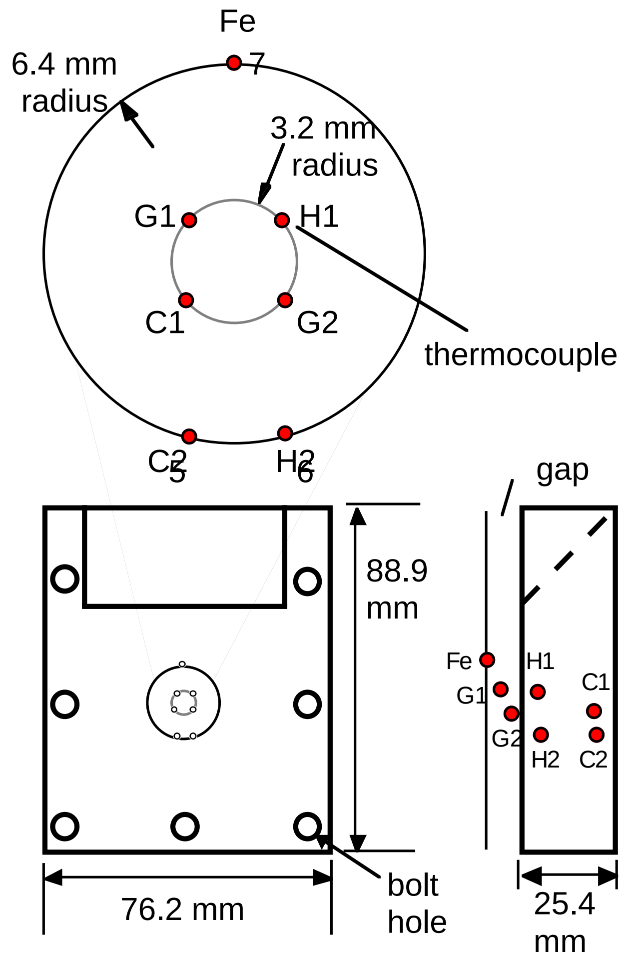

Figure 3.4: Layout of thermocouples through test apparatus

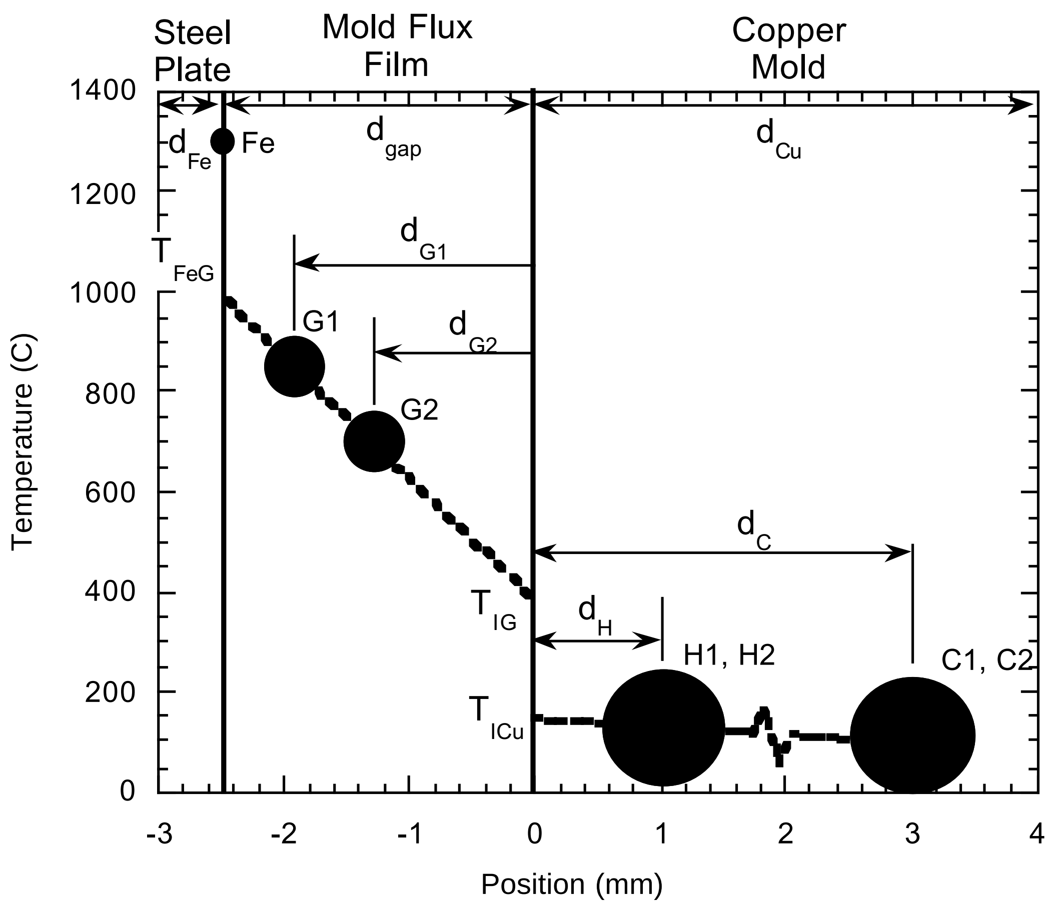

Figure 3.5: Temperature Gradients through test apparatus

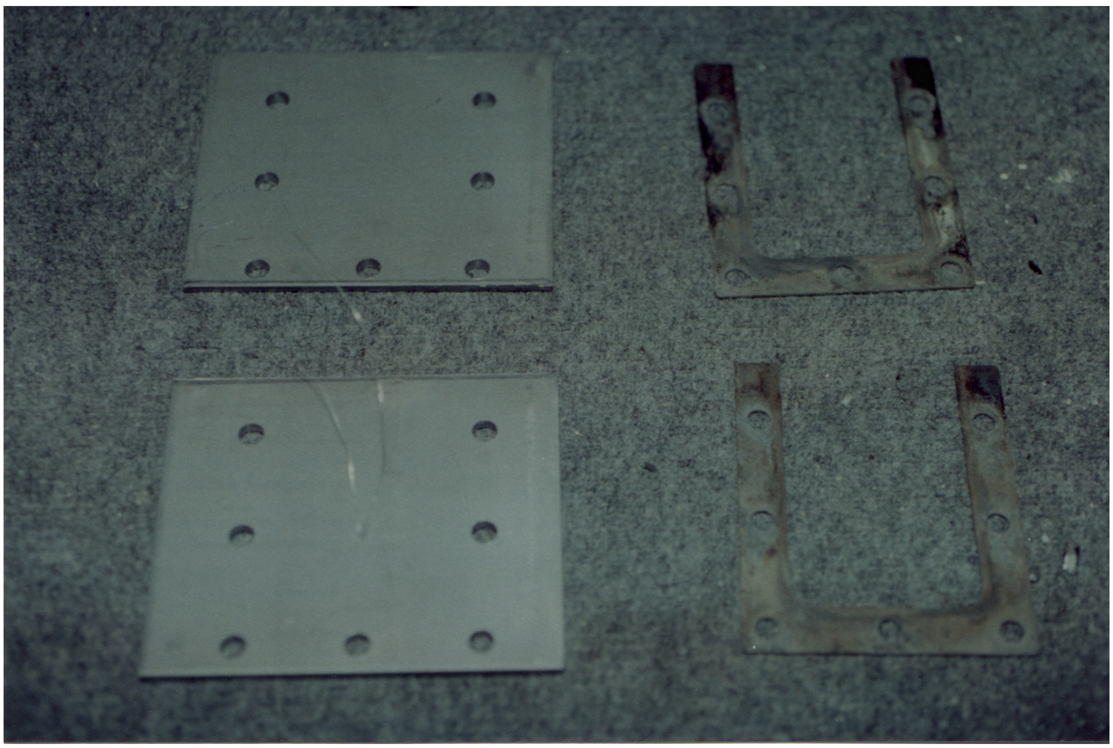

Figure 3.6: Spot-Welded S-type thermocouple attached to steel plate, along with U-Shaped Spacers to set Gap Displacement

Figure 3.7: Data Acquisition System Setup

Figure 3.8: Close-up of Test Fixture and Torch, showing Insulation Closeouts with Refractory Brick and Kao-Wool

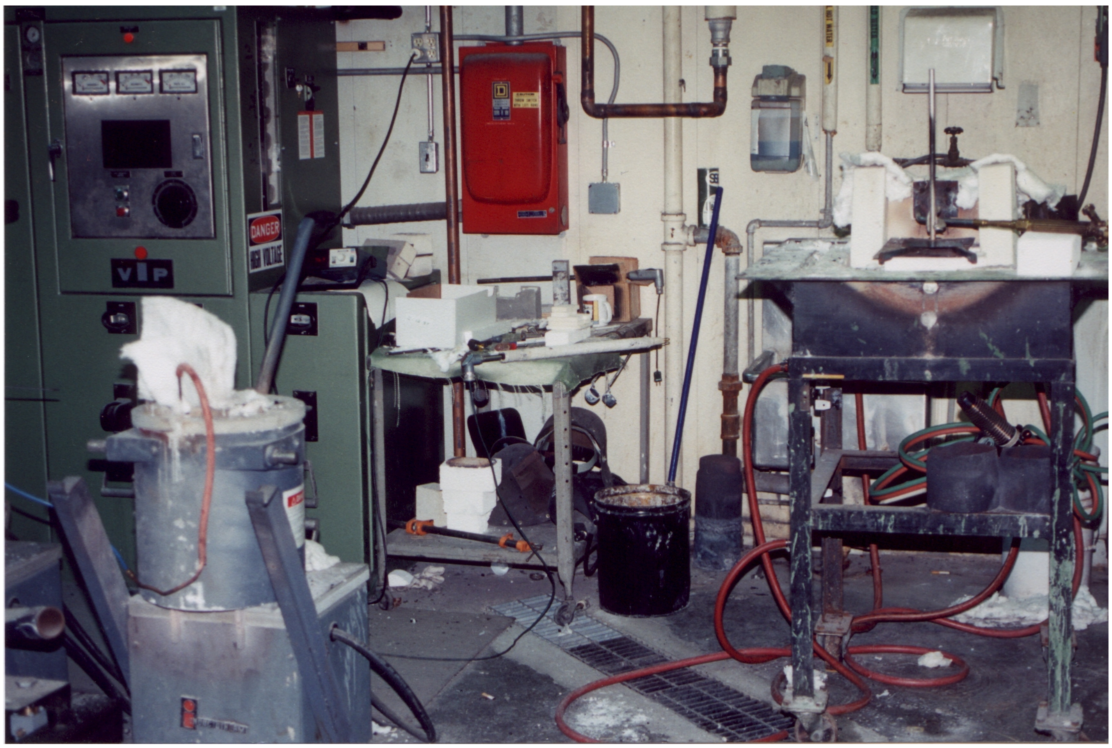

Figure 3.9: Induction Furnace Setup, with Argon Purge

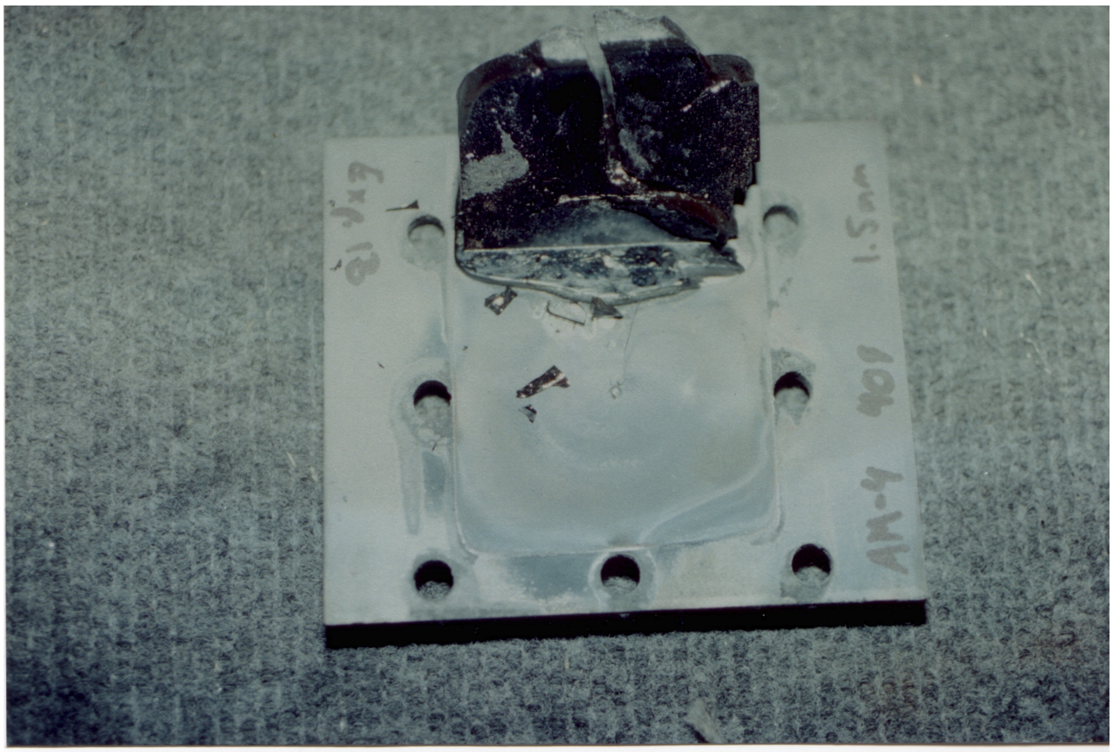

Figure 3.10: Example of Incomplete Filling of flux gap between Mold and Steel

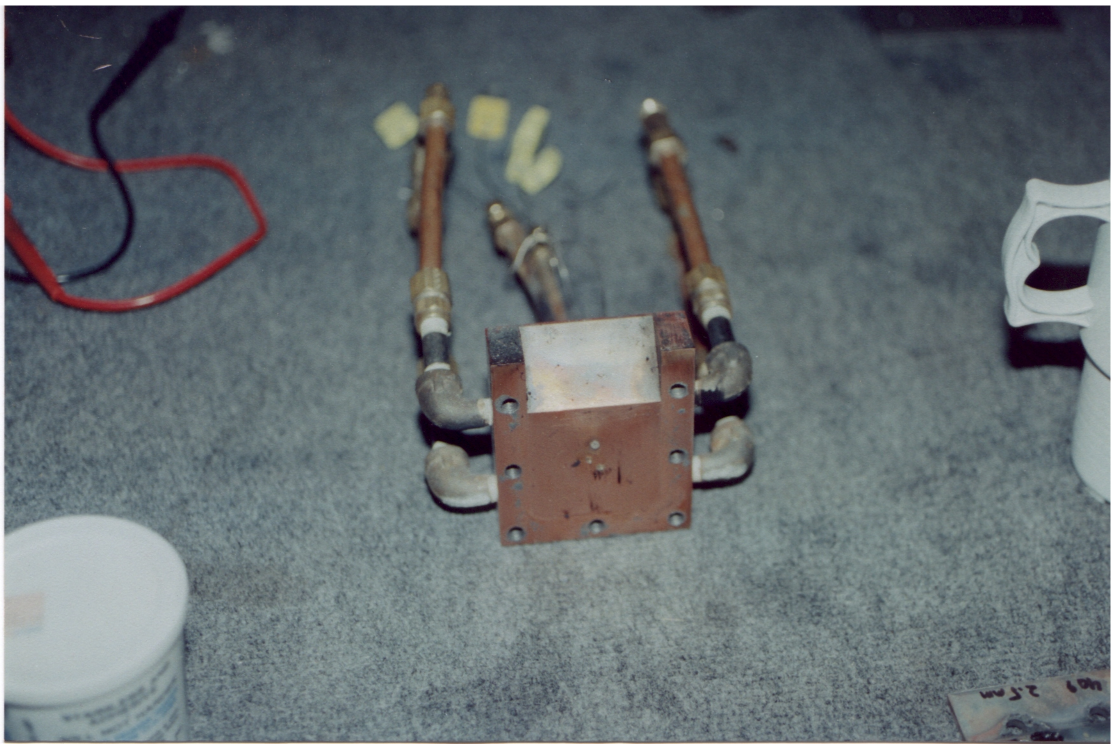

Figure 3.11: Early Design of mold apparatus, showing old mold cooling system

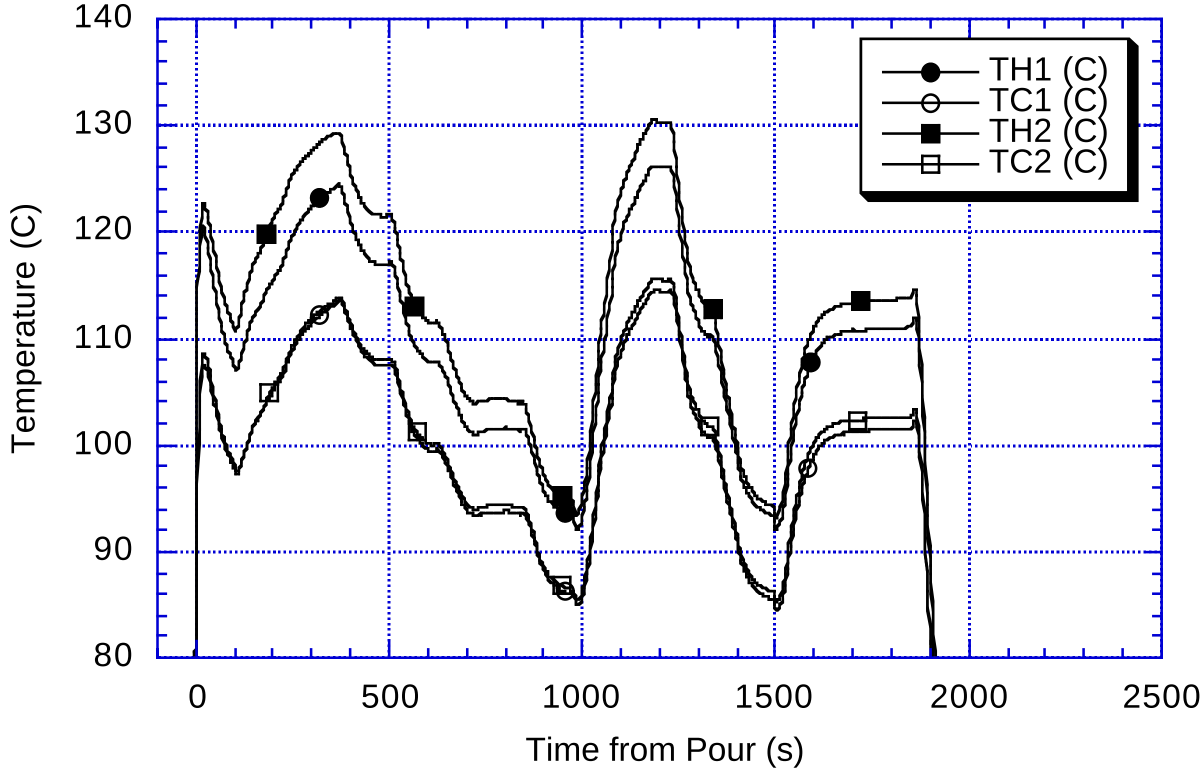

Figure 3.12: Close-up View of Mold Temperature Measurements during Experiment 8, showing variance between hotface temperature readings

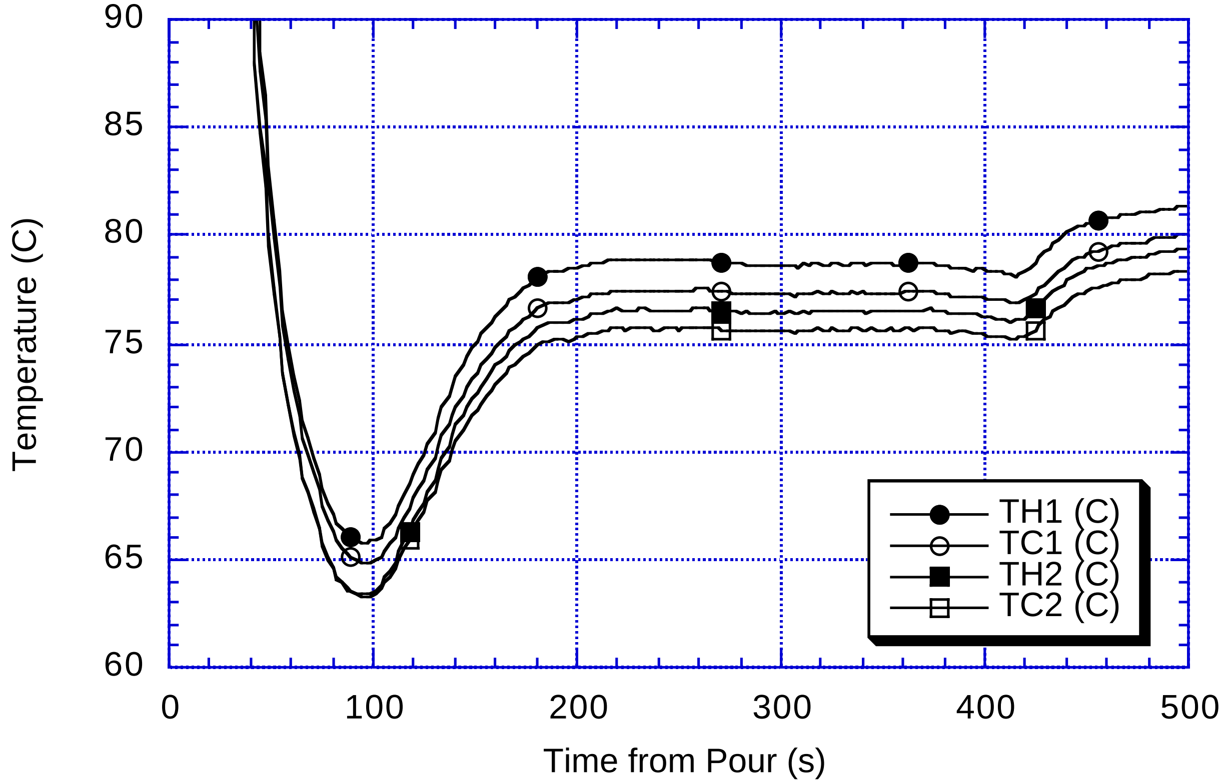

Figure 3.13: Close-up view of Mold Temperature measurements during Experiment 3, showing error in sensor measurement

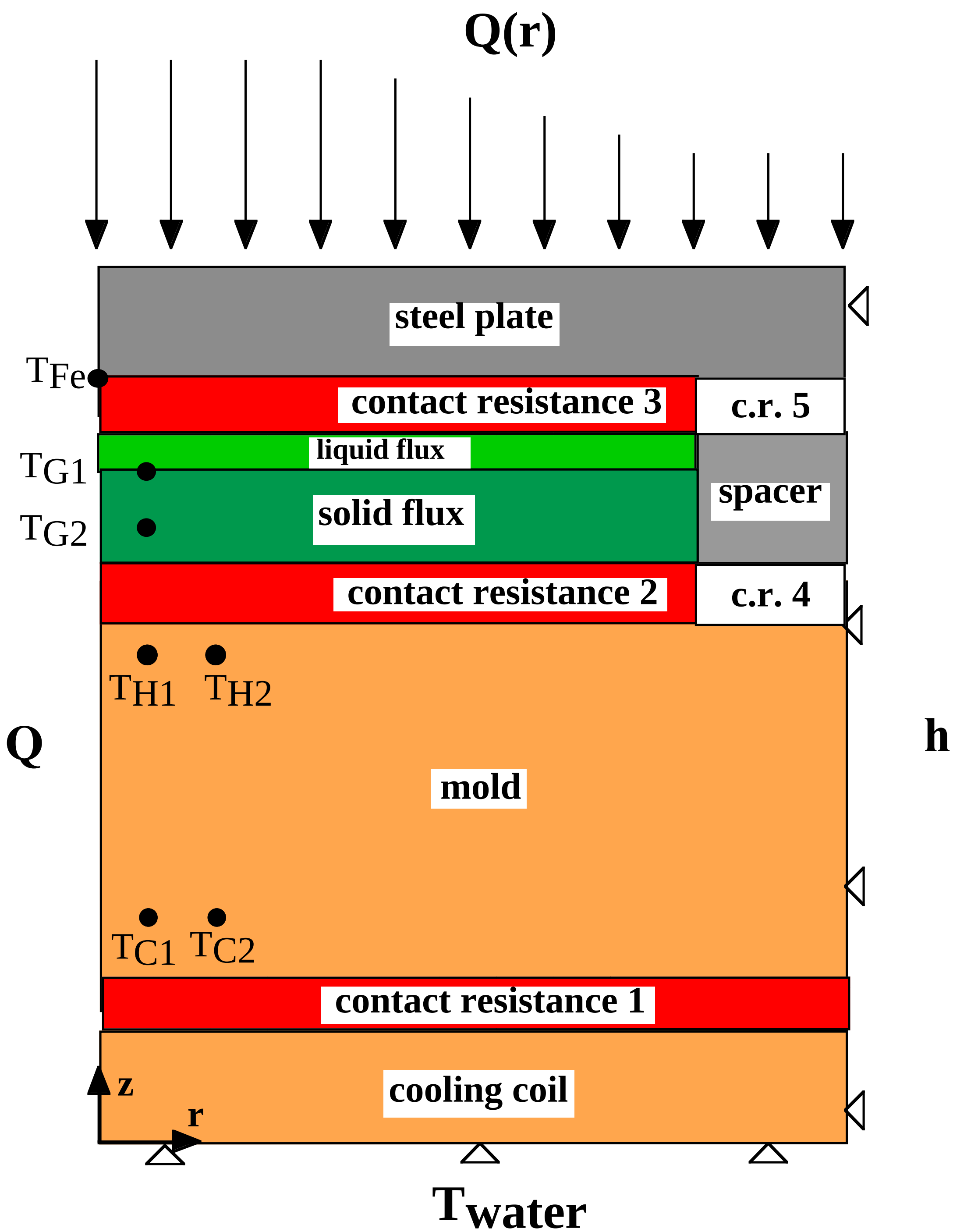

Figure 3.14: Schematic of ANSYS model domain

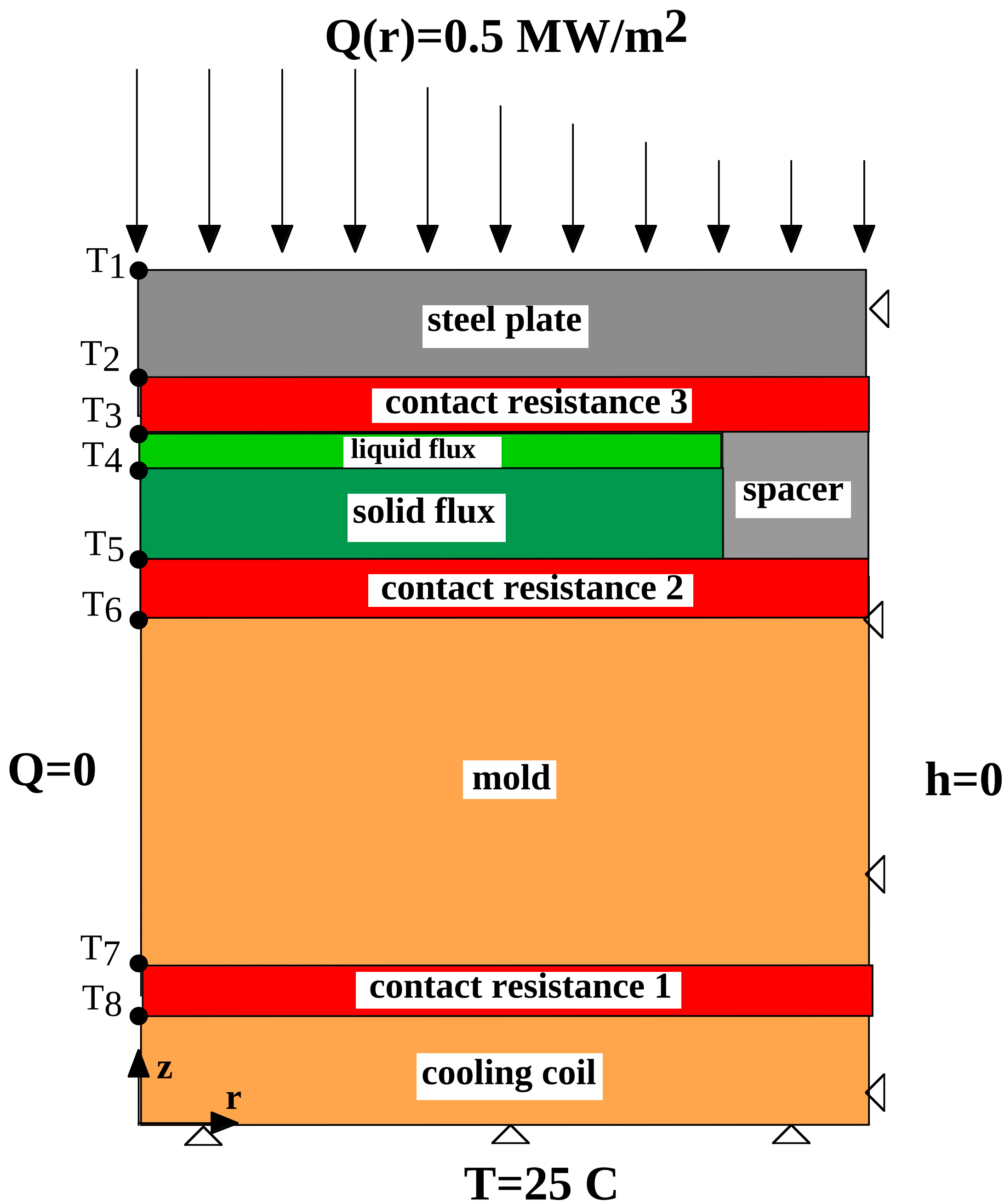

Figure 3.15: ANSYS model domain used for model verification

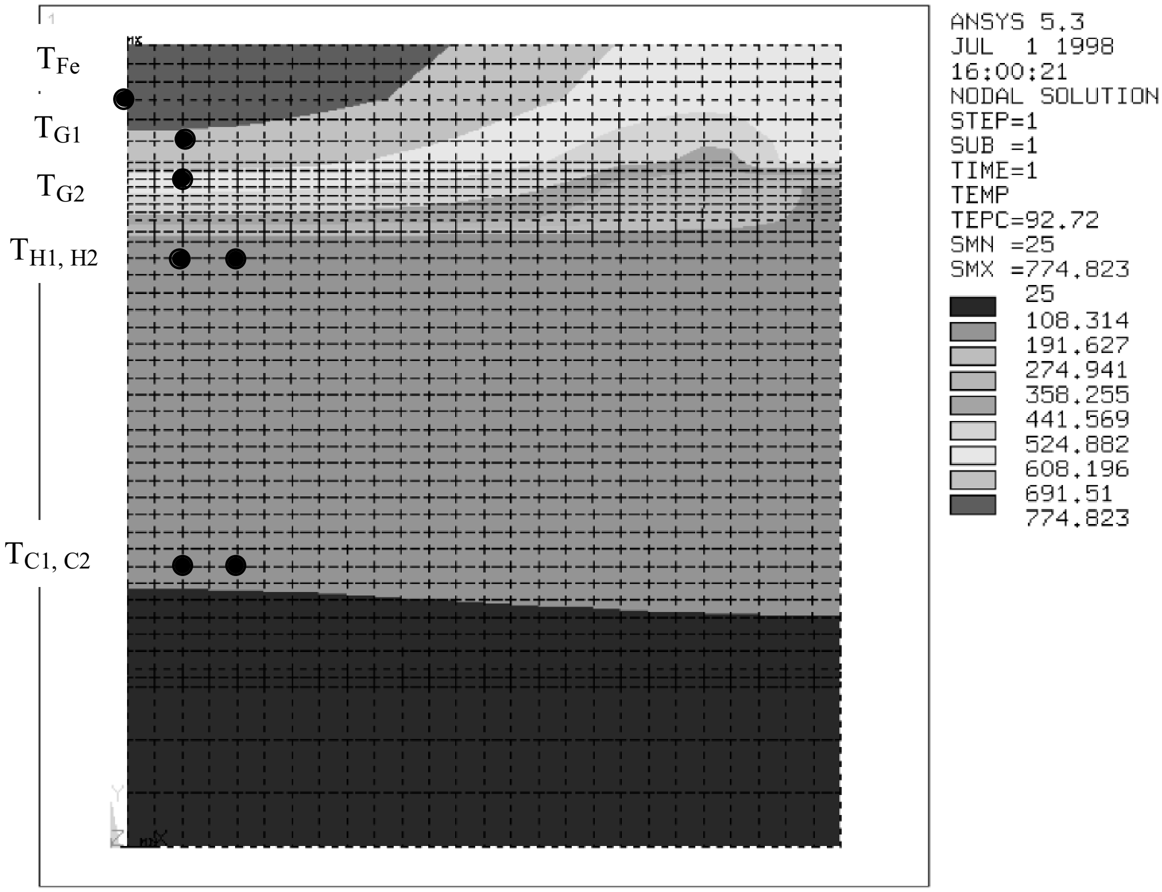

Figure 3.16: ANSYS Temperature Contour Plot for Test Case Four

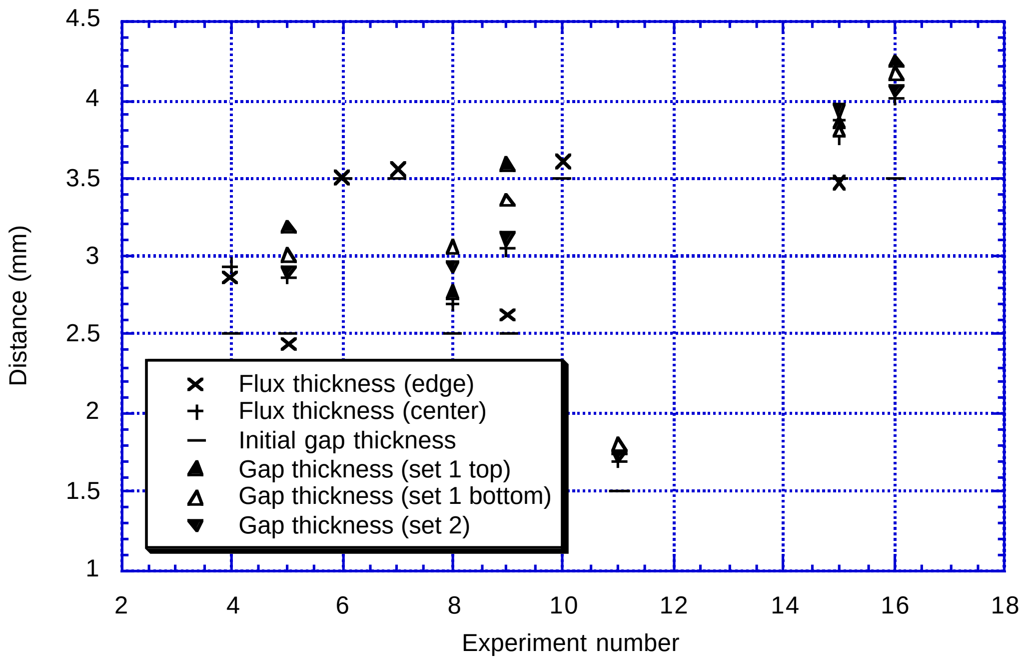

Figure 3.17: Comparison of initial and final gap thicknesses with measured flux layer thickness

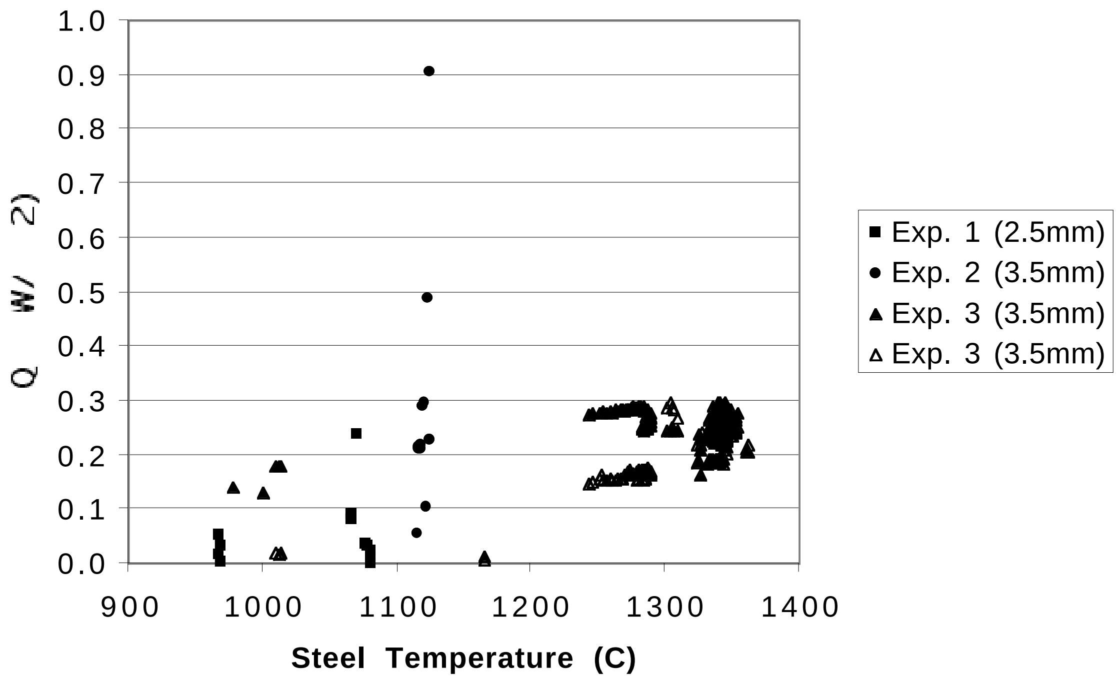

Figure 3.18: Heat Flux versus Steel Temperature for Flux A, derived from 1-D Model

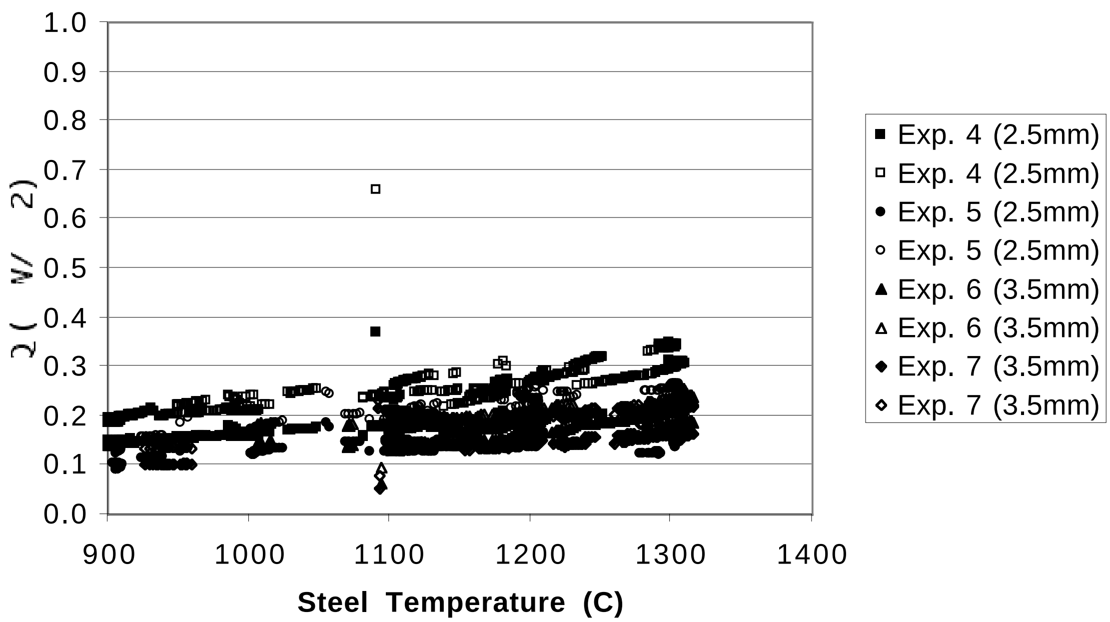

Figure 3.19: Heat Flux versus Steel Temperature for Flux B2, derived from 1-D Model

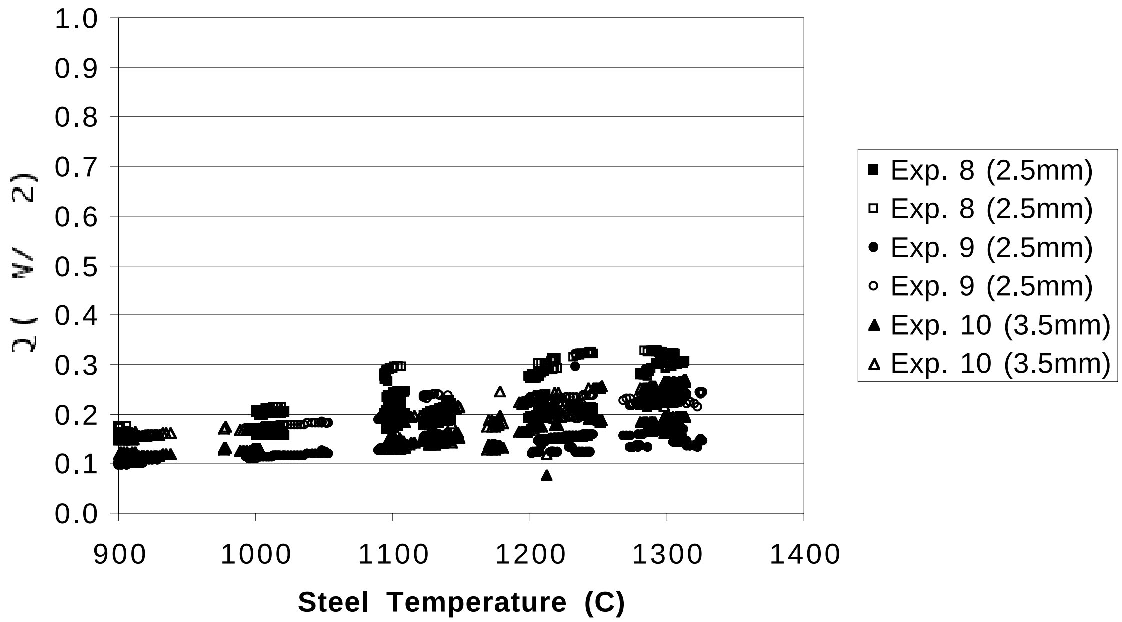

Figure 3.20: Heat Flux versus Steel Temperature for Flux C, derived from 1-D Model

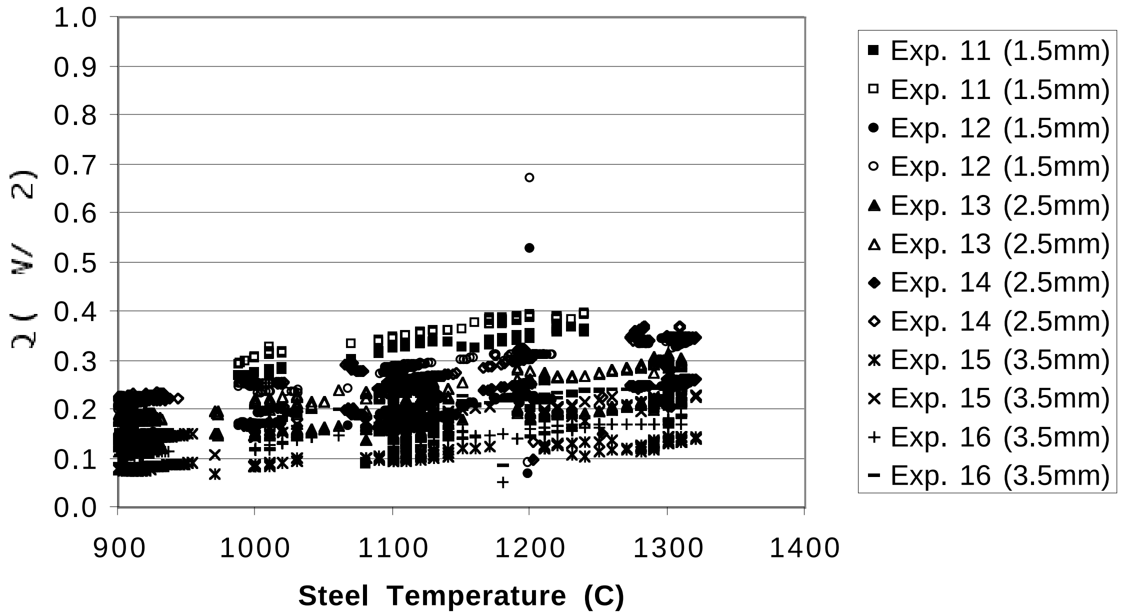

Figure 3.21: Heat Flux versus Steel Temperature for Flux D, derived from 1-D Model

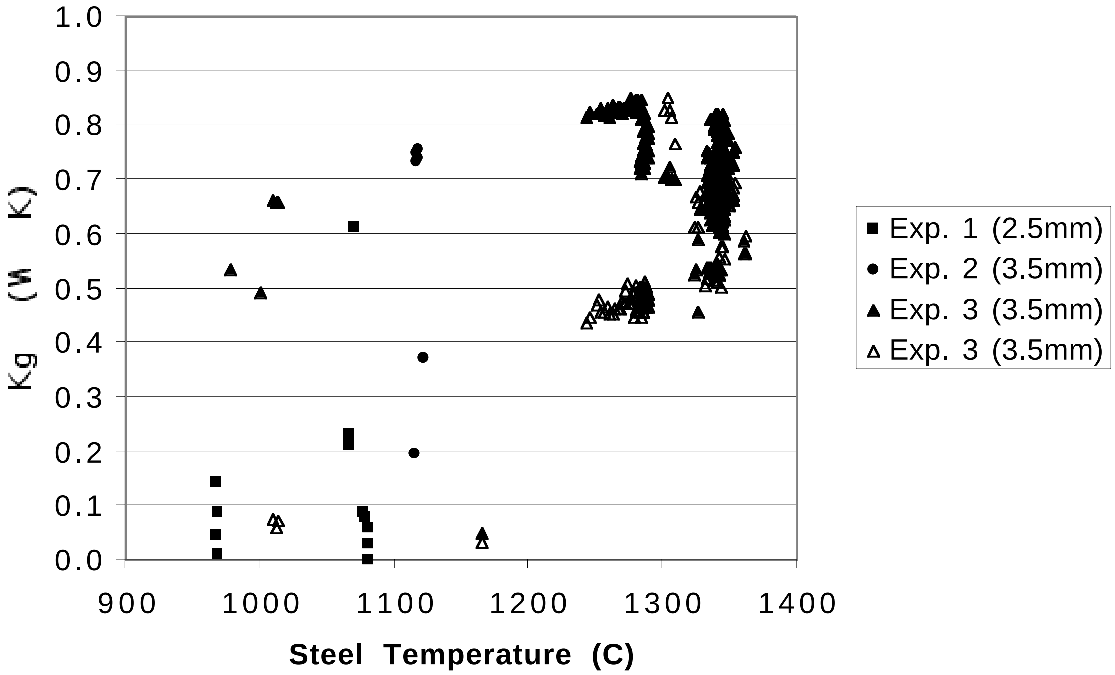

Figure 3.22: Gap Conductivity versus Steel Temperature for Flux A, derived from 1-D Model

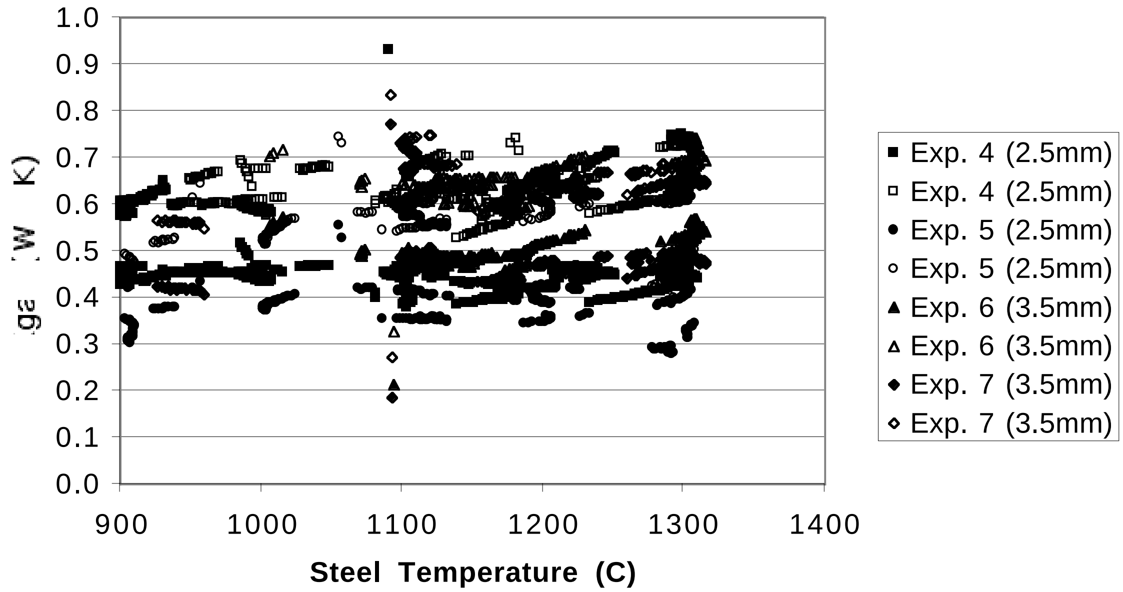

Figure 3.23: Gap Conductivity versus Steel Temperature for Flux B2, derived from 1-D Model

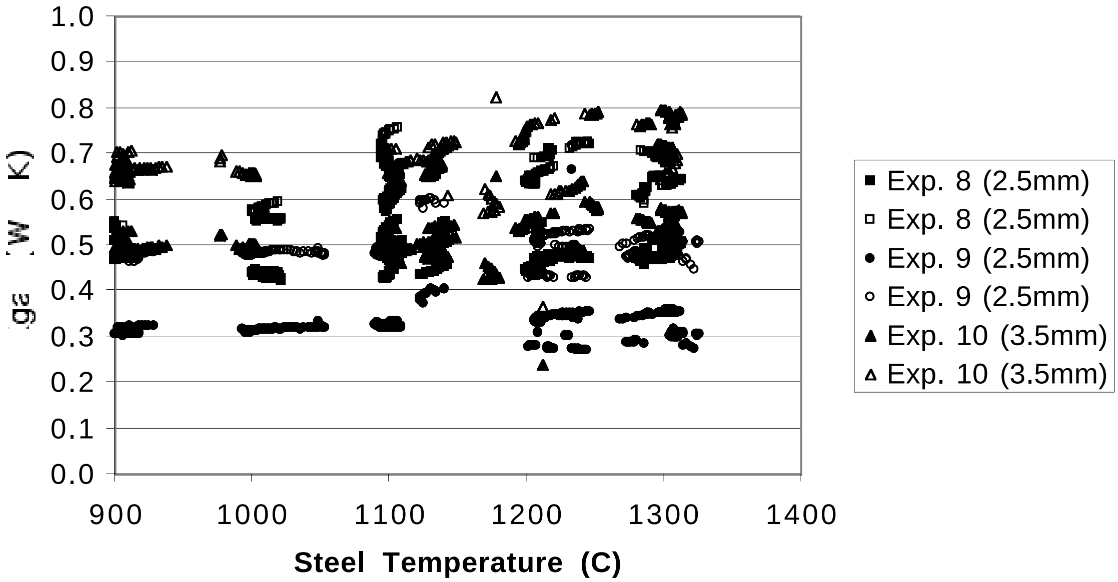

Figure 3.24: Gap Conductivity versus Steel Temperature for Flux C, derived from 1-D Model

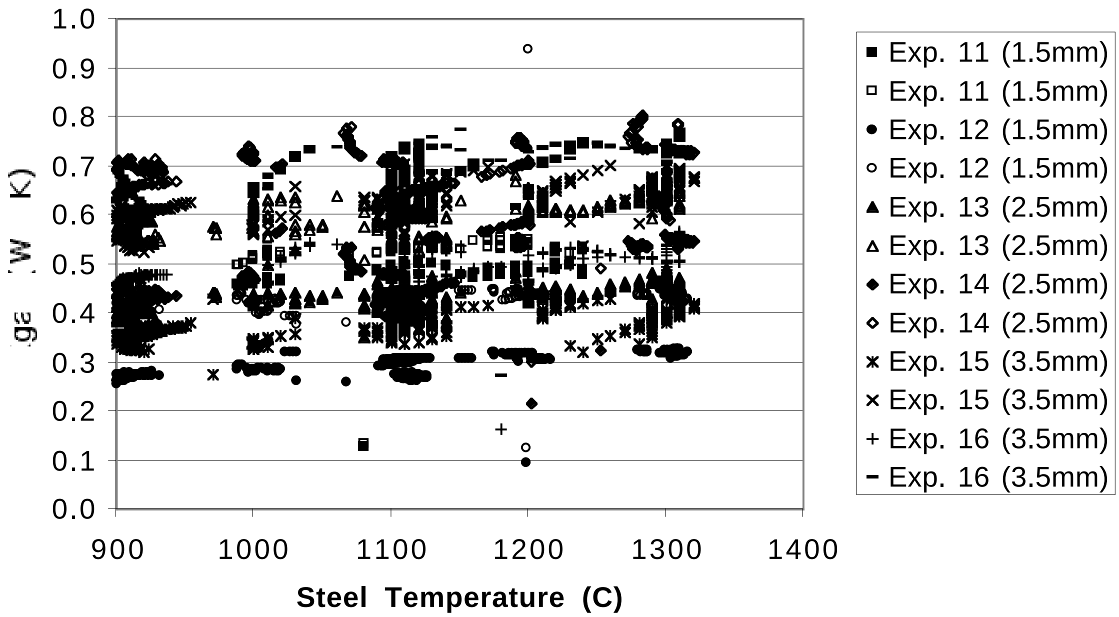

Figure 3.25: Gap Conductivity versus Steel Temperature for Flux D, derived from 1-D Model

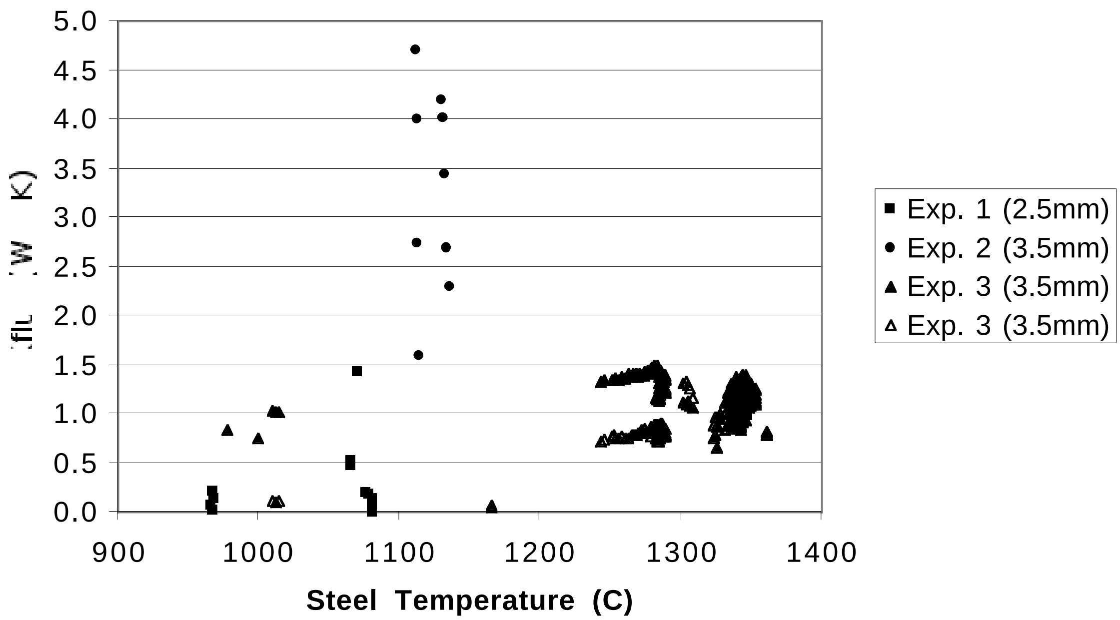

Figure 3.26: Flux Conductivity versus Steel Temperature for Flux A, derived from 1-D Model

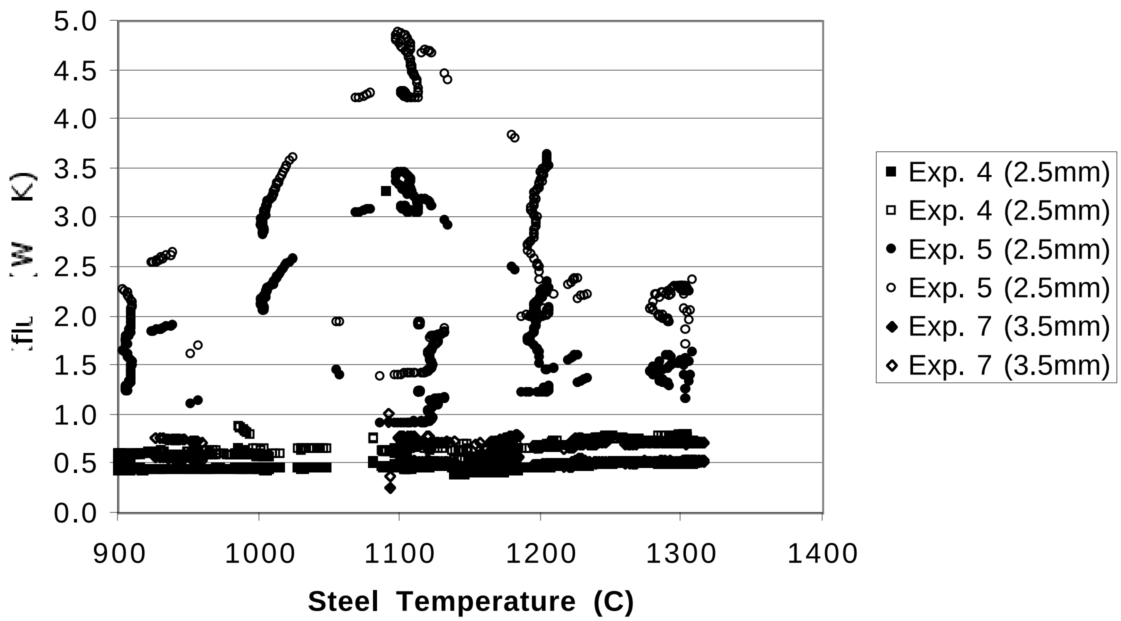

Figure 3.27: Flux Conductivity versus Steel Temperature for Flux B2, derived from 1-D Model

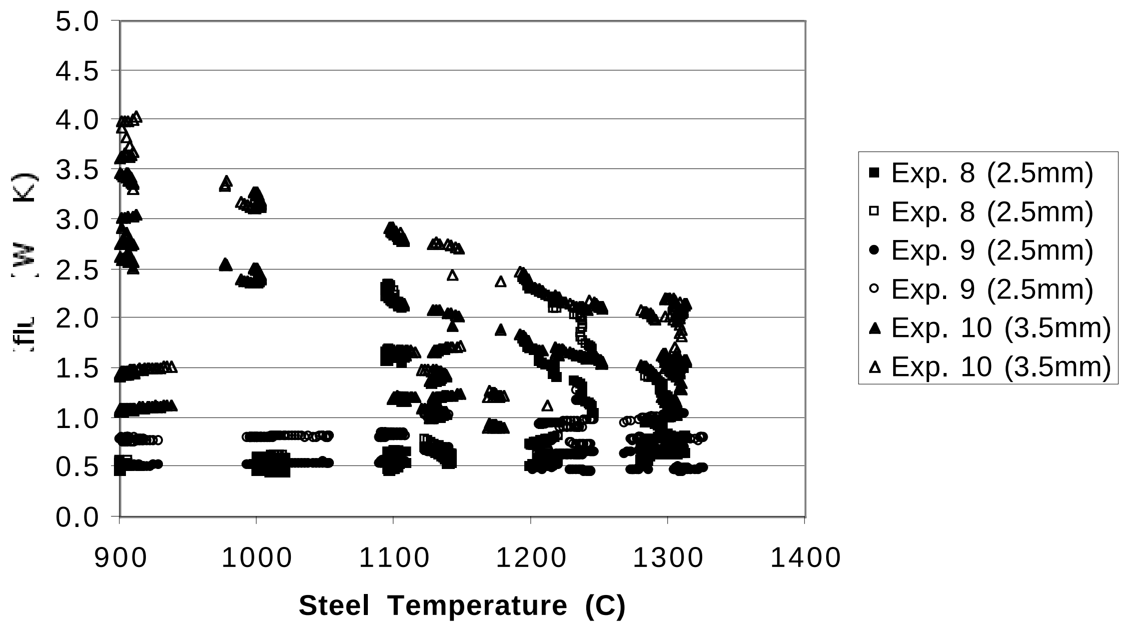

Figure 3.28: Flux Conductivity versus Steel Temperature for Flux C, derived from 1-D Model

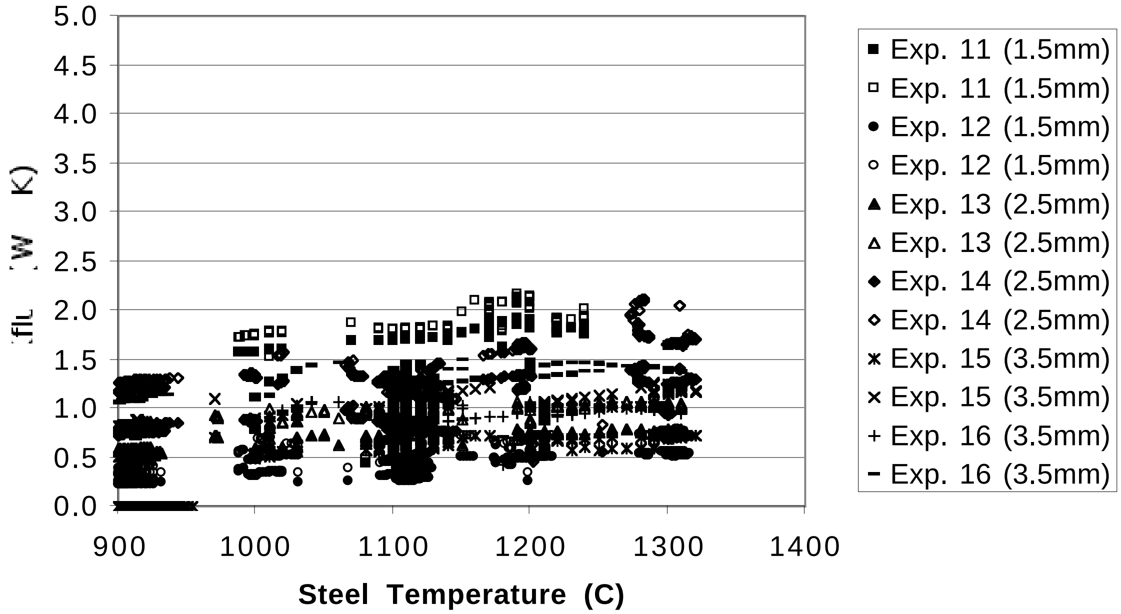

Figure 3.29: Flux Conductivity versus Steel Temperature for Flux D, derived from 1-D Model

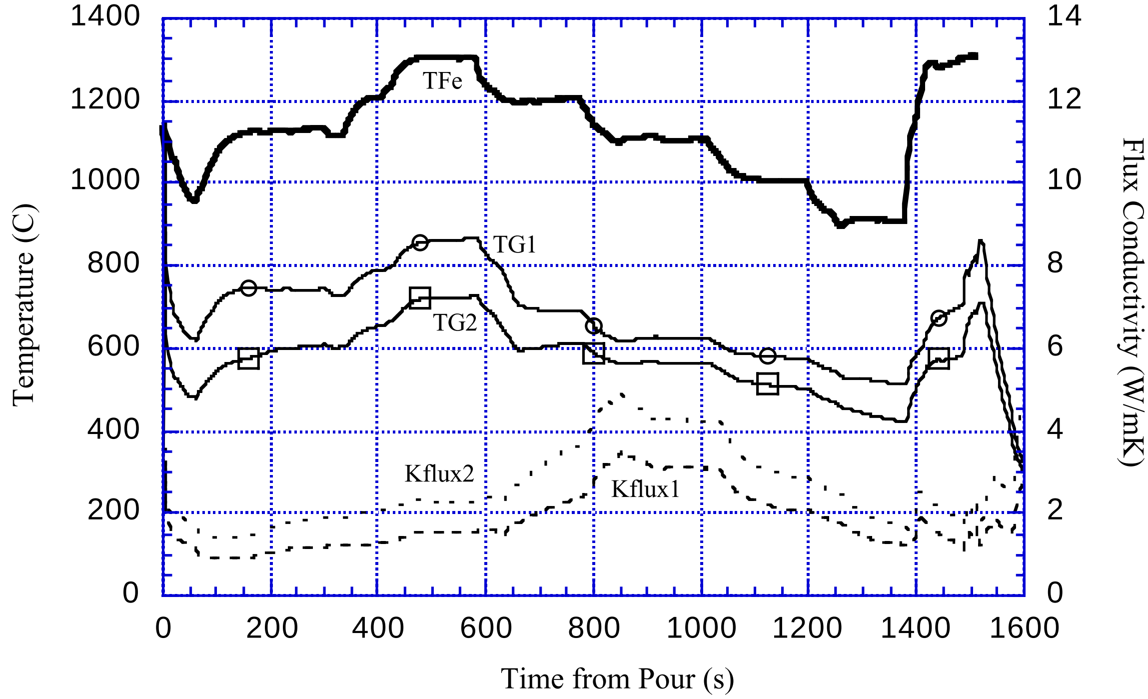

Figure 3.30: Plot of Steel Temperature, Gap Temperatures, and Calculated Flux Conductivities for Experiment 5

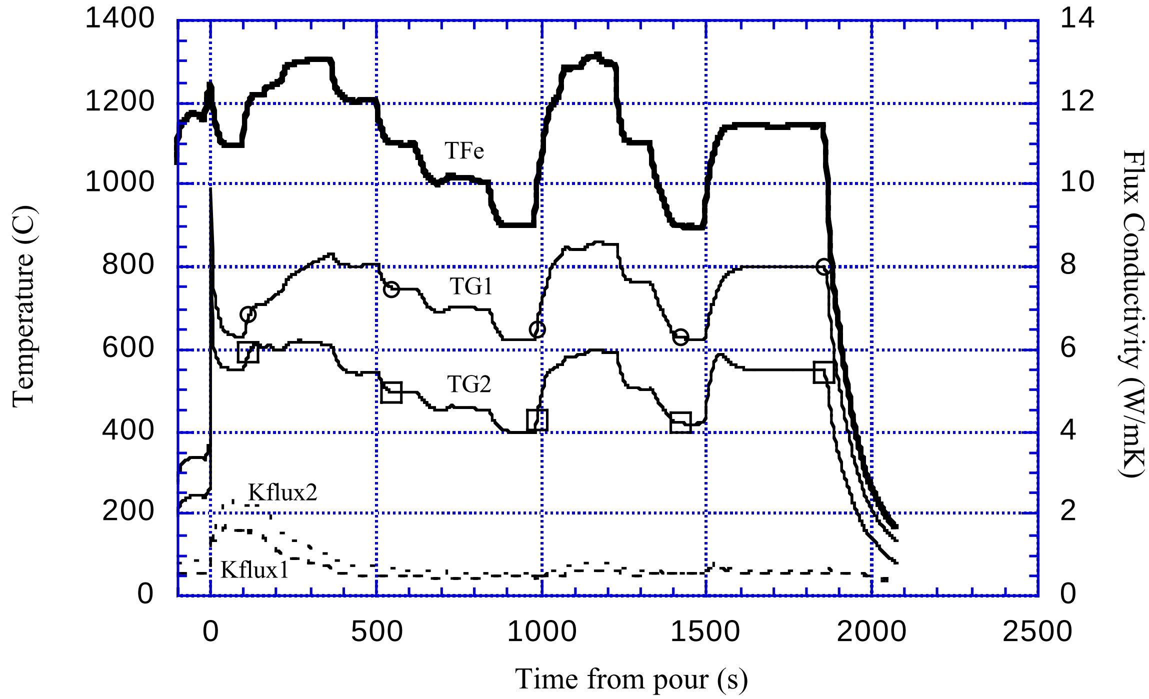

Figure 3.31: Plot of Steel Temperature, Gap Temperatures, and Calculated Flux Conductivities for Experiment 8

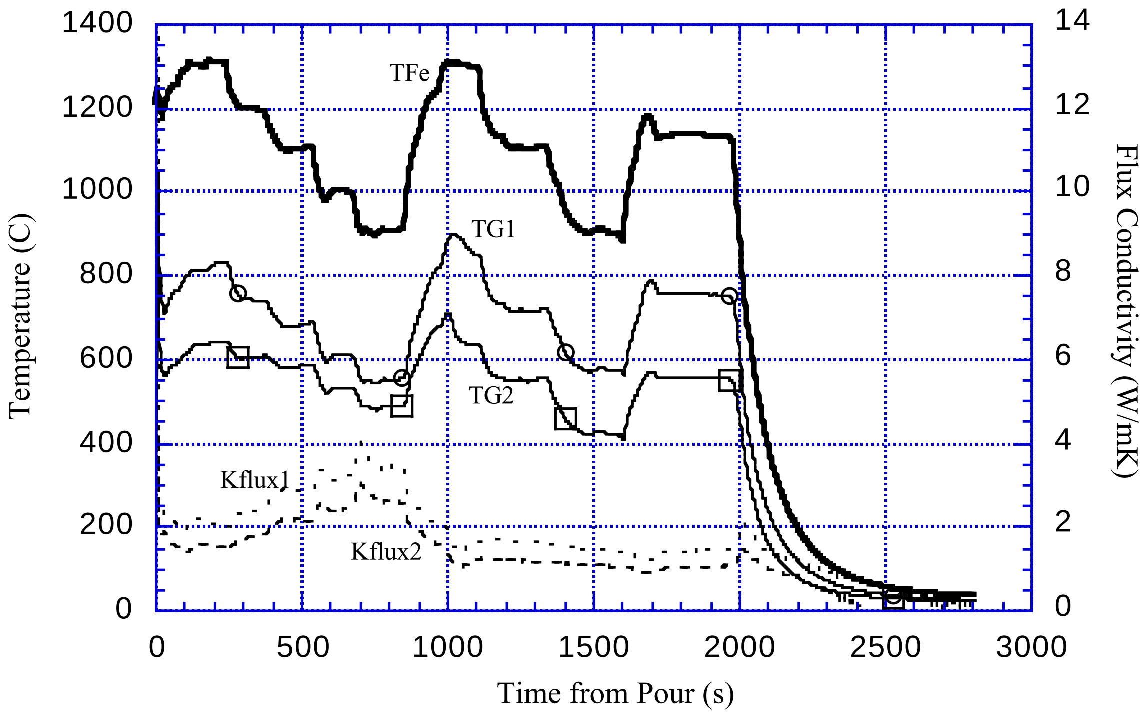

Figure 3.32: Plot of Steel Temperature, Gap Temperatures, and Calculated Flux Conductivities for Experiment 10

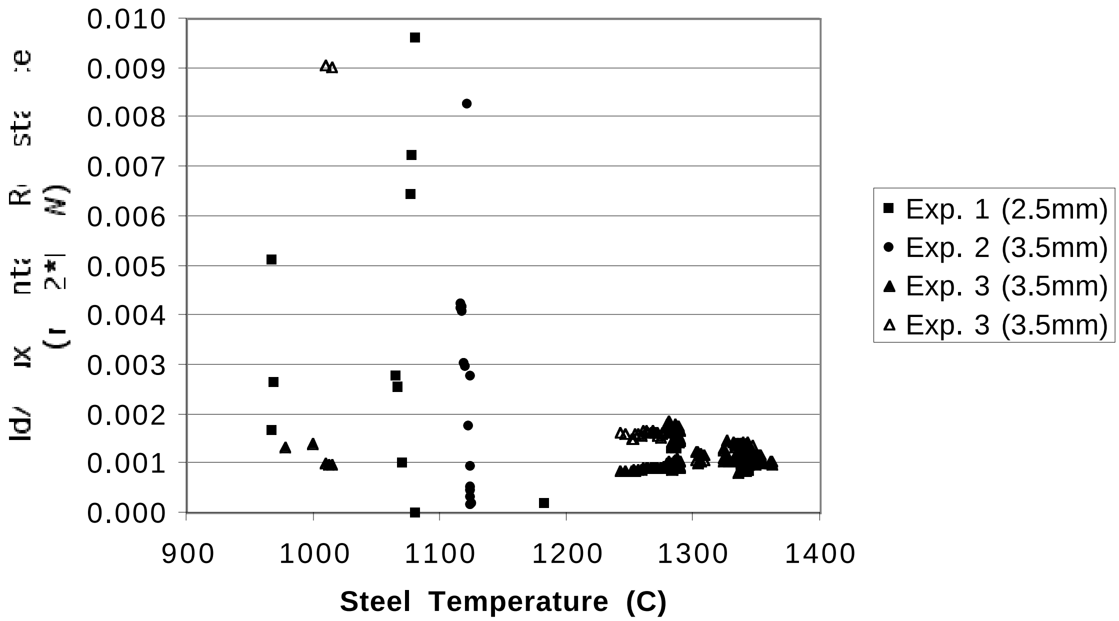

Figure 3.33: Mold/Flux Contact Resistance versus Steel Temperature for Flux A, derived from 1-D Model

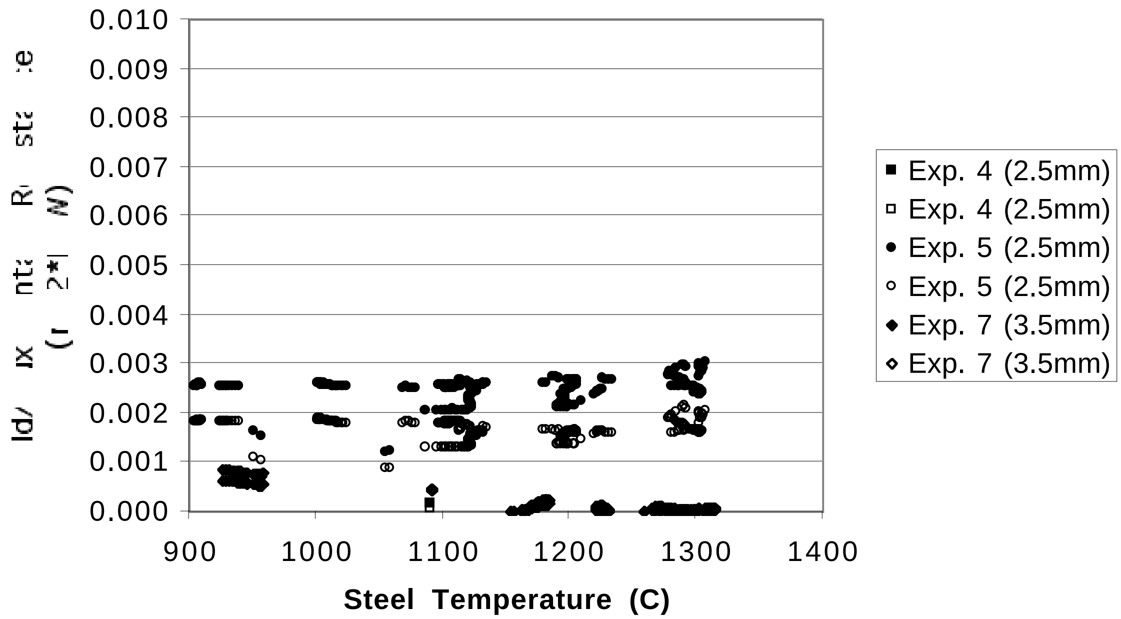

Figure 3.34: Mold/Flux Contact Resistance versus Steel Temperature for Flux B2, derived from 1-D Model

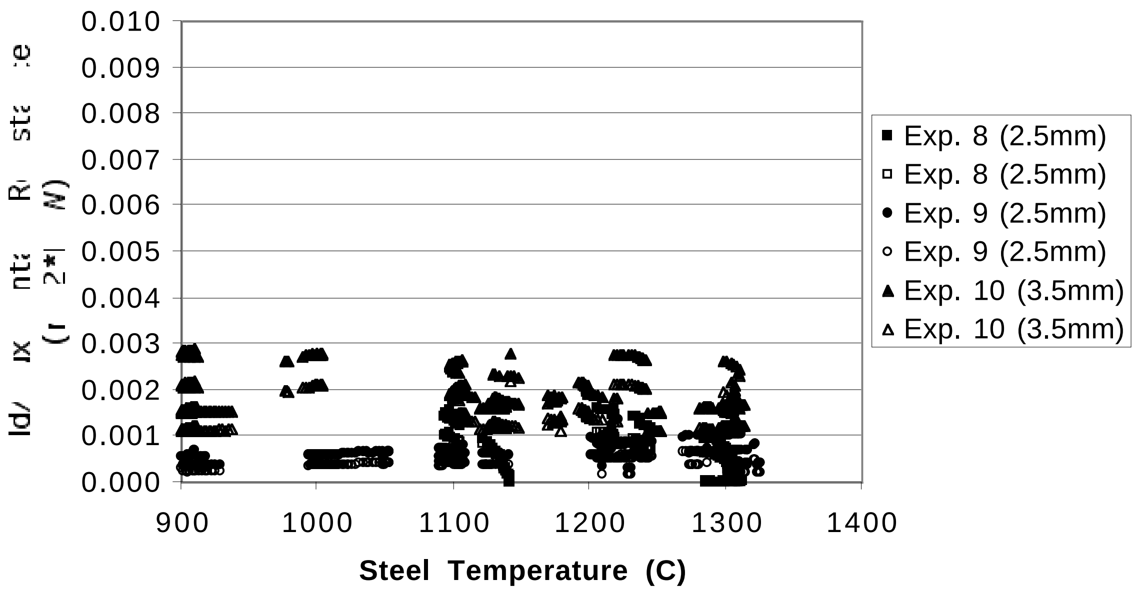

Figure 3.35: Mold/Flux Contact Resistance versus Steel Temperature for Flux C, derived from 1-D Model

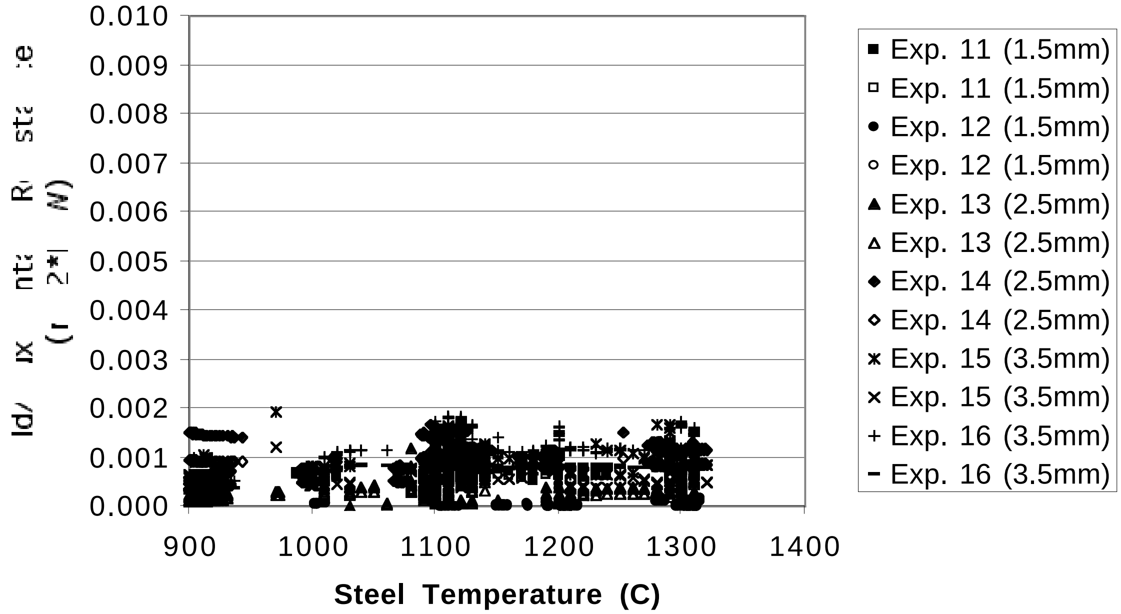

Figure 3.36: Mold/Flux Contact Resistance versus Steel Temperature for Flux D, derived from 1-D Model

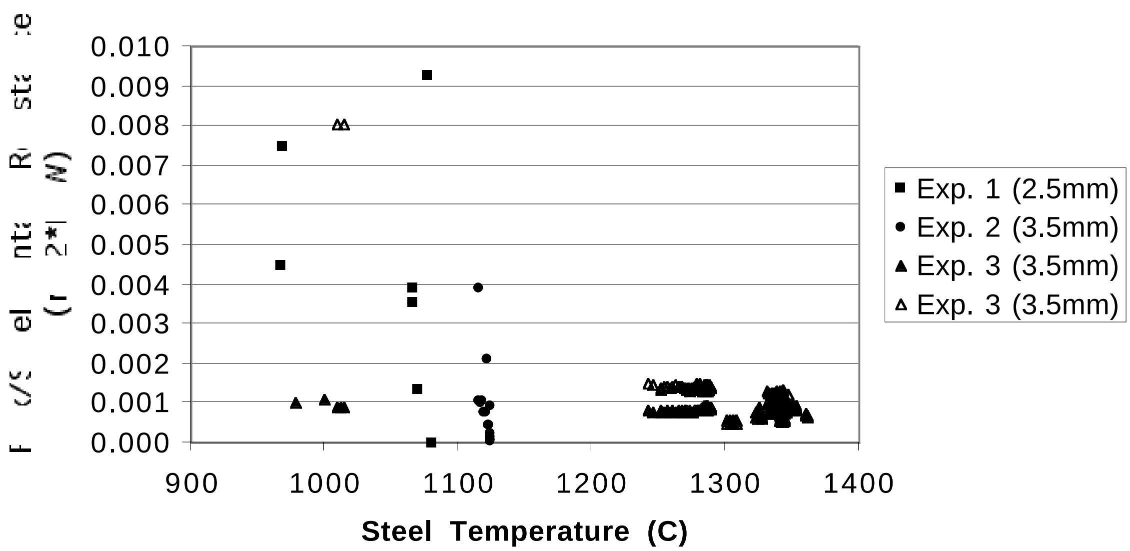

Figure 3.37: Flux/Steel Contact Resistance versus Steel Temperature for Flux A, derived from 1-D Model

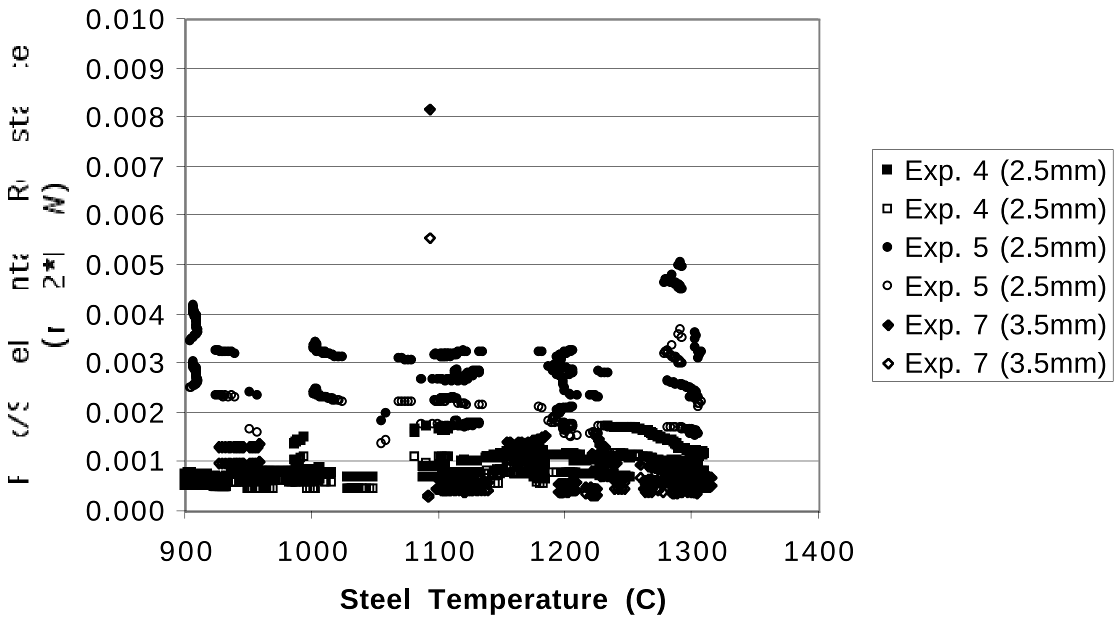

Figure 3.38: Flux/Steel Contact Resistance versus Steel Temperature for Flux B2, derived from 1-D Model

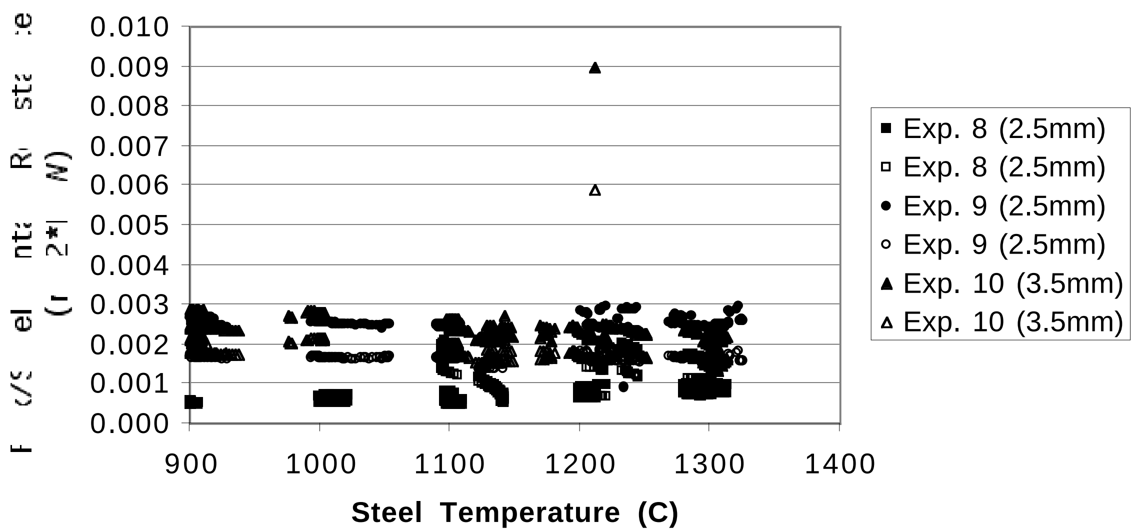

Figure 3.39: Flux/Steel Contact Resistance versus Steel Temperature for Flux C, derived from 1-D Model

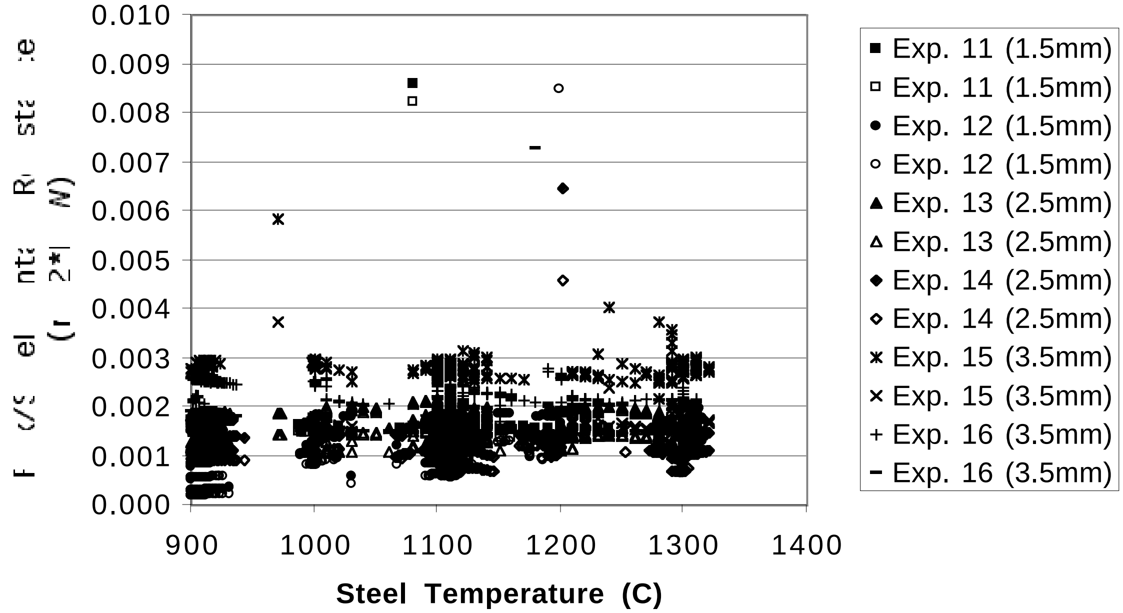

Figure 3.40: Flux/Steel Contact Resistance versus Steel Temperature for Flux D, derived from 1-D Model

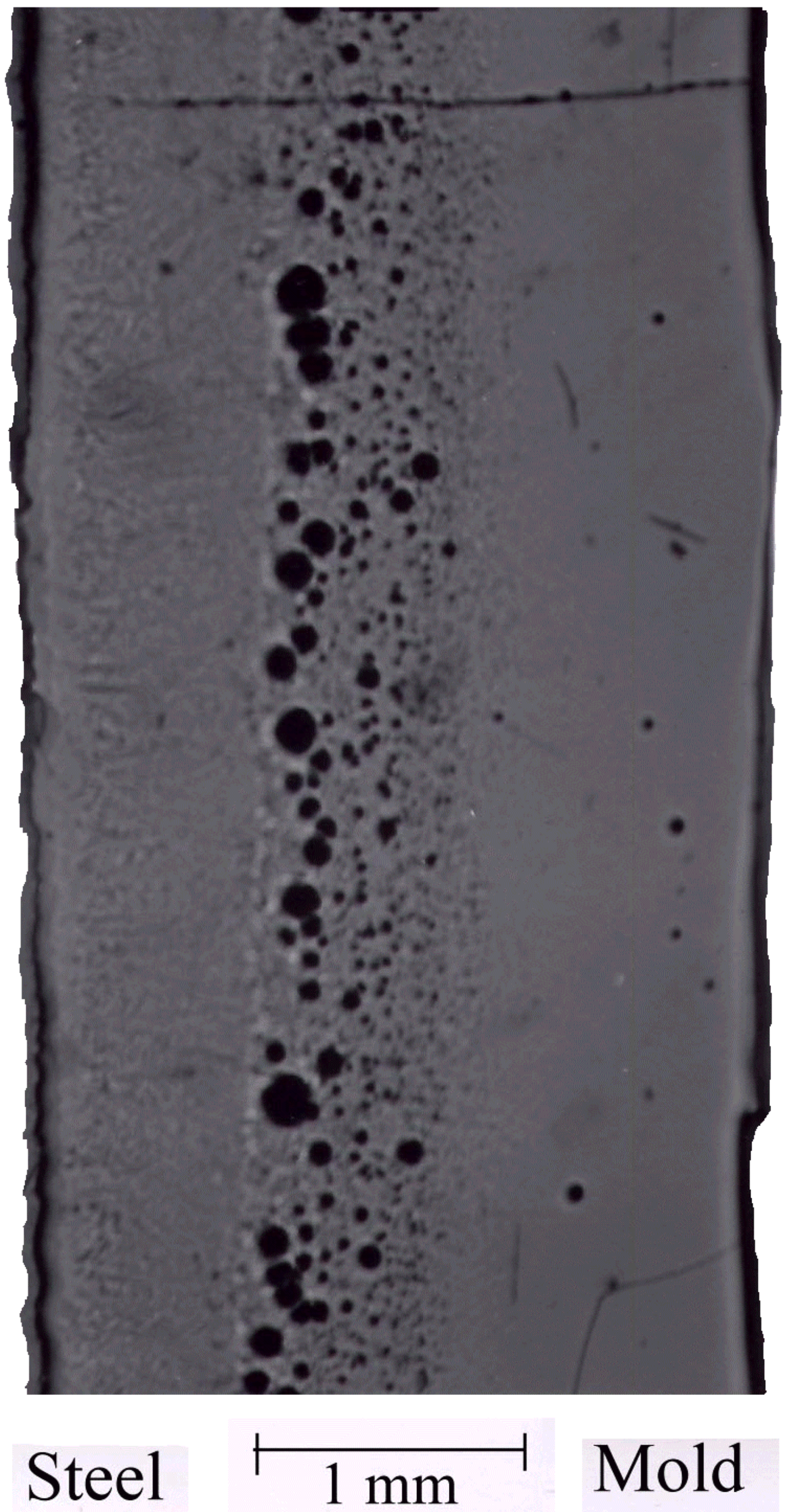

Figure 3.41: Microstructure of section of solidified mold flux C (Experiment 8 near edge)

Figure 3.42: Microstructure of section of solidified mold flux D (Experiment 15 near thermocouple

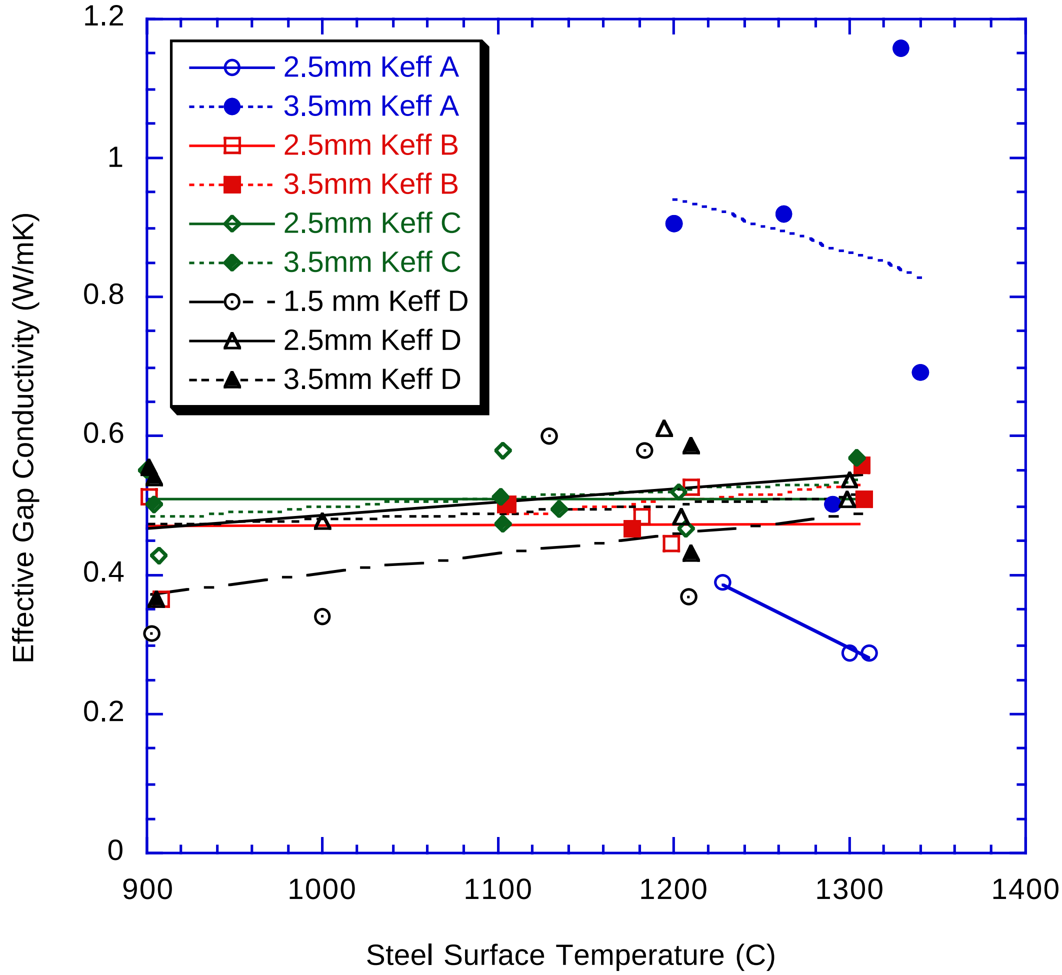

Figure 3.43: Effective gap conductivity results from 1-D Steady State Model

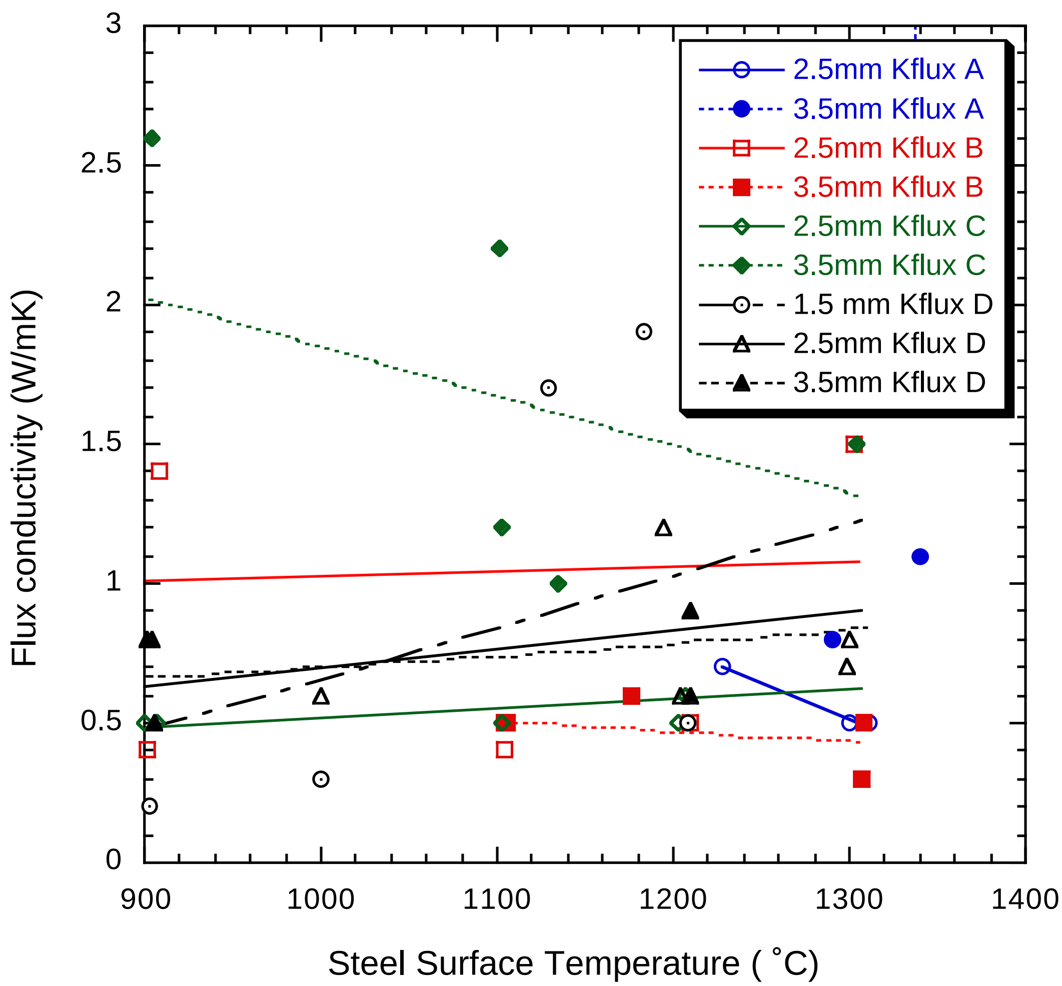

Figure 3.44: Flux conductivity results from 1-D Steady State Model

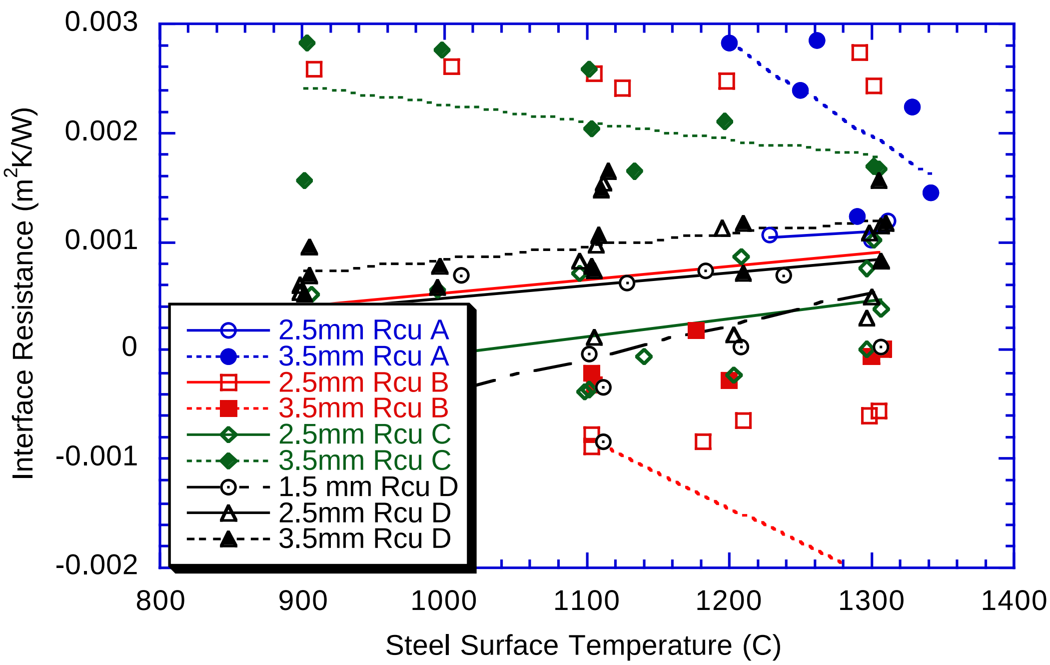

Figure 3.45: Flux/Mold Contact Resistance results from 1-D Steady State Model

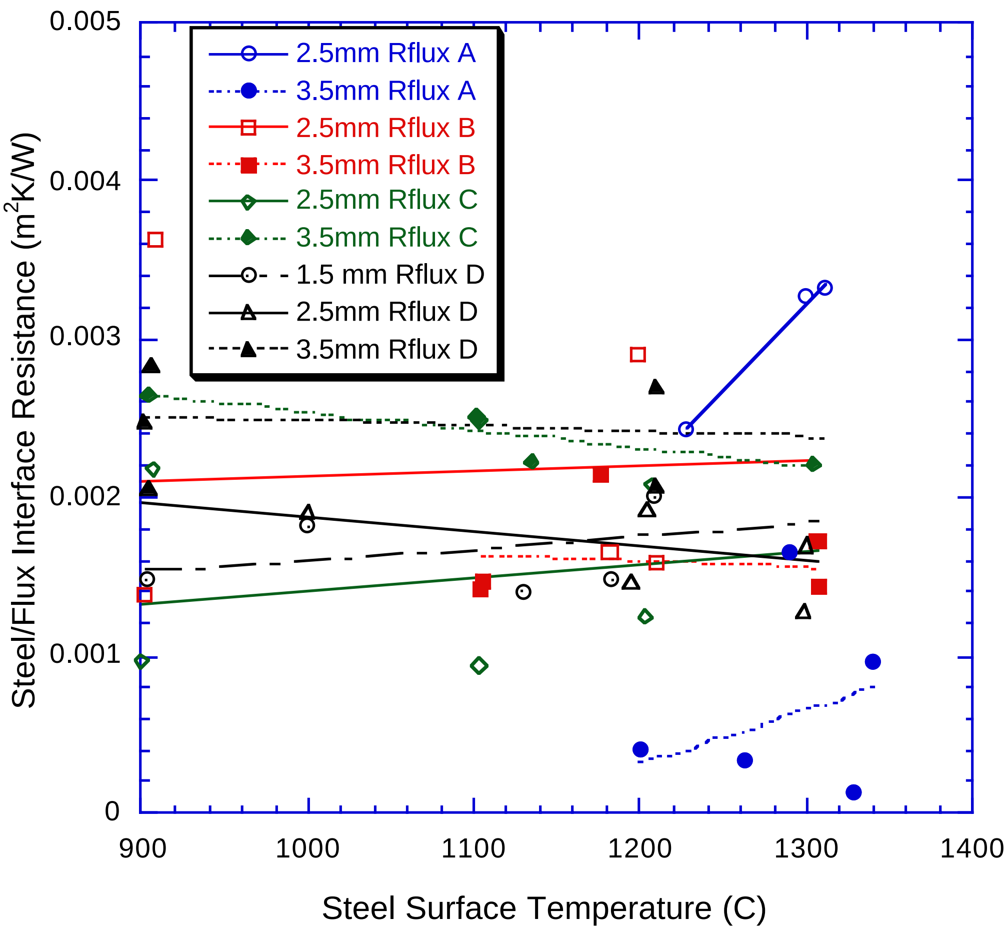

Figure 3.46: Flux/Steel Contact Resistance results from 1-D Steady State Model

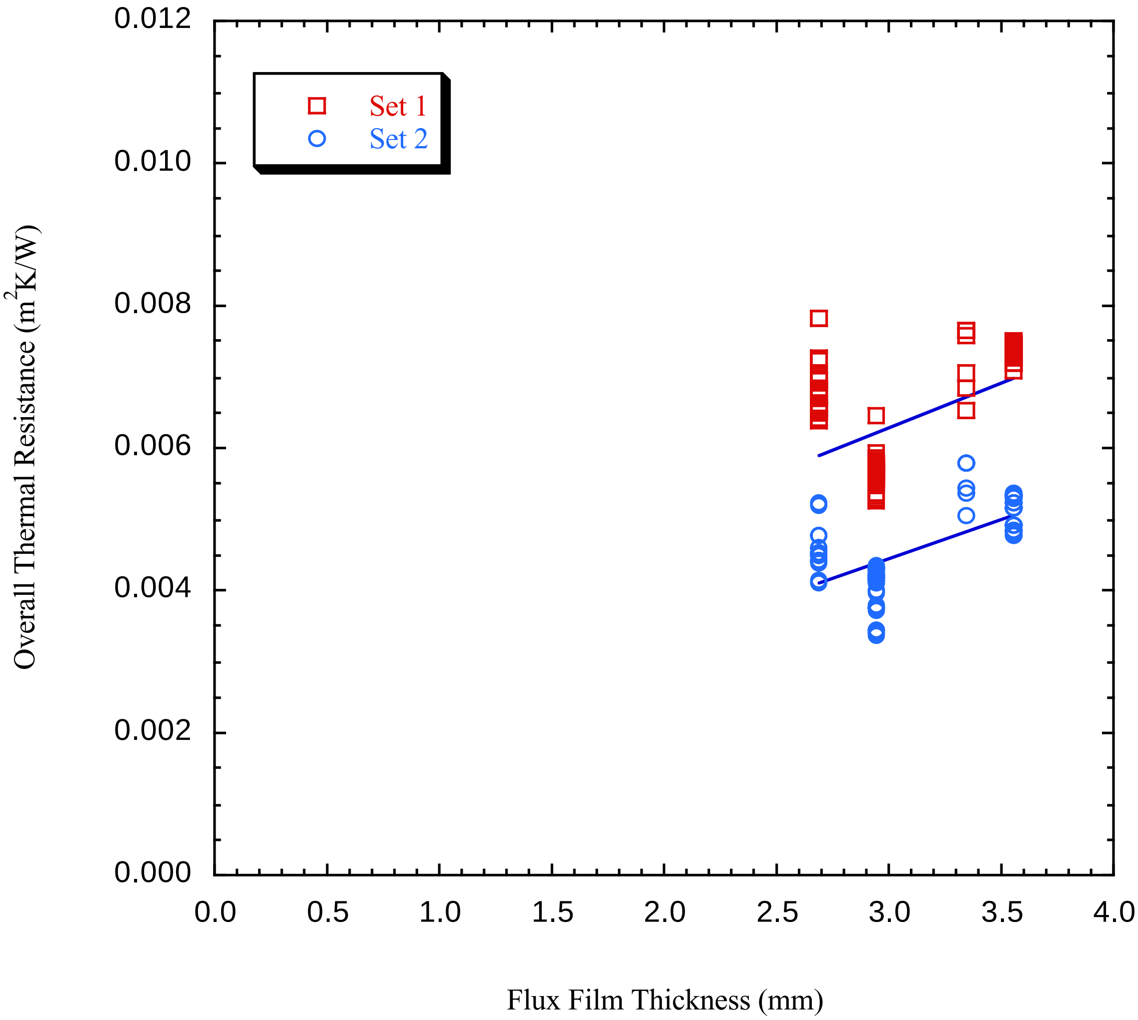

Figure 3.47: Overall Thermal Resistance versus Flux Film Thickness for Flux B2

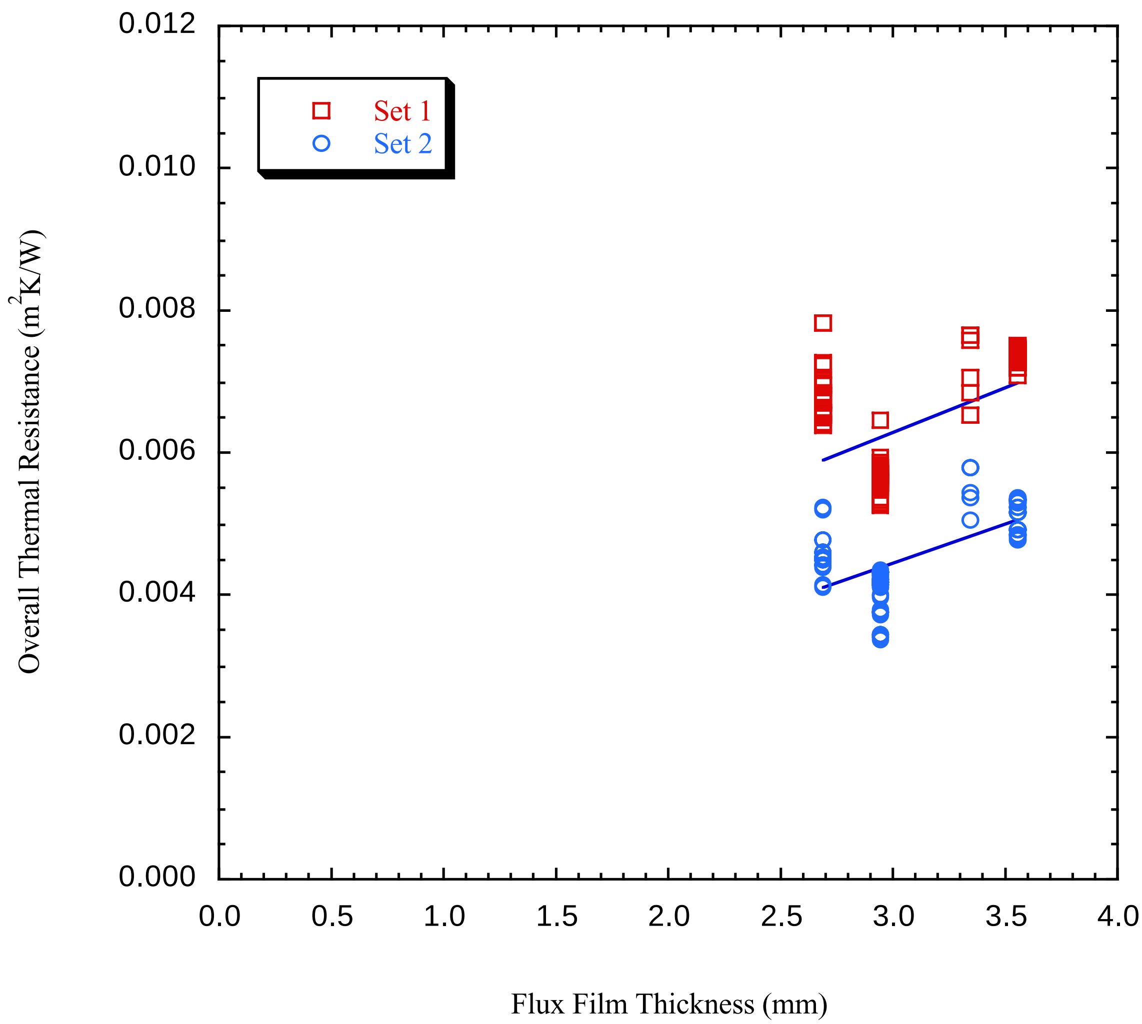

Figure 3.48: Overall Thermal Resistance versus Flux Film Thickness for Flux C

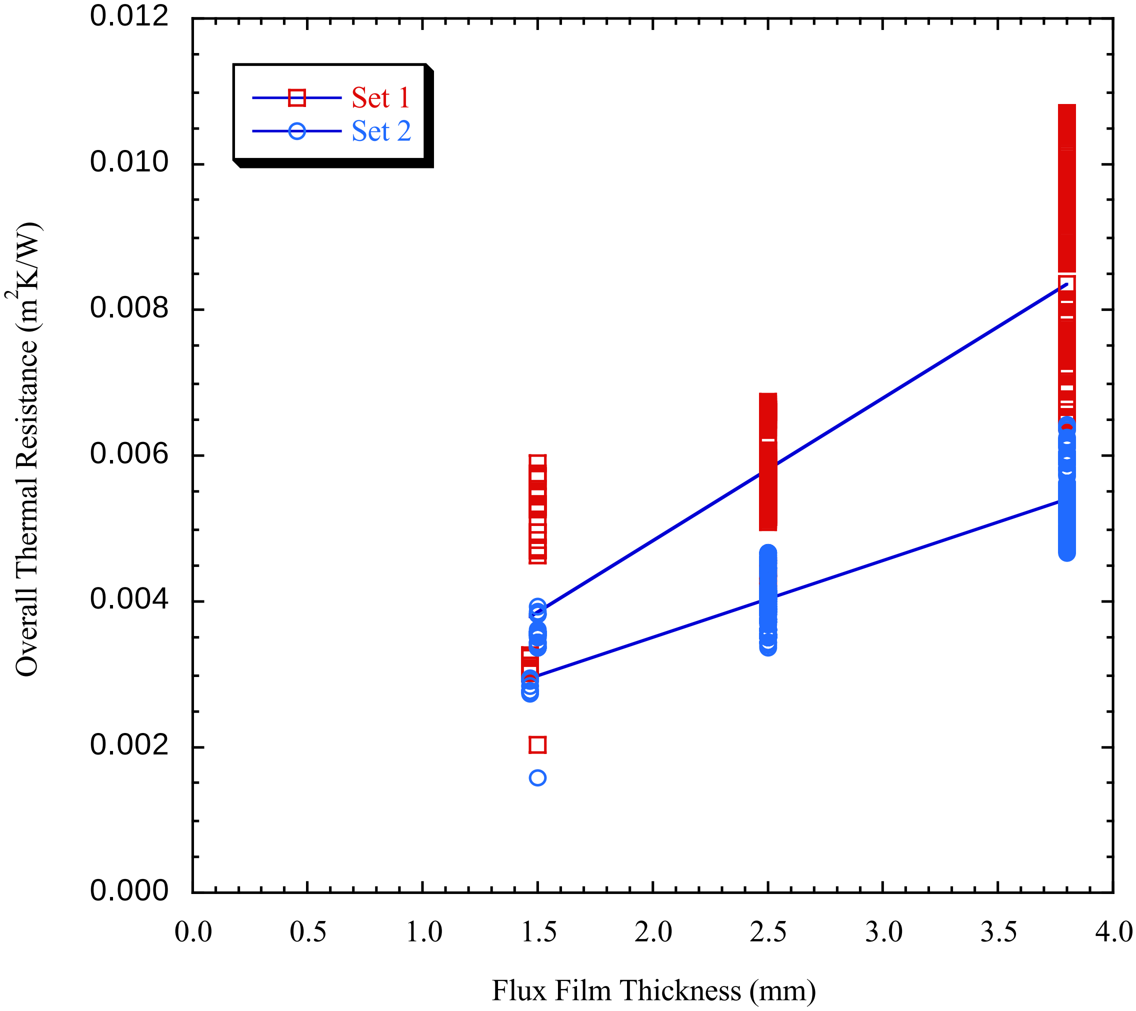

Figure 3.49: Overall Thermal Resistance versus Flux Film Thickness for Flux D

4 BREAKOUT SHELL ANALYSIS

The previous two sections have described the mathematical models developed to simulate the heat transfer mechanisms across the interface between the water-cooled copper mold and the solidifying steel shell. Also, experiments to measure the thermal characteristics of the mold powders used in continuous casters have been analyzed to obtain values for gap conductivity, flux conductivity, and radiation heat transfer coefficient which are used as boundary conditions to the mathematical model. This section summarizes the documentation and analysis [29] of a breakout event at the Armco, Inc. stainless-steel thin-slab caster in Mansfield, OH. This analysis was conducted to quantify shell growth, heat transfer, and microstructure of a breakout event that occurred on March 25, 1997. In addition to providing the relevant mold geometry and casting conditions, the analysis investigates mold temperatures and cooling water temperature increases measured under similar conditions. The data from this analysis, along with values obtained from the mold powder experiments, was applied to the CON1D mathematical model to predict transient shell growth during the breakout event. This work is believed to be the first documented effort of its kind, compiling detailed measurements and descriptions of a breakout event in a continuous casting process.

4.1 Documentation of Breakout Event and Conditions

The following sections describe the conditions under which the breakout shell was formed. Information is divided into sections describing how the breakout occurred, details of the mold and submerged entry nozzle (SEN), steel chemistry, mold powder properties and practice, and casting conditions.

4.1.1 Description of Breakout Event

The breakout occurred while casting a 132 x 984 mm(5.2 x 38.75) slab of 434 stainless steel. A picture of the breakout shell is shown in Figure 4.1. The breakout was caused by the opening of part of a long longitudinal crack. A picture of the crack opening in the shell is shown in Figure 4.2. The hole itself is wedge-shaped, measuring 483 mm long and tapers to a maximum opening of 19 mm at the bottom. The hole extends from 965 to 1448 mm below the top of the shell and is 75 mm west of the centerline down the inside radius wide face. The hole tapers into a longitudinal crack extending both upwards to within 300 mm of the meniscus, and downwards many meters below the breakout.

4.1.2 Description of Water-Cooled Copper Mold

The water-cooled copper mold, which is used to form a steel shell thick enough to contain the liquid steel within the strand, is comprised of four straight C181 Cr-Zn-Cu alloy plates that are supported by a steel cassette water box which flows water through the grooves in the copper plates. Figure 4.3 shows how the mold plates and steel cassette form the continuous casting mold.

Figures 4.4 through 4.6 show the configurations of the wideface and narrowface copper plates, as well as how the copper plates are attached to the water box. Table 4.1 gives further details of the mold geometry. Copper plate thicknesses represent that of new mold plates, whereas the mold used during the breakout event were machined back to 24 mm. Both the wideface and narrowface plate surfaces are coated with a uniform 0.1 mm thick layer of Chromium over a layer of Nickel tapered from 1 mm thick at mold top to 1.5 mm thick at mold bottom. The figures showing the mold plate configurations do not reflect any of these mold coatings.

One of the copper molds at the Mansfield facility is instrumented with thermocouples to measure mold heat fluxes, which is described in more detail later in this section. Figures 4.5 and 4.6 show how these thermocouples are located in the wideface and narrowface plates.

4.1.3 Description of Submerged Entry Nozzle

The submerged entry nozzle is a 3-port design with two large ports pointing towards the narrow faces and a small central port pointing downwards. The nozzle bore is 135 mm O.D. and 70 mm I.D. It tapers into a rectangular outlet region measuring 76 x 185 mm O.D. with 32 x 150 mm I.D. The nozzle is submerged about 130 mm below the steel / flux interface, measuring to the top of the large port. Further details on the nozzle and flow pattern are reported elsewhere [13].

4.1.4 Process Parameter Details

There are several process parameters that must be measured in order to model breakout shell growth. A few of these include casting speed, slab geometry, steel composition, SEN position, cooling water flow rates and direction, oscillation practice, and mold powder composition. Table 4.2 lists values for several of these process parameters, casting geometry, and steel composition for the breakout event. Figure 4.7 shows measurements of casting speed, average liquid level, and stopper rod position versus time for the breakout event. Mold liquid level is determined by triangulating the signal from a radioactive source which is cut off at the average level of the molten steel. The liquid level recorded is relative to a horizontal line 260 mm below the top of the mold. The stopper rod opening position is measured on a percent linear distance basis relative to an arbitrary initial reference point above the tundish well. Increasing the opening from 27% to 55% represents a roughly 3-fold increase in opening area and flow, from a steady value that is heavily throttled (mainly closed).

Before the breakout occurs, the casting speed, liquid level, and stopper rod parameters in Figure 4.7 behave in a controlled manner. The breakout event starts at 7178 seconds. At this time, the stopper rod position increases dramatically as it attempts to stabilize the falling liquid level. The operator closed the stopper rod at 7190 seconds, and the casting speed began to decrease in a linear manner. The liquid level quickly dropped after the stopper rod was completely closed, and fell beyond the range of the sensor. Casting was stopped completely at 7210 seconds.

Table 4.1 contains the mold cooling water flowrates and velocities based on the new mold s slot geometry. The mold cooling water flowed from the bottom to the top of the mold. Temperatures of the mold cooling water were measured before and during the breakout event. Mold water temperature differences are shown in Figure 4.8, and have been corrected for sensor bias by subtracting the sensor readings recorded before the steel enters the mold. The water inlet temperature remained fairly steady at about 35 ßC during the breakout event. The outlet temperature was about 8 ßC higher. Bias for the mold water temperature measurements before the breakout tundish run are: 1.14 °C (IR), 1.03 °C (OR), -0.20 °C (West NF), and -0.27 °C (East NF).

The mold oscillation practice includes a stroke of 5.13 mm at a frequency of 3.942 Hz, with 0.1 s negative strip time. Average oscillation mark depth and width were 0.4 +/-0.2 x 1.0 +/-0.5 mm, with a measured pitch of 7.1 +/-1 mm. The oscillation marks were generally well formed and horizontal, including near the breakout, indicating that lubrication conditions appeared to be normal. An anomalous surface feature is that the oscillation marks below the mold along the narrowface slant downwards toward the outside radius, as shown in Fig. 4.9. In addition, the narrow faces bulge outward about 30 mm each on the inside radius edges.

Table 4.3 lists composition and properties of the mold powders used in the breakout event. The breakout was initiated 48 minutes after changing from powder, A, to an exothermic powder, B, and 41 minutes after changing heats. Powder C is used to compare steady-state mold temperatures, collected during a similar casting run which didn t have a breakout, against the breakout event to estimate mold heat flux values. These powder classifications are the same used to identify mold powders tested in the previous chapter. Powder B and B2 are powders from different suppliers that have similar compositions. The thermal properties for powder B2 will be used in the CON1D shell growth predictions effort described later in this section.

4.2 Breakout Shell Thickness Measurements

The breakout shell was divided into 14 sections, to measure the shell thickness as a function of position from the shell meniscus. The narrowfaces were cut down their centerline, while the broadfaces were cut at 86mm, 238mm, and 390mm distances from their centerline. A schematic of how the breakout shell was divided, with the relative location of the crack that caused the breakout, is shown in Figure 4.10.

Figures 4.11 through 4.15 show the breakout shell measurements as a function of distance below the top of the shell. The narrowface shell measurements, as well as those in the off-corner (390 mm) areas of the widefaces, show delayed shell growth near 300 to 400 mm below the top of the shell. This behavior is representative of shell thinning due to liquid steel impingement from the SEN onto the steel shell.

4.3 Breakout Shell Microstructure

Metallographic analysis was performed on samples taken from the breakout shell and from the solid strand just below. Thirteen samples were taken from the narrowface centerline, and thirteen samples were taken from the broadface slice located at 86mm from its centerline. These samples were obtained from select locations below the shell meniscus. Measurements were performed to determine the dendrite arm spacings and final columnar grain size.

Figures 4.16 and 4.17 show the dendritic structure in longitudinal sections taken at two different distances below the top of the breakout shell, through the center of the west narrow face. The dendritic structure was revealed using about 45s immersion in a solution of 10 g $CuCl_2$ in 50 ml HCl, 50 ml C_2H_5OH and 100 ml H_2O [30].

Figure 4.16 shows the microstructure between 8 and 10 mm below the top of the narrow face of the breakout shell, where the shell is only 1.00 mm thick. The secondary arm spacing is about 18 μm, and is relatively uniform across the sample. The corresponding primary arm spacing is variable, but averages 46 μm.

Figure 4.17 shows the microstructure taken 813 mm below the top of the narrow face of the breakout shell, where the shell is 11 mm thick. A close-up taken near the drained interface is shown. The secondary arm spacing is about 40 μm and the primary spacing is 127 μm. Note that the dendrites angle slightly upwards (opposite to the casting direction). The small white regions are carbide precipitates.

Figure 4.18 shows the increase in primary and secondary dendrite arm spacings measured down the breakout shell near the narrowface and wideface centerlines. All measurements were made near the drained interface. The dip in primary spacing along the narrow face appears to correspond with the point of jet impingement that causes the dip in shell growth at about the same distance.

Sample sections were etched to reveal the columnar grain structure in a representative region of the slab. Macro-etching was performed using Villellas s etchant. Figure 4.19 presents a horizontal section through the strand, from the west narrow face to the wide face centerline, and including the longitudinal crack that later started the breakout. This section was taken 127 meters below the top of the breakout shell, where casting conditions were reasonably typical of steady state. Anomalous features are the longitudinal crack, and corresponding bulging of the narrow face inside radius. The crack is 32 mm deep and 10 mm wide at the surface of this section. Note that the final grain structure, shown in Figure 4.19, is almost 100% columnar. Most of the structure consists of grains that span across half the strand thickness, making them 65 mm long. Their width varies from 2 to 7 mm.

In several micrographs, intermittent dark bands of enriched solute traverse across the dendrites, roughly parallel to the solidification front. They were observed only at locations near the drained interface where the liquid jet likely impinges directly on the shell. As shown in Figure 4.11, they are 0.75 to 1.64mm beneath this interface on the narrowface centerline (0.57mm beneath the wideface) and extend from 305 to 610mm below the meniscus along the NF (508 to 610mm down the wideface).

4.4 Mathematical Modeling of Breakout Shell Growth

An analysis was performed to evaluate shell growth predictions, produced from the CON1D mathematical model, against measurements and data obtained from the ARMCO breakout shell. In addition to the information described in the previous sections, profiles for transient casting speed, overall mold heat flux, and steel superheat flux must be derived to model shell growth.

4.4.1 Derivation of Transient Casting Speed Profiles

Transient casting speeds for positions on the breakout shell were derived from the casting speed versus time data presented in Figure 4.7. The top of the shell is assumed to form when the casting speed first starts to decrease, at 7184.2 seconds. Casting speeds for positions below the top of the shell are extrapolated based on the steady-state casting speed that exists before the breakout hole forms. Figure 4.20 shows casting speeds for selected positions on the shell as a function of time. Final solidification times for each position on the breakout shell is also included.

By utilizing the transient casting speed profiles along with the liquid level position, the shell solidification within the mold can be better understood. Figure 4.21 illustrates the movement of the shell during the breakout. Specifically, it presents distance versus time histories for several points on the strand surface, which eventually becomes the breakout shell. These curves were derived from the time-dependent casting-speed data in Figure 4.7, by summing the instantaneous casting speed multiplied by the time increment, for different starting times. Zero distance corresponds to the position of the steady-state meniscus, normally held by the mold level controller at 104 mm below the top of the mold. A reconstruction of the mold level history is presented on the same graph. The beginning of the curve is taken from the recorded data in Figure 4.7. Beyond 7190 seconds, the curve was extrapolated by estimating the drainage time [31], based on a 19x480 mm hole and initial head of 1450 mm. Schematics of the breakout shell are superimposed on the graph at three critical times to illustrate the events during the breakout. The time when the level first starts dropping at 7178 seconds indicates when the breakout hole first forms. Intersecting this time with the curve representing movement of the end of the breakout hole reveals that the breakout hole starts as a short hole just below the mold exit. The shell and hole both grow for the next 12 seconds, as the input of new liquid partly compensates for the losses through the breakout hole. Then, at 7190 seconds, the top of the final breakout shell forms, as the input flow of new steel stops and the shell drains. When withdrawal finally stops at 7210 seconds, this point has traveled to 385 mm below the original liquid level position. Because the shell drains fairly quickly, it is reasonably representative of steady casting conditions. The solidification time for any position on the steel surface can be obtained from Figure 4.22, by subtracting the time a given point first drops below the liquid level (often at distance = 0) from the time the level later drops below its current position, as indicated by the intersection of the two curves. This information is included in Figure 4.22, which magnifies the initial portion of a few shell thickness plots. In general, the solidification time is almost directly proportional to distance along the breakout shell. However, this is not quite true at early times (less than 10s for this breakout). Initially, points on the breakout shell move downward faster than the level drops. Thus, the top of the breakout shell forms below the steady-state meniscus level. This portion of the shell is covered by molten steel longer than the initial portion of a shell cast under steady-state conditions would be. Thus, the distance between each second of solidification time in Figure 4.22 is shorter at early times. This finding explains why model predictions of the steady-state shell thickness might underpredict the breakout shell thickness near the meniscus. Models based on matching the local solidification time should match the breakout shell profile more readily.

Figure 4.22 shows that drainage through the breakout hole did not appear to have much influence on shell growth, as shell growth beside the breakout hole is similar to that across the mold on the outer radius. Shell growth at both the narrow face and off-corner sections of the wideface are generally reduced relative to the central regions of the wide face. This is likely due to superheat from the impingement of the strong jets that flow from the nozzle ports and expand as they traverse across the mold. The east side is a generally a little thicker than the west side, for reasons unknown.

4.4.2 Mold Heat Flux Profiles

As mentioned previously, ARMCO possesses an instrumented mold, containing 106 thermocouples, to measure mold heat flux. Figure 4.23 shows the position of the thermocouples within the instrumented mold. Thermocouples were aligned vertically between the bolt holes and extended to 24 mm below the wide face copper hot face and 12 mm below the narrow face according to the design given in Figures 4.4 to 4.6. Each thermocouple consists of a 2-mm diameter constantan wire or stud which is welded to the bottom of its inset hole in the back of the copper plate. The copper mold itself serves as the copper portion of the thermocouple junction. To keep water out of the inset hole, the constantan wire is sheathed with an insulating plastic plug.

The mold that was used during the breakout event was not instrumented with thermocouples, so no measurements of mold heat flux values during the breakout are available. In an attempt to obtain typical temperatures during steady casting conditions similar to those just prior to the breakout, mold temperatures were obtained from a heat that had similar, representative casting conditions. The mold geometry is the same as given in Table 1.1, as the mold was new. Casting conditions are the same as the breakout conditions in Table 4.2, except that powder C was used (see Table 4.3).

Figure 4.24 presents the measured temperatures for 86 thermocouples, (excluding the 625 mm columns). Measured mold cooling water temperature differences averaged: 7.44 ßC (IR), 7.45 ßC (OR), 7.93 ßC (West NF) and 8.05 ßC (East NF). Near the meniscus, the actual mold temperature between the measured points is expected to be much higher. A vertical arrow indicates the estimated location of the maximum mold temperature, which is about 40 mm below the liquid level. Note that wideface temperatures near to the narrow faces (475 mm) are consistently lower on both the inside radius (IR) and outside radius (OR). The narrow faces consistently record the highest temperatures.

Values for mold heat flux were derived from the thermocouple measurements obtained from the representative case. Figure 4.25 shows calculated mold heat flux values for the different faces of the mold. Notice that heat flux values for the mold narrowfaces are consistently higher than those for the widefaces. For purposes of modeling shell growth, heat flux profiles for the loose wideface were used.

4.4.3 Liquid Superheat Flux Profiles

A CFD analysis of fluid flow within the ARMCO casting mold has been performed by Creech [32] which incorporates the SEN design to model the superheat input to the steel shell due to liquid steel impingement. Superheat profiles are given in Figure 4.26, which show values for selected shell measurement planes as a function of distance below meniscus.

4.4.4 Comparison of Model Predictions against Breakout Shell Measurements

Figures 4.27 through 4.29 show model predictions of shell growth against breakout shell measurements for near the middle of the wideface, near the offcorner of the wideface, and near the middle of the narrowface. Predictions for the wideface shell thicknesses compare quite well with the data from the shell measurements. Predictions for the narrowface shell thicknesses tend to underpredict the data from the shell measurements. This is expected, since the heat flux values used for all three cases were based on the loose wideface data obtained from the ARMCO instrumented mold, and that the narrowface heat flux values obtained from the mold are higher than those of the loose wideface.

4.5 Conclusions

This chapter has focused on the analysis of the breakout conditions which produced the ARMCO breakout shell. Casting conditions and process parameters significant to modeling shell growth were collected and analyzed. This data was used to assess the accuracy of the CON1D mathematical model and its capabilities of modeling shell growth, through comparison of model predictions with breakout measurements.

Table 4.1: Mold Geometry

	Widefaces	Narrowfaces
Copper wall thickness	35.0 mm (new)	25.0 mm (new)
Total copper plate width	1560 mm	132.1 mm
Copper plate length	1200 mm	1200 mm
Distance between cooling water channels	21.5 mm	30.0 mm
Start of slots from mold top	25 mm	30 mm
Cooling water slot depth	5.0 mm (34 slots) 5.0 mm (13 slots) 10 mm (22 slots)	12 mm (8 slots)
Cooling water channel width	16.0 mm (34 slots) 14.0 mm (13 slots) 6.0 mm (22 slots)	5.0 mm (8 slots)
Channel cross sectional area	4865 mm^2 (each WF)	462.7 mm^2 (each NF)
Water flow rate	0.05677 m^3/s (IR) 0.05677 m^3/s (OR)	0.00631 m^3/s (East) 0.00631 m^3/s (West)
Cooling water velocity	11.67 m/s	13.64 m/s
Restraining bolts	11 across x 12 down (each WF)	12 studs (each NF center)

Table 4.2: Casting Conditions

		Steel Composition (434 Cr Steel)			
Casting speed	25.4 mm/s				
Strand thickness	132.1 mm	0.047	%C	0.10	%Cu
Strand width	984.0 mm	0.48	%Mn	0.008	%Sn
Tundish depth	990 mm	0.026	%P	0.0	%Ti
SEN submergence depth	127.0 mm	0.001	%S	0.003	%Al
Pour temperature	1563.0 ßC	0.39	%Si	0.020	%Co
Meniscus dist. from mold top	104.0 mm	16.71	%Cr	0.026	%V
Mold conductivity	315.0 W/mK	0.20	%Ni	0.010	%Nb
Cooling water pressure	0.62 MPa	1.00	%Mo	0.056	%N

Table 4.3: Mold Powder and Flux Properties

	A	B	C
Powder Composition			
% SiO_2	29.4	33.8	38.4
% CaO	28.8	33.9	39.2
% Na_2O	9.3	10.6	2.0
% Fe_2O_3	11.0	0.3	0.7
% MgO	0.5	2.4	3.4
% Al_2O_3	6.6	6.2	5.0
% F	7.3	5.7	9.3
% S, % CO_2	-	-	0.6, 2.8
% other oxides			3.5
% C	6.0	4.1	2 .6
Flux Viscosity @ 1300 ßC	1.4 Poise	2.3 Poise	2.0 Poise
Crystallization temp.	1140 ßC	1146 ßC	1135 ßC
Powder layer depth	52 mm	18 mm	17 mm
Liquid layer depth	6 mm	17 mm	18 mm

Figure 4.1: View of Breakout Shell

Figure 4.2: View of longitudinal crack which initiated breakout event

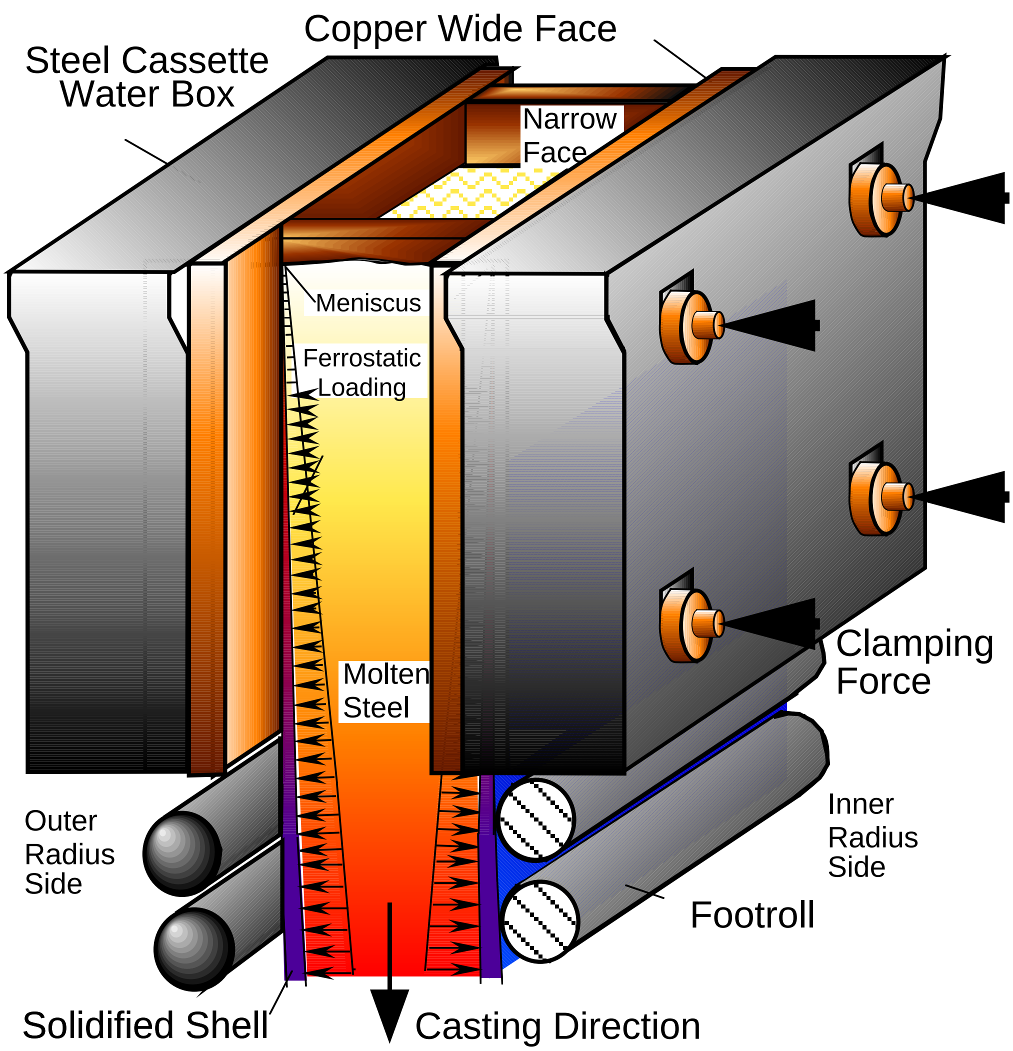

Figure 4.3: View of mold construction [29]

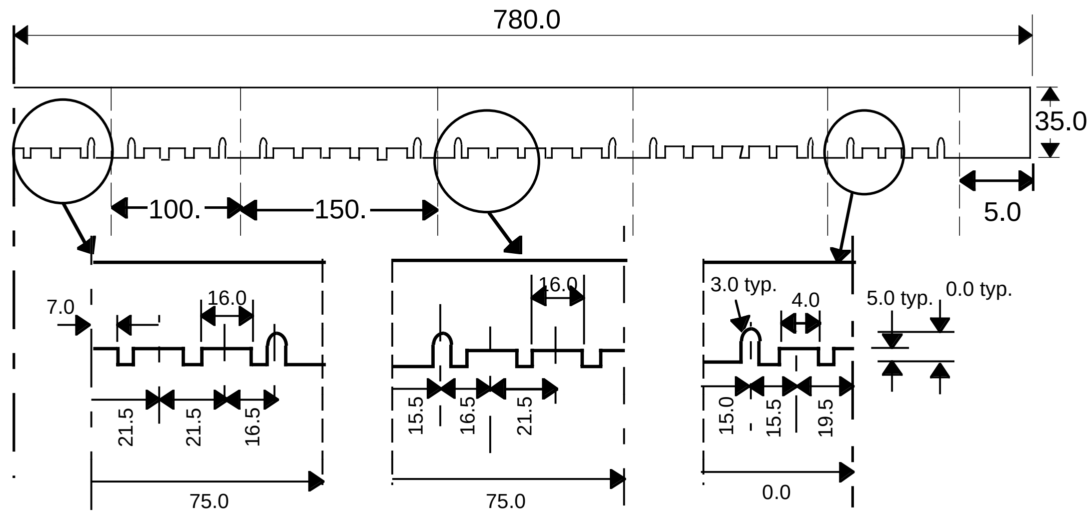

Figure 4.4: Schematic of copper mold wide face design, including water channel dimensions

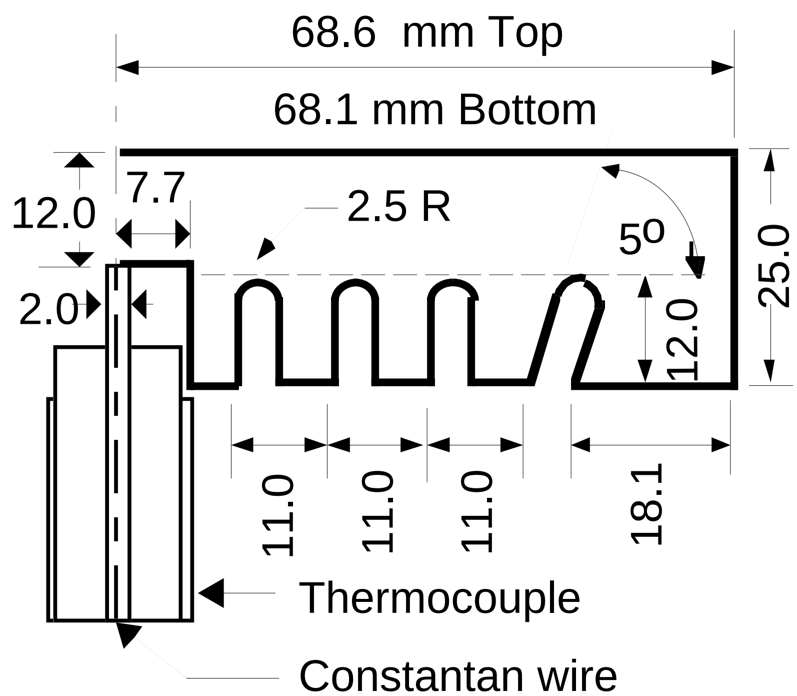

Figure 4.5: Schematic of copper mold narrowface design, including water channel dimensions and thermocouple location

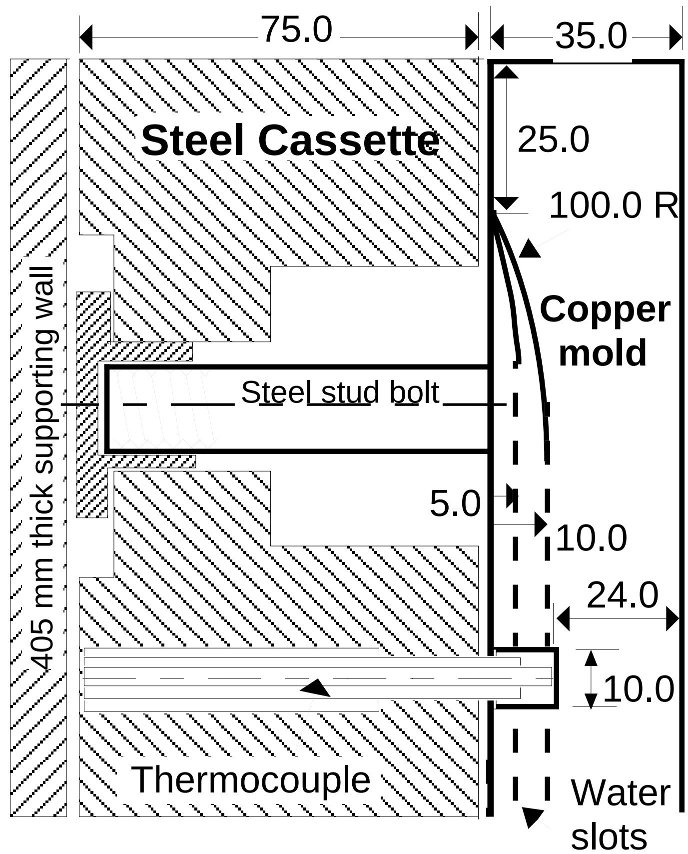

Figure 4.6: Construction of Steel Cassette, copper wideface plate, and thermocouple location

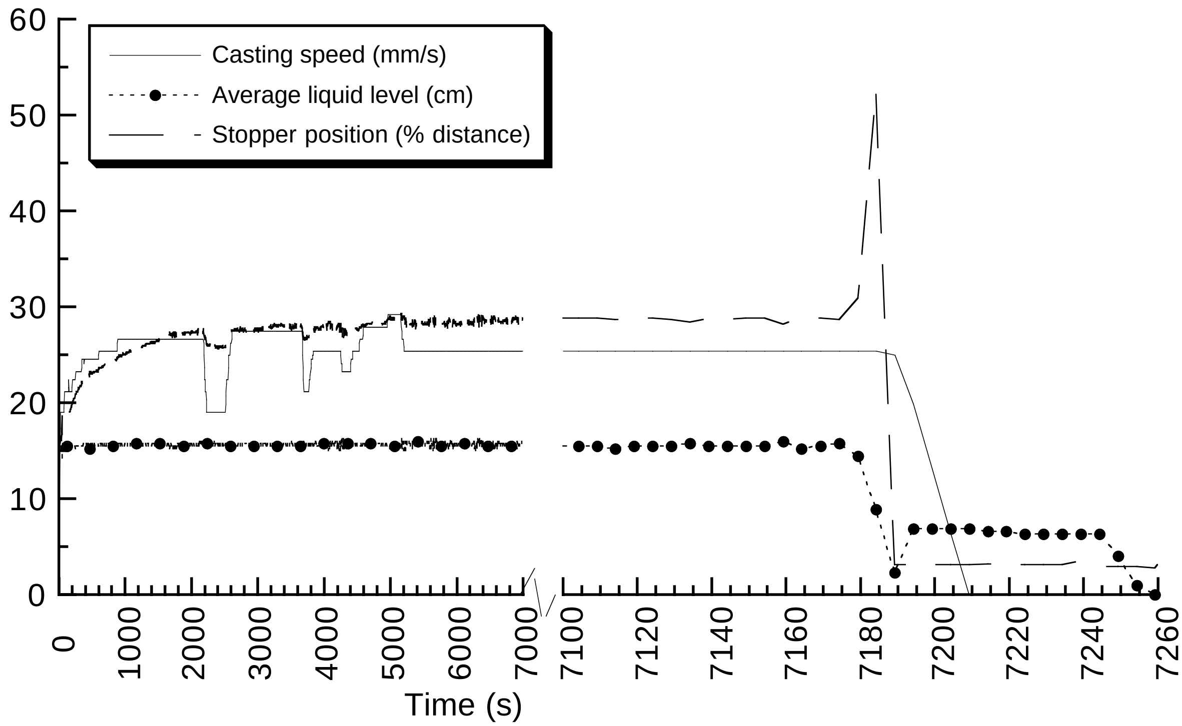

Figure 4.7: Casting Speed, Average Liquid Level, and Stopper Rod Position versus Time for Breakout Event

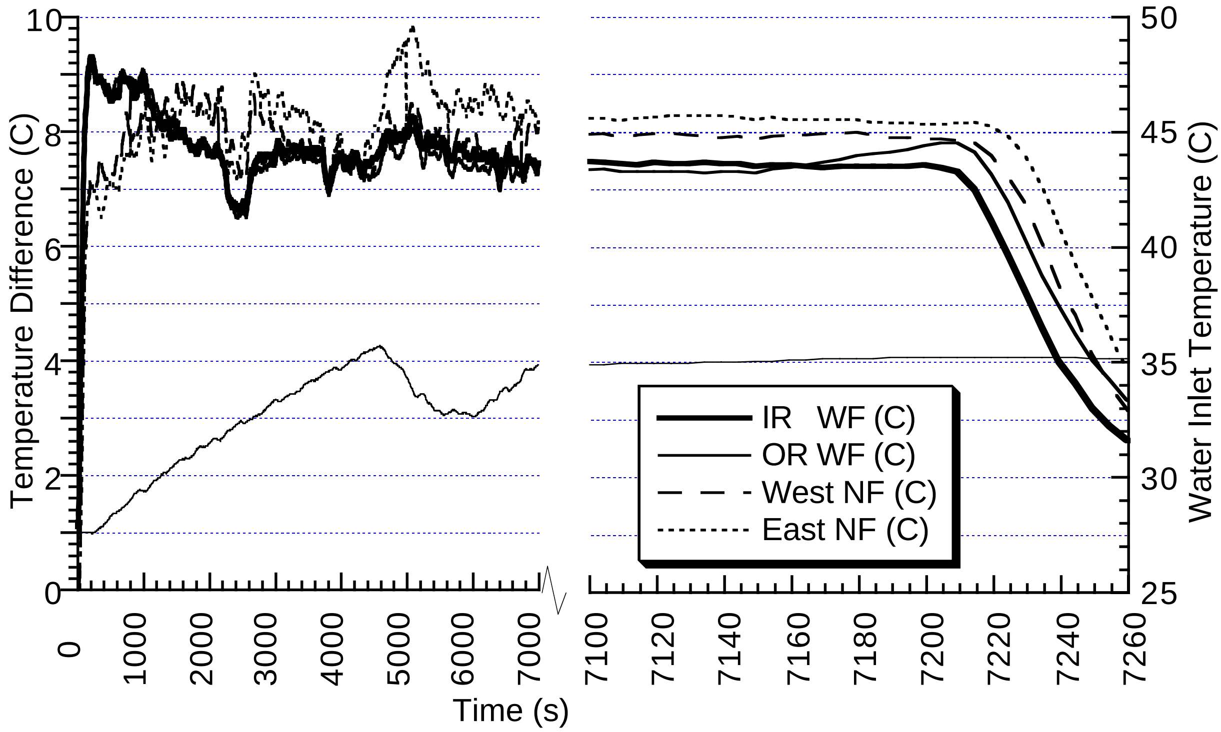

Figure 4.8: Mold Water Temperature Differences versus Time for Breakout Event

Figure 4.9: Oscillation Mark Pattern on Narrowface of Breakout Shell. Casting direction is downwards.

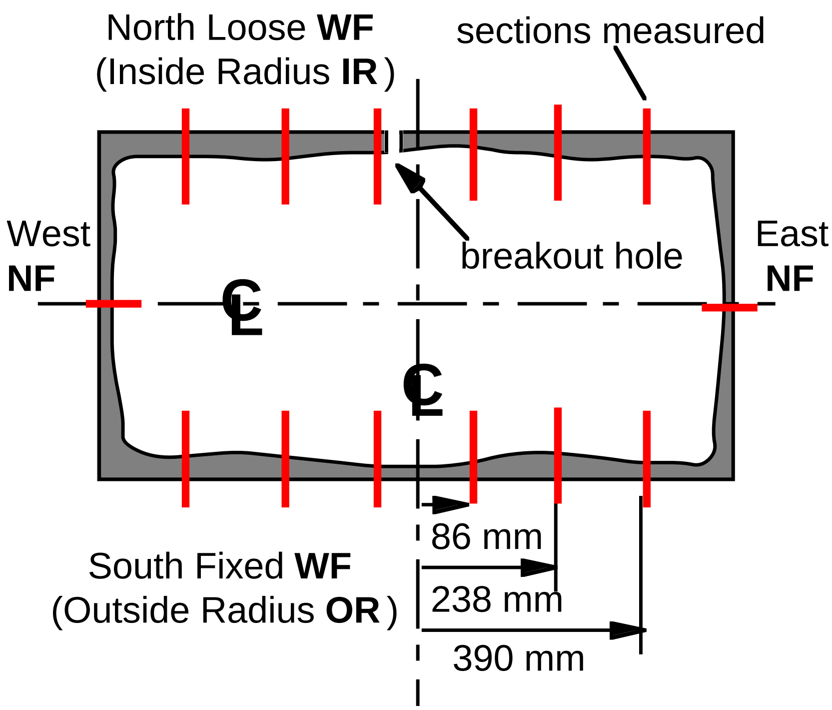

Figure 4.10: Schematic of Breakout Shell Measurement Locations

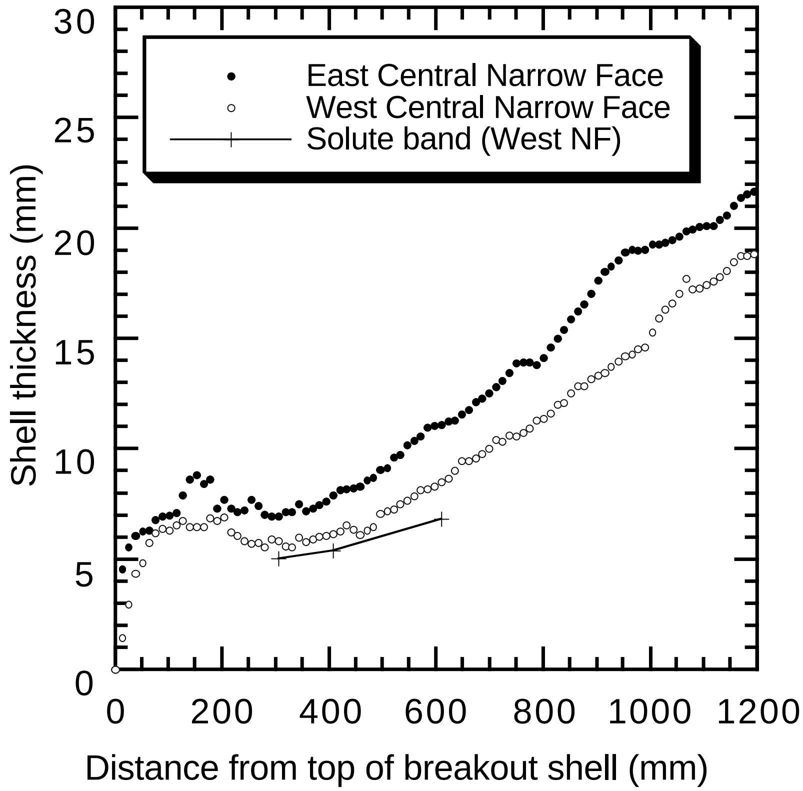

Figure 4.11: Measurements of Narrow Face Shell Thickness versus Distance from Top of Breakout Shell, along with locations of Solute bands identified in Micrographs

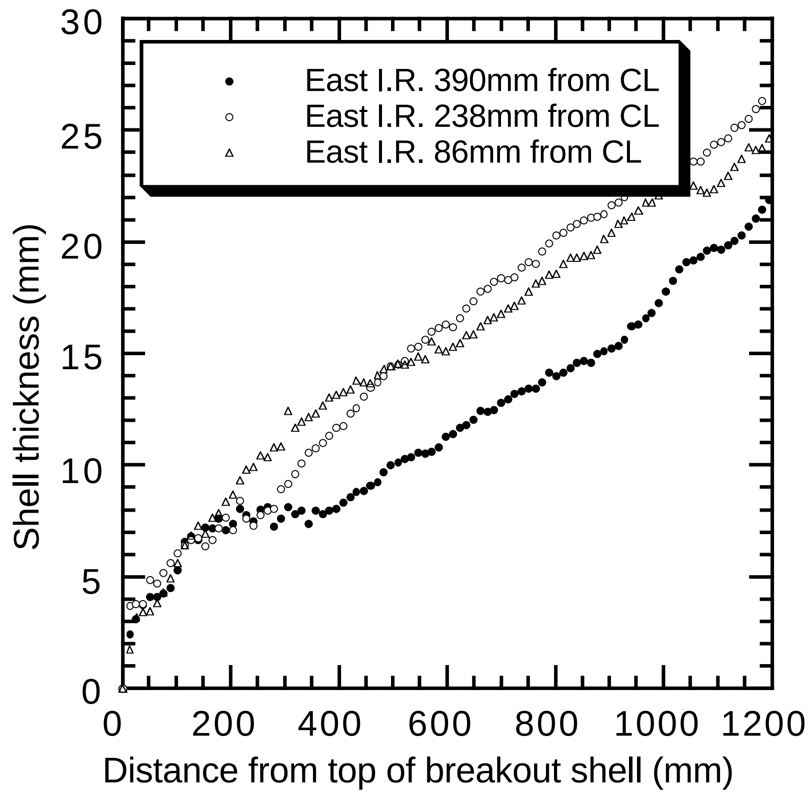

Figure 4.12: Measurements of East Inside Radius Shell Thickness versus Distance from Top of Breakout Shell

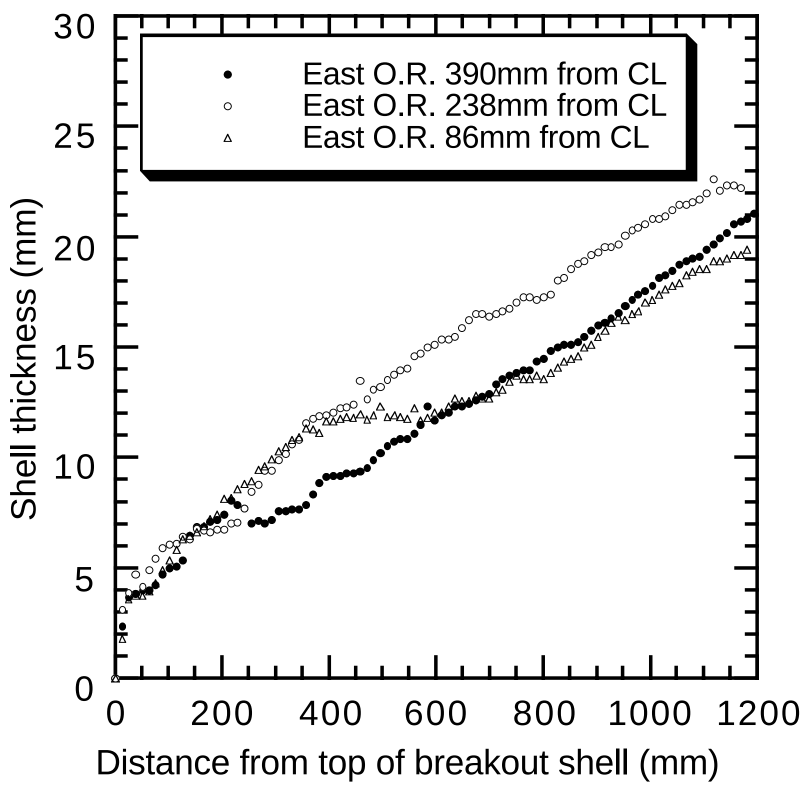

Figure 4.13: Measurements of East Outside Radius Shell Thickness versus Distance from Top of Breakout Shell

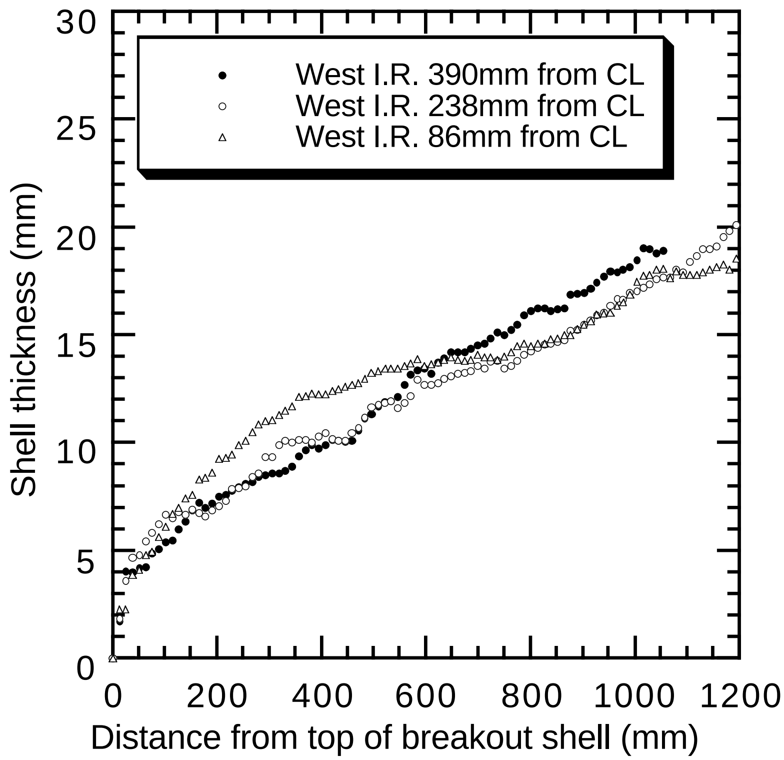

Figure 4.14: Measurements of West Inside Radius Shell Thickness versus Distance from Top of Breakout Shell

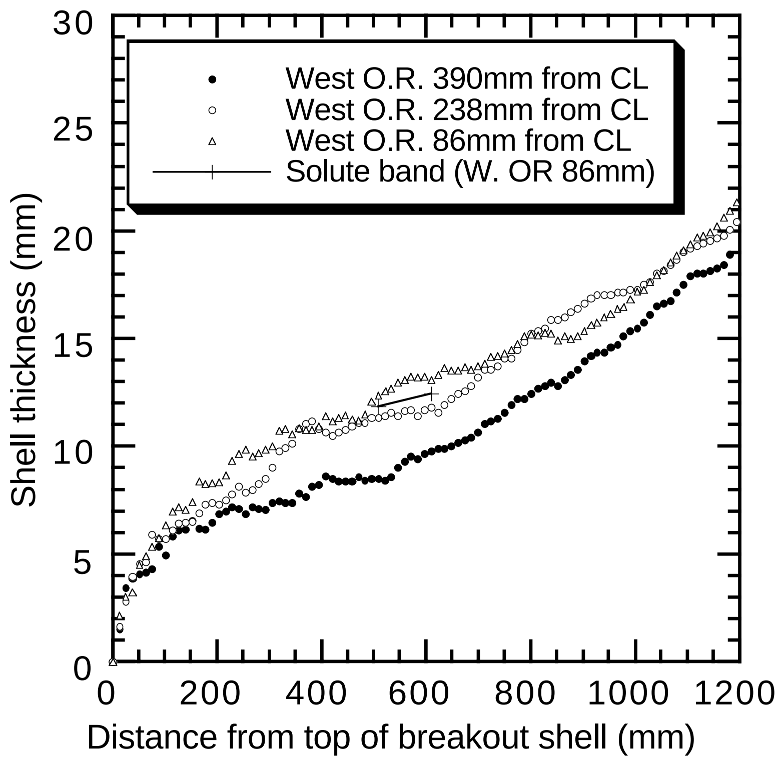

Figure 4.15: Measurements of West Outside Radius Shell Thickness versus Distance from Top of Breakout Shell, along with locations of Solute bands identified in Micrographs

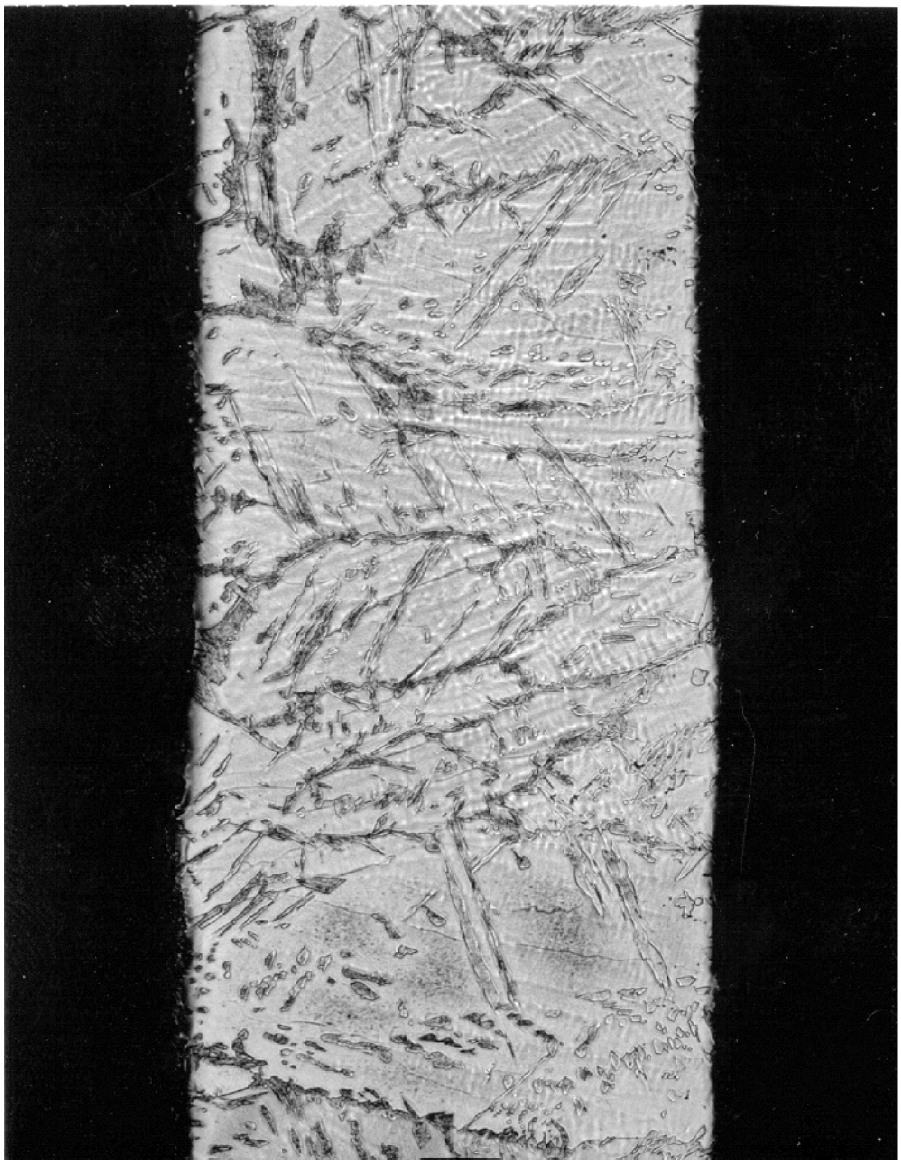

Figure 4.16: Dendritic Structure near top of Breakout Shell Narrowface. Total thickness from Strand Surface (right) to Drained Interface (left) is 1.00 mm at the bottom

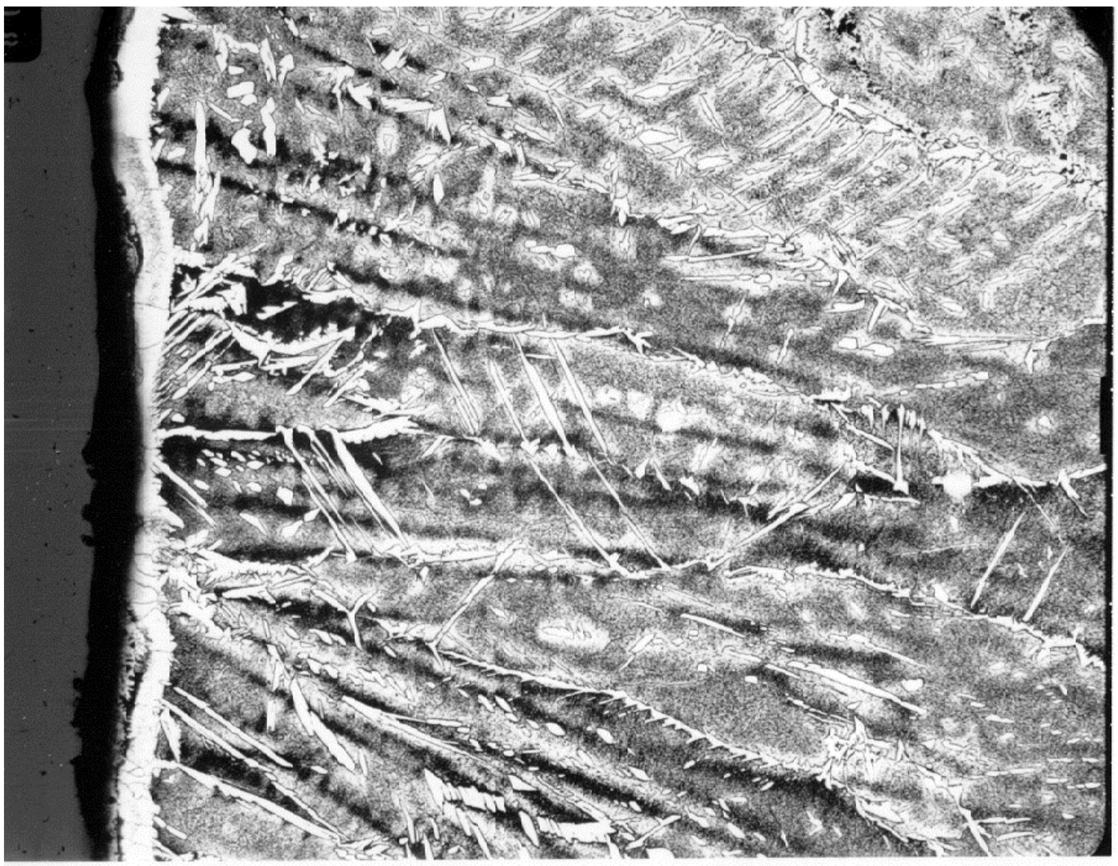

Figure 4.17: Microstructure of West Narrowface Centerline 813 mm below top of shell. Picture shows 2.15 mm of the total 11 mm Shell thickness. Drained interface is to the left; Casting Direction is downwards.

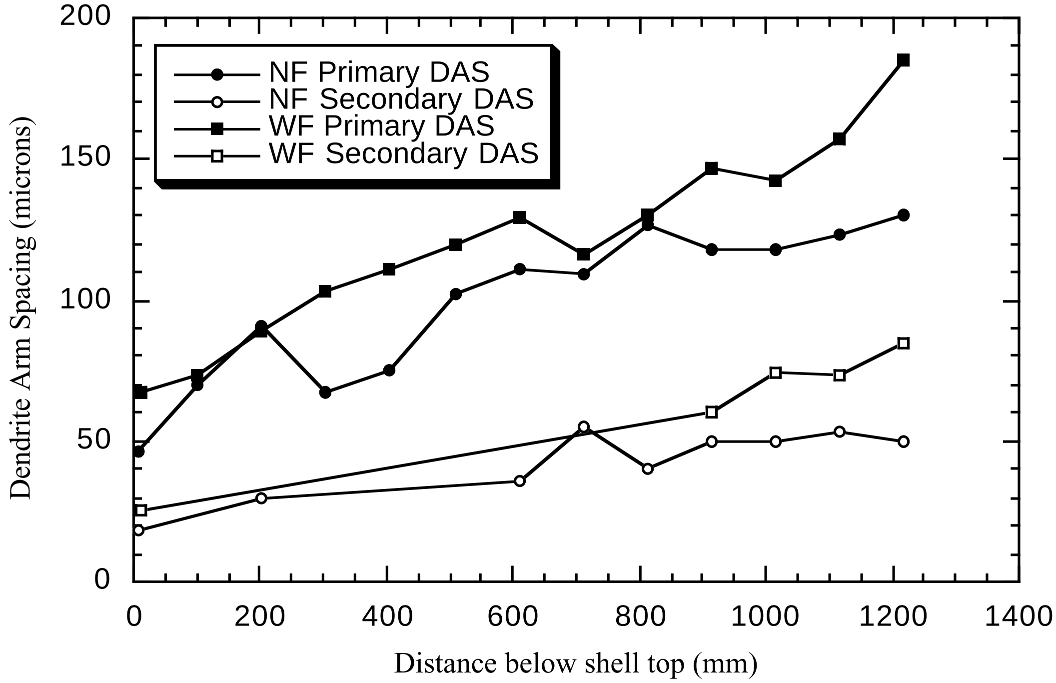

Figure 4.18: Measured Dendrite Arm Spacings for Different Distances down Shell Narrowface, Wideface

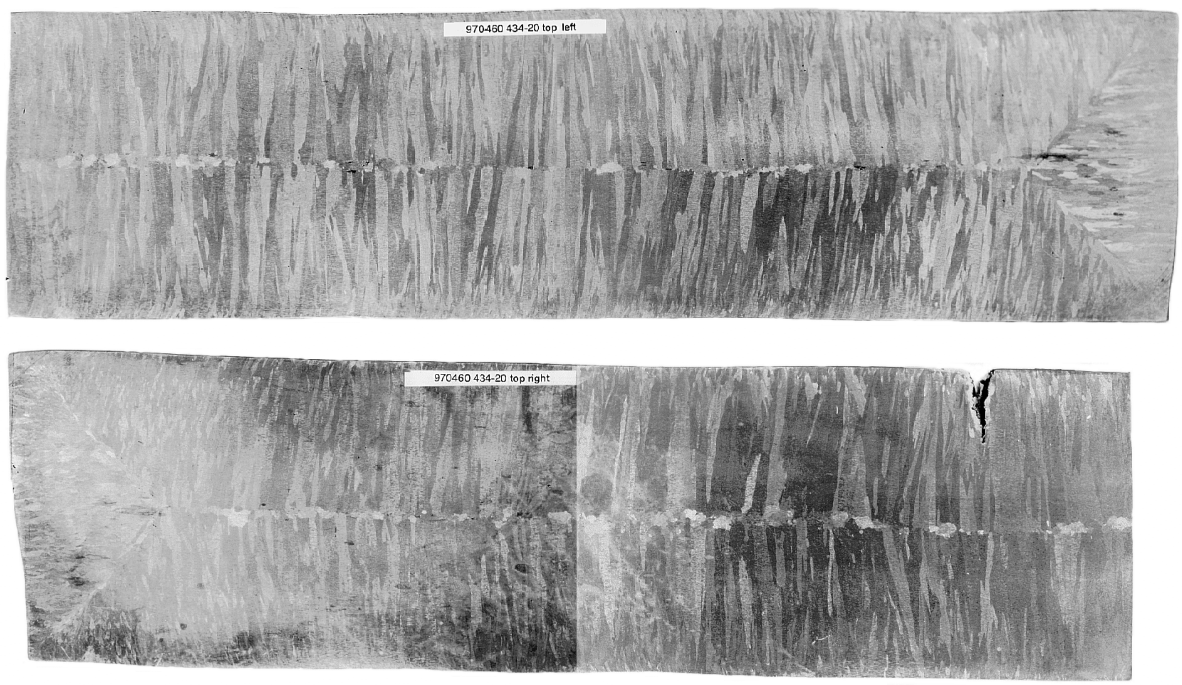

Figure 4.19: Horizontal Section of Breakout Shell, Macroetched with Villella s Etchant, Showing Grain Structure and Longitudinal Crack

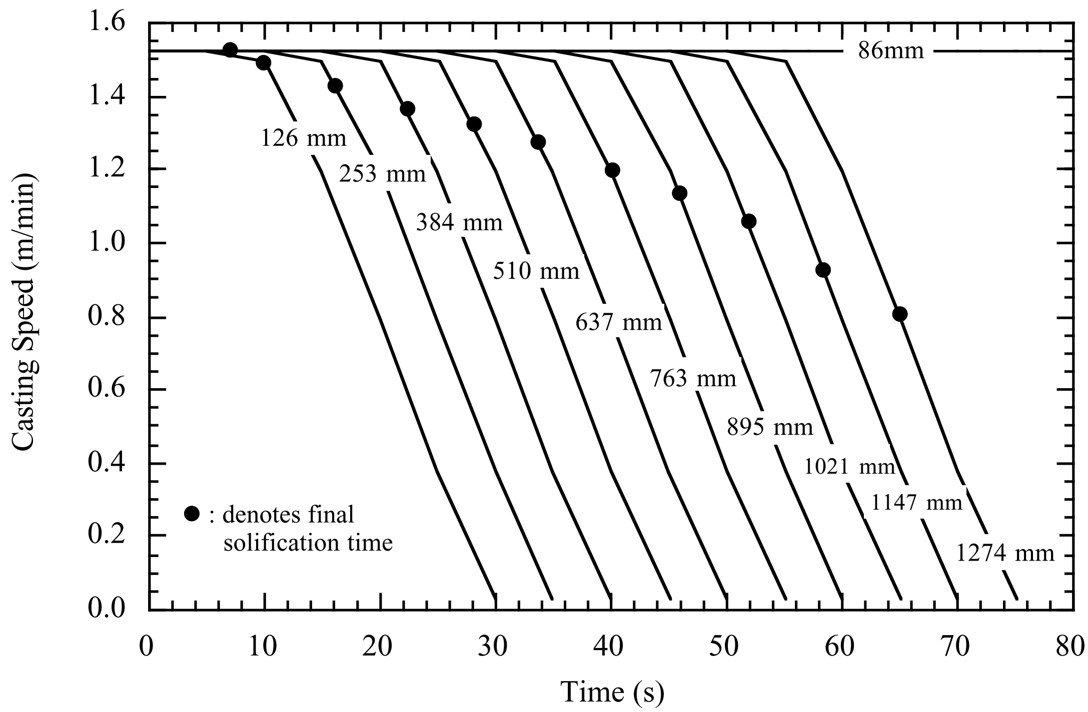

Figure 4.20: Plot of Casting Speed versus Time for Locations Along Breakout Shell

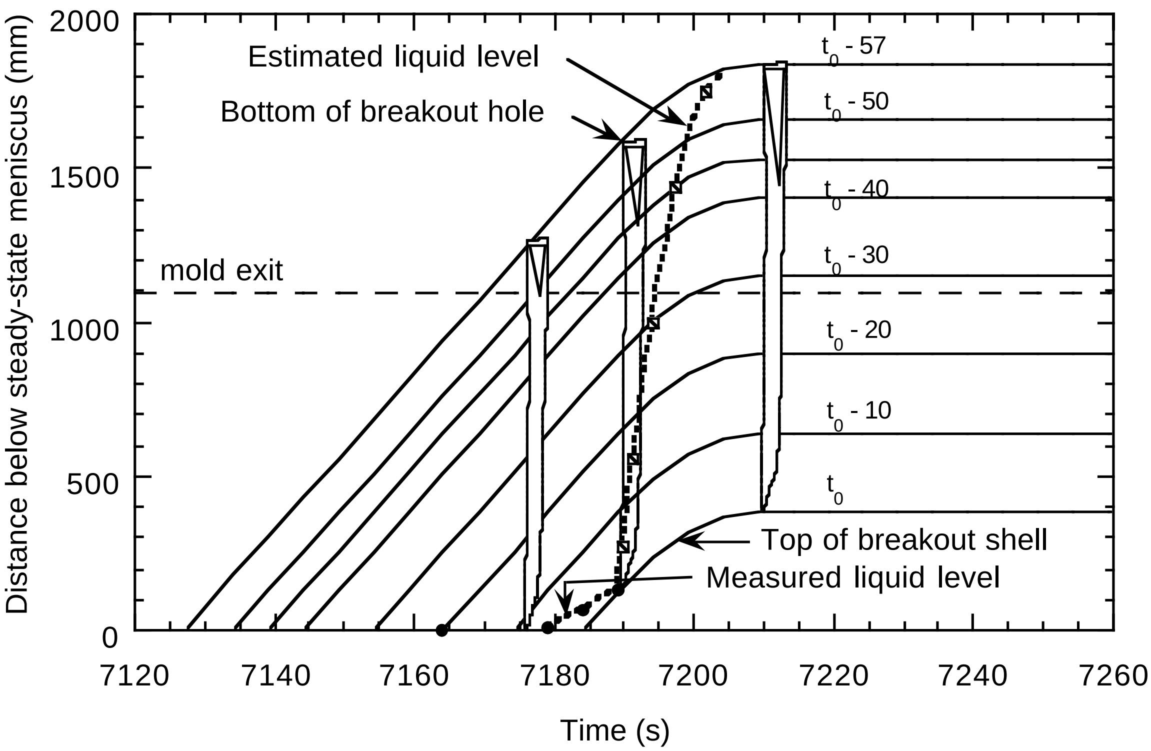

Figure 4.21: Liquid Level and Shell Growth versus Distance below Steady-State Meniscus Level

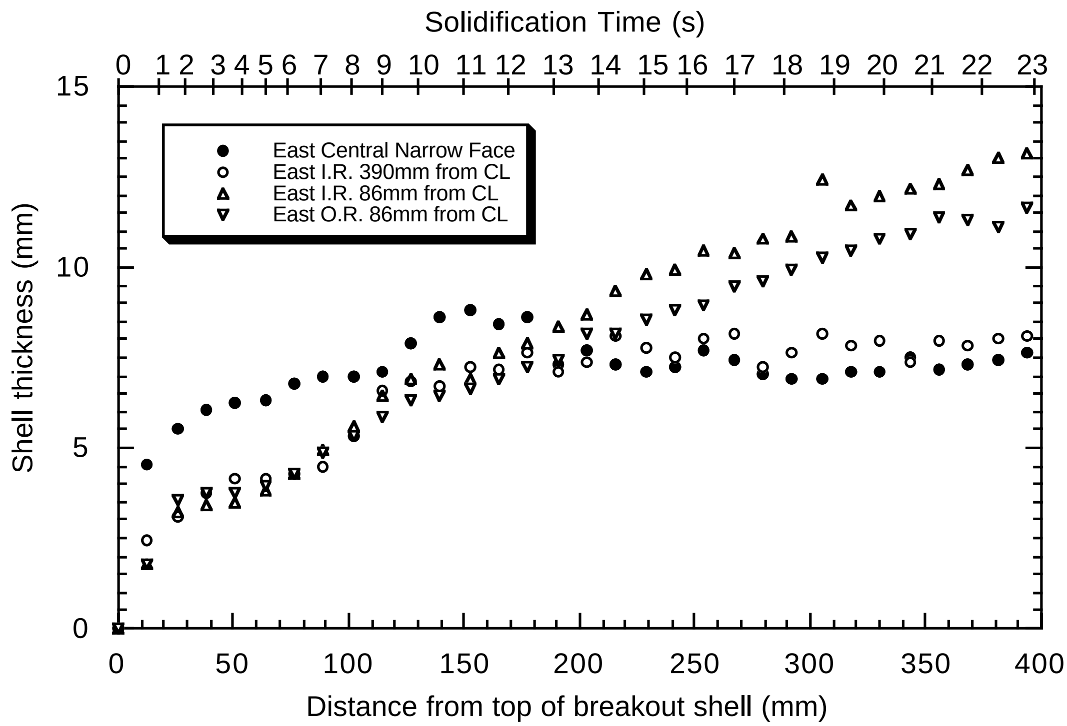

Figure 4.22: Plot of Initial Shell Growth and Local Solidification Time versus Distance from Top of Shell

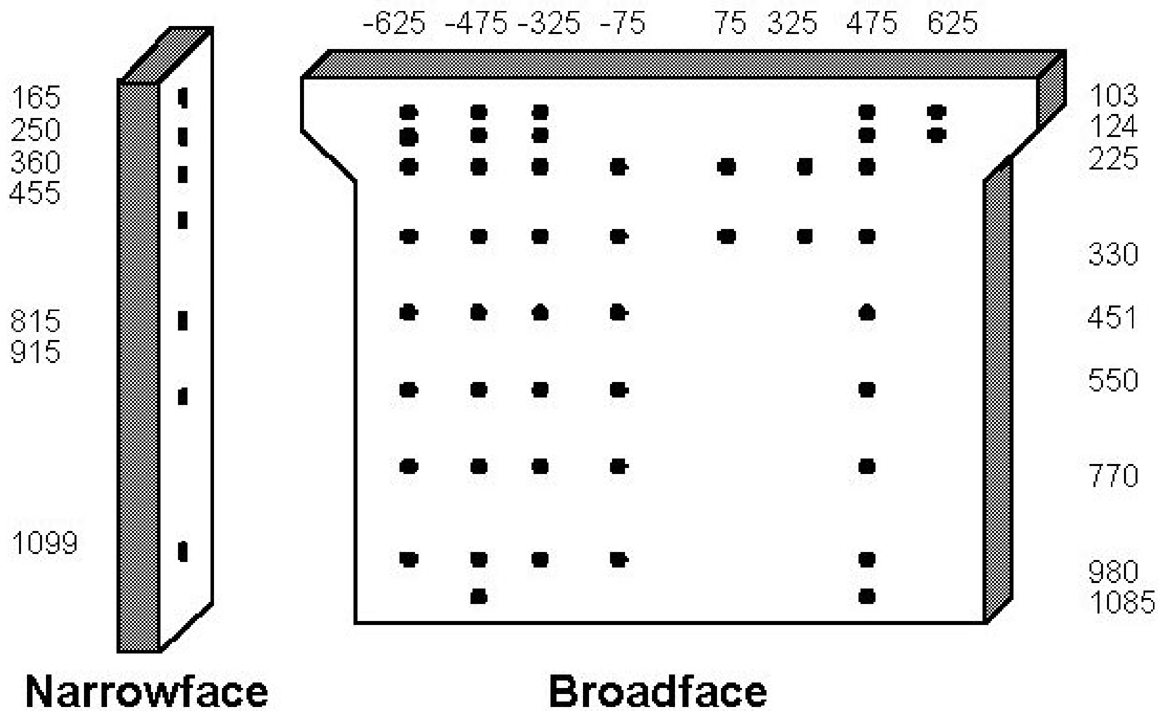

Figure 4.23: Location of Thermocouples within ARMCO Instrumented Mold [29]

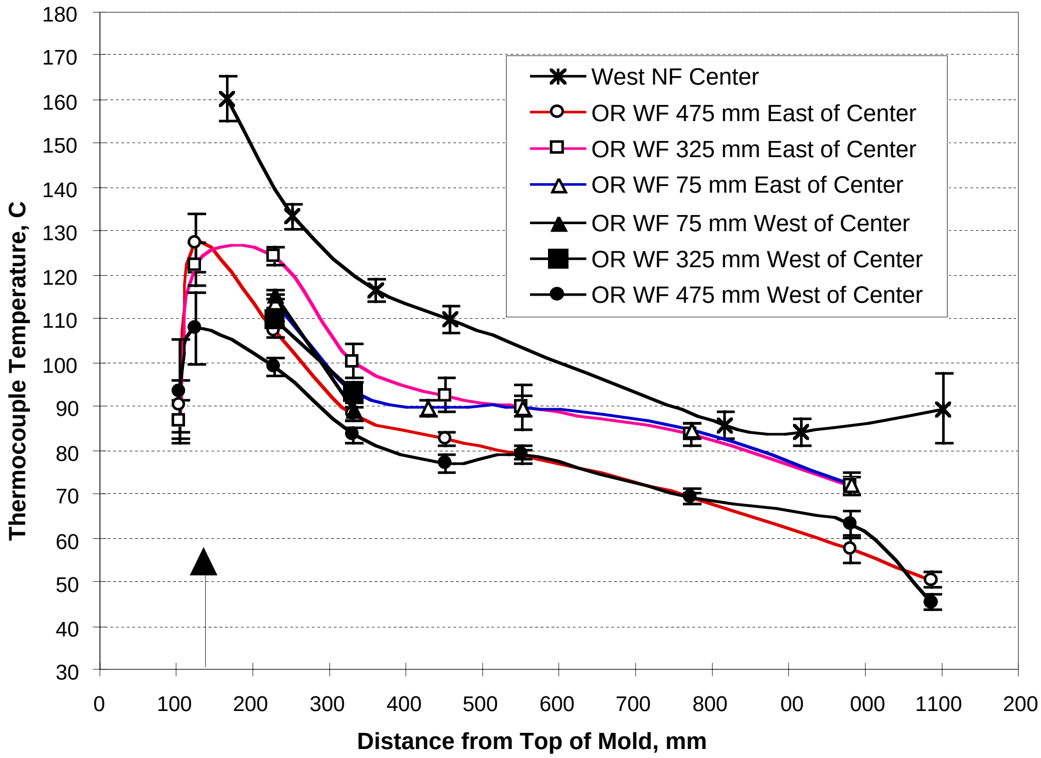

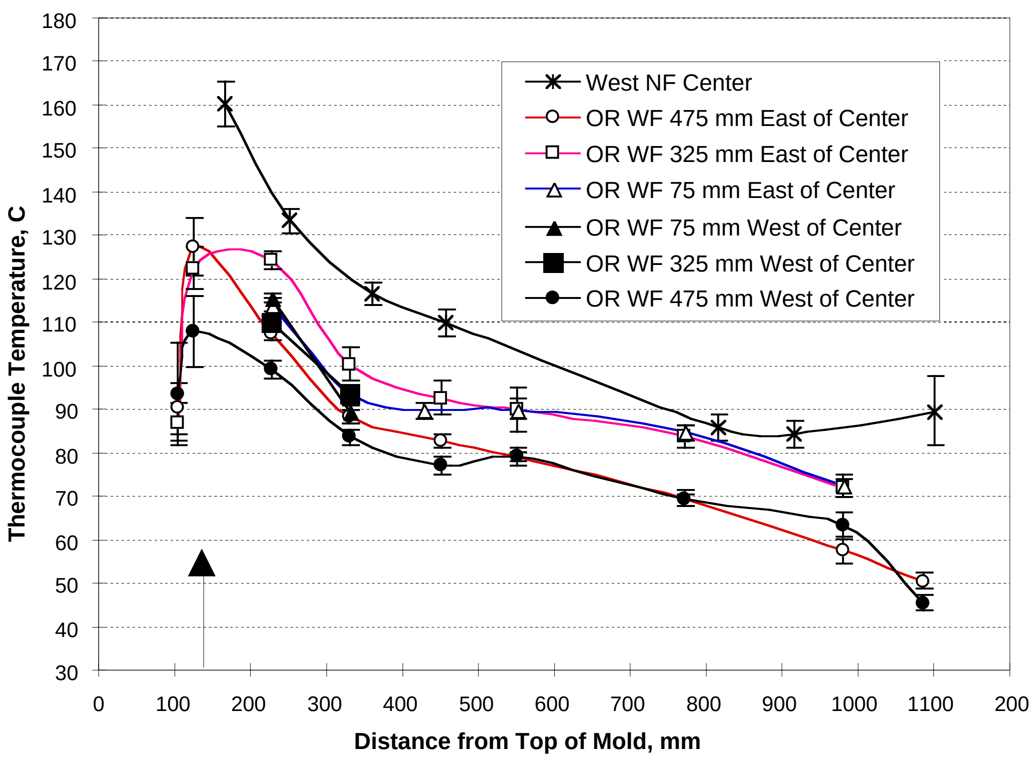

Figure 4.24: Typical Mold Temperatures

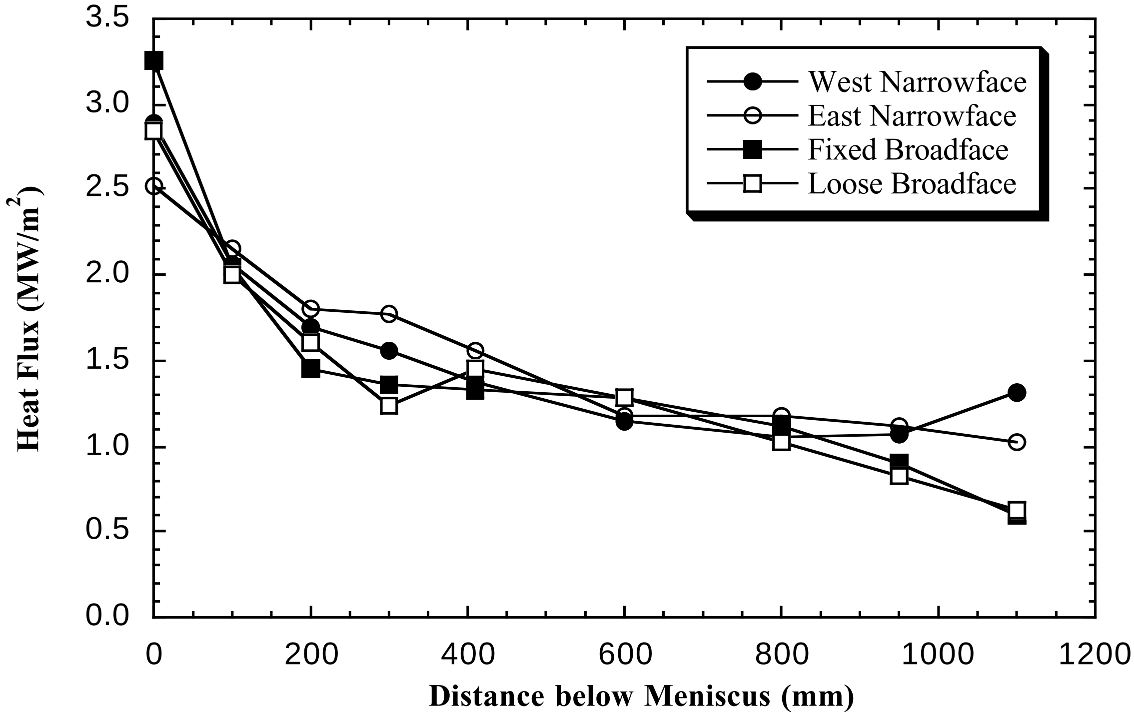

Figure 4.25: Mold Heat Flux Values Calculated from Mold Thermocouple Measurements

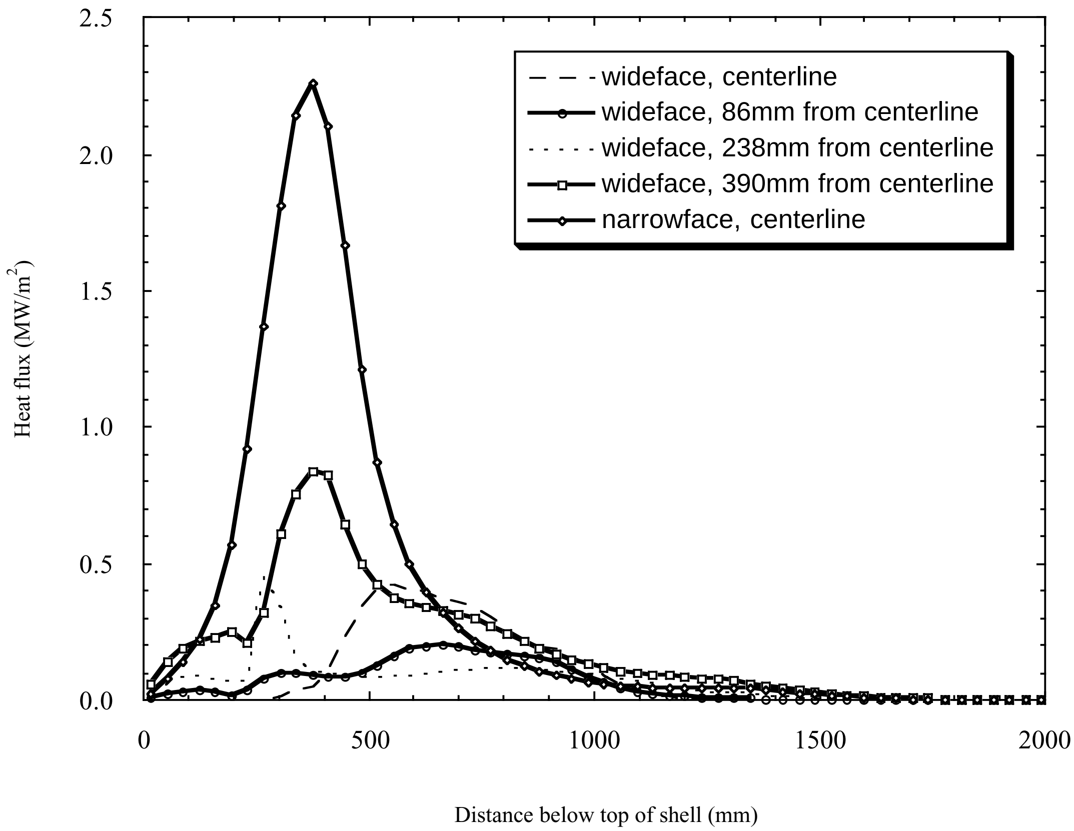

Figure 4.26: Superheat Flux Profiles versus Distance below Top of Shell, for Various Shell Measurement Positions

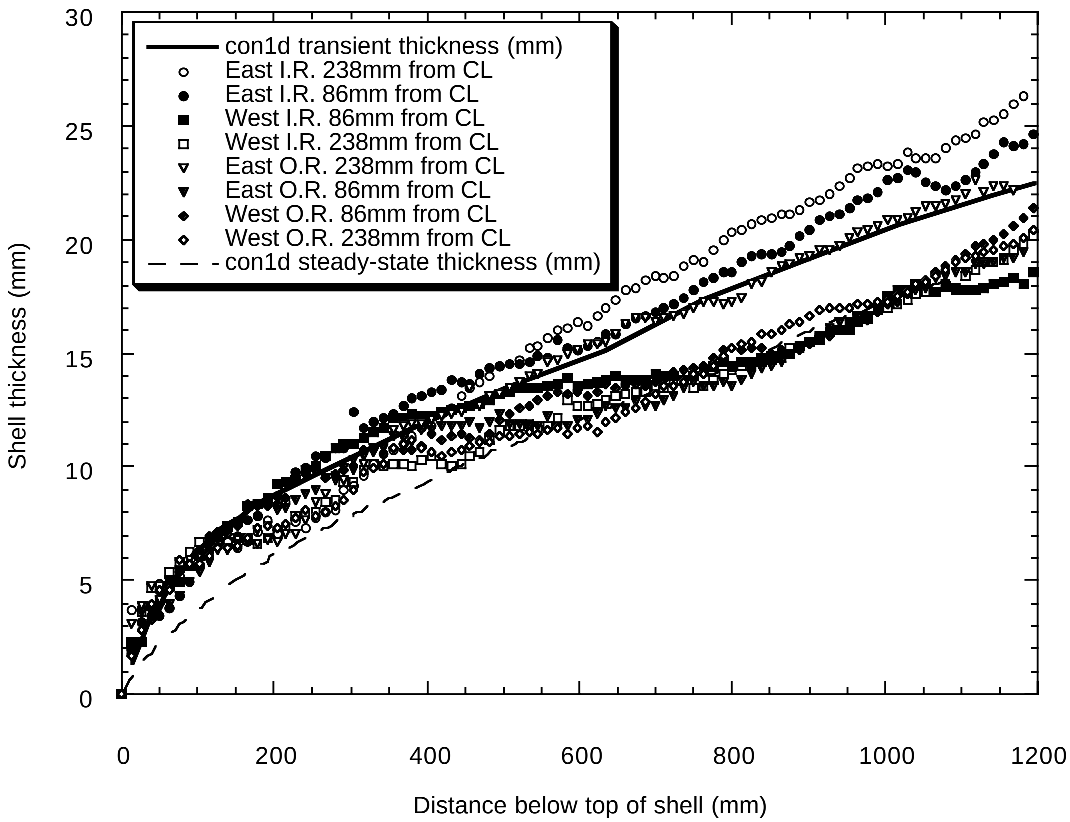

Figure 4.27: Comparison of CON1D Steady-State and Transient Shell Thickness Predictions Against Breakout Shell Measurements for Locations Near Wideface Centerline

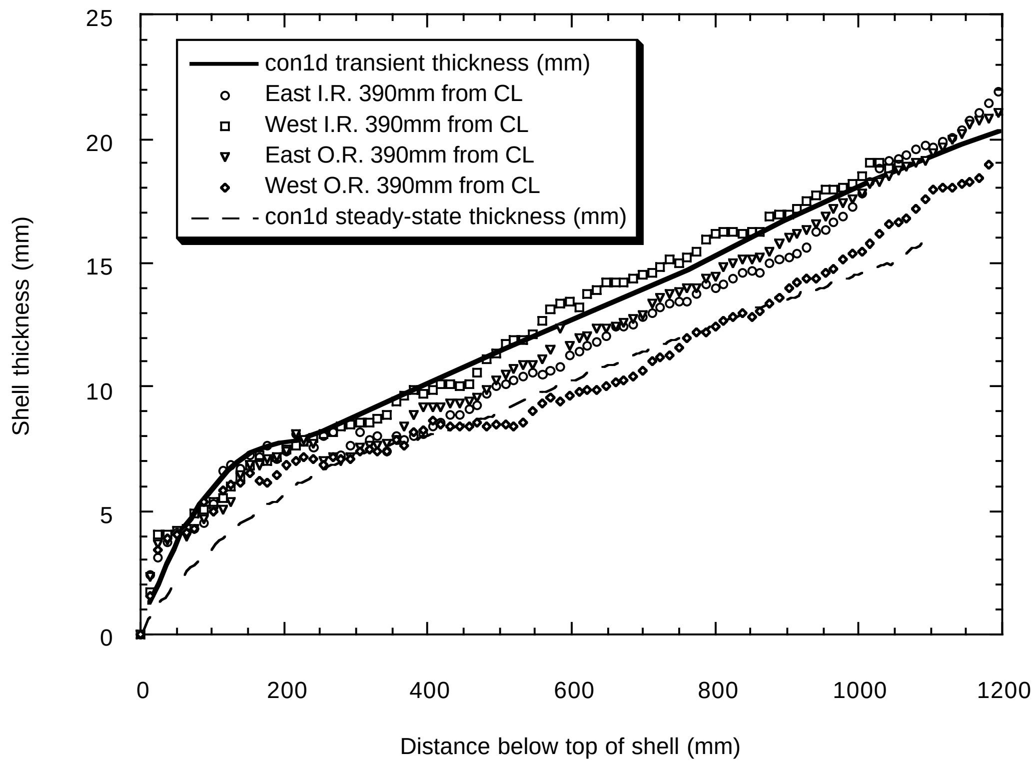

Figure 4.28: Comparison of CON1D Steady-State and Transient Shell Thickness Predictions Against Breakout Shell Measurements for Off-Corner Wideface Locations

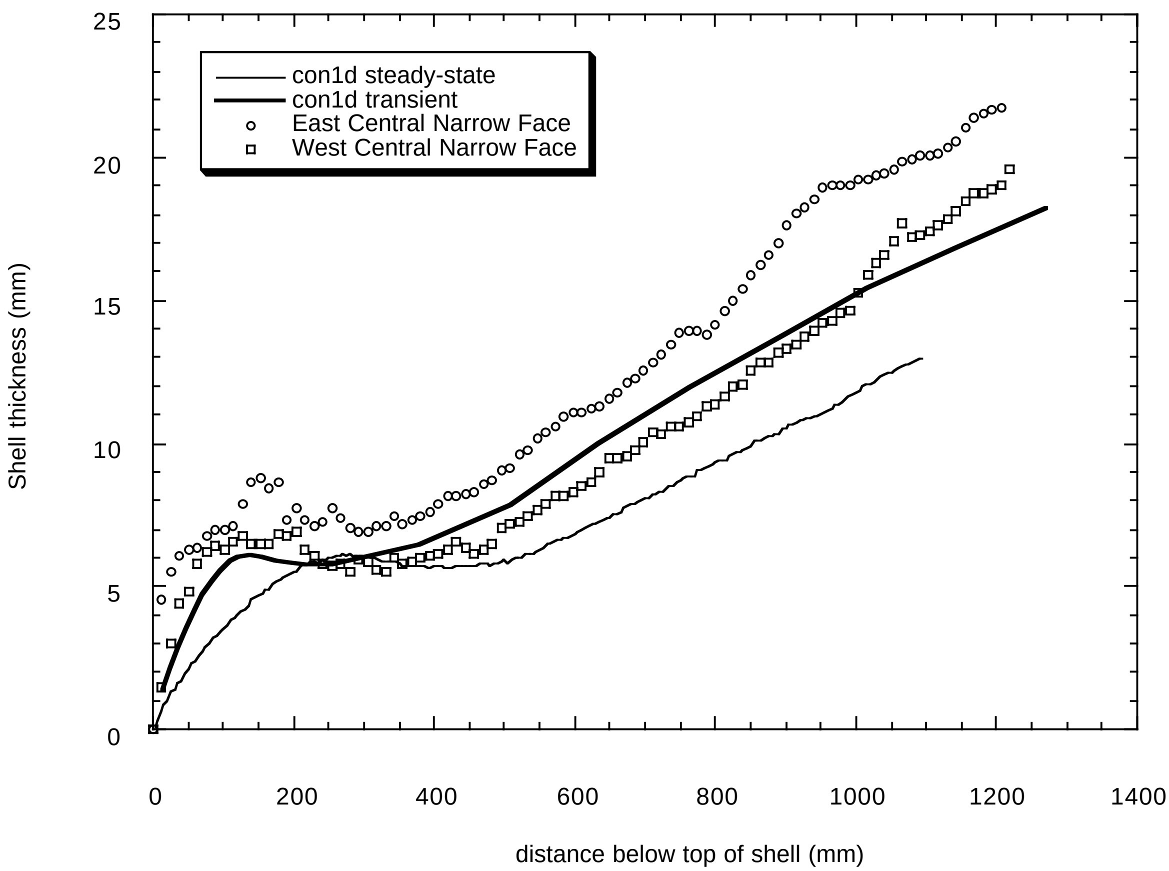

Figure 4.29: Comparison of CON1D Steady-State and Transient Shell Thickness Predictions Against Breakout Shell Measurements for Narrowface Centerline

5 CONCLUSIONS

Surface quality problems in continuous cast steel are greatly affected by heat transfer across the interfacial gap between the solidifying shell and the water-cooled mold. This work has focused on the use of mathematical models, experimental data, and plant measurements to quantify the effect of heat transfer across the flux film which is formed in this interfacial region.

5.1 Description of Mathematical Model

A mathematical model, CON1D, was developed to simulate heat transfer and solidification in the continuous casting mold. The individual aspects of heat transfer within the process were described, and focused on the equations which characterize interfacial heat transfer between the solidifying steel shell and the water-cooled copper mold. After describing the model, CON1D was validated against Hills' analytical solution for shell growth, and showed the numerical predictions to be within 5% of analytical results.

5.2 Mold Powder Experiments

An experimental method has been developed and applied to measure the thermal properties of mold flux under conditions similar to those found in the meniscus region of a continuous casting machine. The experiment reproduces important aspects of the continuous casting process, including the temperature-time history experienced by the flux. A set of one-dimensional models were applied to the experimental data to evaluate several thermal characteristics of the apparatus and flux film, including mold heat flux, gap conductivity, flux conductivity, and contact resistances between the mold and flux film, and between the flux film and steel. Models from the literature were also applied to the experimental data, which produced conductivity and contact resistance values which compared well with those reported in the literature. Specific findings include:

- The flux solidified in multiple layers similar to those observed from continuous casting molds and contained many gas bubbles.
- Flux thermal properties may change with time. In particular, the flux conductivity appears to decrease with time.
- The "measured" property values depend greatly on the model used to extract them. Flux conductivities in this work (including radiation but not interface resistances) averaged about 1.0 W/mK.
- Contact resistances at both interfaces were very important to heat transfer, especially in this particular apparatus, which simulates a rigid gap such as found in the corners of the continuous cast shell. Interface resistances averaged about 0.0015 m^2-K/W, which is equivalent to an air gap of about 0.1 mm.

5.3 Analysis of Breakout Shell

Measurements have been made to quantify a particular set of typical process conditions for the continuous casting of stainless steel slabs at Armco, Inc. in Mansfield, OH, focusing on the analysis of a breakout shell. The data include shell thickness, mold temperatures, and microstructure measurements. The breakout appears to be representative of normal casting conditions. The data collected from the breakout event was input into the CON1D mathematical model, to simulate and predict the growth of the breakout shell. The model incorporated mold heat fluxes calculated from a casting run that had similar process conditions, transient casting speed collected from the breakout event, and superheat flux profiles obtained from a CFD model of the submerged entry nozzle. Shell growth predictions based on local solidification times within the shell matched well with the breakout shell measurements, even close to the meniscus.

5.4 Future Work

This work has focused on incorporating experimental and measured plant data into mathematical models, to quantify the effect of interfacial heat transfer in the continuous casting process. Although the present findings help to understand what occurs in the casting mold, more analysis is needed in order to fully understand the behavior of the interfacial gap. Some suggestions are:

- Include the effect of mold flux latent heat in the interface heat transfer model within CON1D,
- Investigate flux behavior due to varying process parameters, such as mold heat flux and oscillation, in relation to their TTT diagrams,
- Complete detailed analysis of mold powder experimental data, in order to fully characterize the effect of plate distortion on flux thermal properties,
- Perform additional mathematical predictions of shell growth based on breakout shell measurements, for various casting runs and mold temperature/heat flux profiles

Further investigation into these tasks will facilitate a thorough understanding of interfacial heat transfer within the continuous casting process.

Appendix A: CON1D Version 4.1 Sample Input File

CON1D-4.1 Slab Casting Heat Transfer Analysis
University of Illinois, Brian G. Thomas, 1998
Armco breakout shell;transient analysis;z=252.63 mm;given heat flux curve
ta03 Input Data INP

(1) Casting Conditions:
7 Number of time-cast speed data points
(If=1, constant speed)
Next 2 lines contain time(s) and vc(m/min) data points
0. 10. 15. 20. 25. 30. 35.
1.524 1.524 1.4986 1.1938 0.7874 0.381 0.03
1563.000 Pour temperature (C)
132.1000 Slab thickness (mm)
984.0000 Slab width (mm)
1096.000 Working mold length (mm)
1090.000 Z-distance for heat balance (must be in mold) (mm)
127.0000 Nozzle submergence depth (mm)
1 Spray conditions (1=normal; 2=minimum)

(2) Simulation Parameters:
0 Which shell to consider? (0=wide face; 1=narrow face)
2 Which mold face to consider(0=outer, 1=inner,
2=straight mold or narrow face)
-1 Calculate mold and interface (=0)
or enter interface heat flux data (=1 or -1 :faster)
9 Number of z and q data points (if above = 1 or -1)
Next 2 lines contain z(mm) and q(kW/m2) data
0. 100. 200. 300. 410. 600. 800. 950. 1100.
2850. 2000. 1610. 1240. 1450. 1290. 1020. 830. 620.
-1.0000 Is superheat treated as heatflux?
0=no; 1=yes (take default);-1=yes (enter data)
11 Number of z and q data points (if above = -1)
Next 2 lines contain z(mm) and q(kW/m2) data
0. 16.4 124.3 196.2 340. 375.9 411.8 555.6 699.4 843.2 987.1
0. 23.6 219.8 570. 2139.9 2260.2 2097.3 646.3 260.1 125.7 66.1
1 Do you want (more accurate) 2d calculations
in mold? (0=no; 1=yes)
100.0000 Max. dist. below meniscus for 2d mold calcs (mm)
1.000000E-02 Time increment (s)
100 Number of slab sections
5.000000 Printout interval (mm)
0.000000E+00 Start output at (mm)
2000.000 Max. simulation length (mm)
66.00000 Max. simulation thickness (mm)
(smaller of max. expected shell thickness &
half of slab thickness)
25000 Max. number of iterations

0.000000 Shell thermocouple position below hot face (mm)
0.8000000 Fraction solid for shell thickness location (-)

(3) Steel Properties: (grade 434-20, heat 861515)
0.055 0.5 0.003 0.0350 0.40 %C,%Mn,%S,%P,%Si
16.4 0.500 0.000 1.05 0.201 %Cr,%Ni,%Cu,%Mo,%Ti
0.0500 0.000 0.06 0.0000 0.0000 %Al,%V,%N,%Nb,%W
0.0000 0.0000 0.0000 0.0000 0.0000 %Co,(additional components)
430 Grade flag (1000,304,316,317,347,410,420,430,999)
(carbon steels,..AISI stainless steels..,user subroutine)
0 Use segregation model to modify carbon steel
liquidus? (0=no, -1=yes)
Override defaults with following constants
(-1=default)
-1.00000 Steel liquidus temperature (C)
-1.00000 Steel solidus temperature (C)
7.270000 Steel density (g/cm^3)
304.0000 Heat fusion of steel (kJ/kg)
0.800000 Steel emissivity (-)
-1.00000 Steel specific heat(kJ/kg deg K)
-1.00000 Steel thermal conductivity(W/mK)
-1.00000 Steel thermal expansion coefficient (-)

(4) Spray Zone Variables:
25.00000 Water and ambient temperature in spray zone(Deg C)
5 Number of zones

No.	Zone starts at (mm below top)	#of rolls in zone	Roll radius (m)	Water flux (l/m^2)	Fraction of q thru roll
1	1096.000	1	0.05	14.059	0.010
2	1176.000	1	0.075	7.246	0.010
3	1331.000	5	0.075	3.937	0.080
4	2240.000	5	0.075	3.937	0.220
5	13640.000	30	0.222	0.950	0.360

14000.000 End of last spray zone

(5) Mold Flux Properties: (M662-C20)
39.2 38.4 3.4 2.0 0.6 %CaO,%SiO2,%MgO,%Na2O,%K2O
0.0 0.70 0.0 1.3 0.0 %FeO,%Fe2O3,%NiO,%MnO,%Cr2O3
5.0 0.0 0.0 0.0 1.4 %Al2O3,%TiO2,%B2O3,%Li2O,%SrO
0.0 9.3 1.8 2.6 2.8 %ZrO2,%F,%free C,%total C,%CO2
1084.05 Mold flux solidification temperature(C)
1.4300 Solid flux conductivity(W/mK)
1.43000 Liquid flux conductivity(W/mK)
2.210000 Flux viscosity at 1300C (poise)
2700.000 Mold flux density(kg/m^3)
200.0000 Flux absorption coefficient(1/m)
-1.0000 Flux index of refraction(-)

(-1 = take default f(composition))
0.9 Slag emissivity(-)
3.089508 Exponent for temperature dependency of viscosity
1 Form of mold powder consumption rate
(1 = kg/m^2; 2 = kg/t)
0.2000000 Mold powder consumption rate
0.0000E+00 Location of peak heat flux (m)
0.0040000 Slag rim thickness at metal level (m)
1.0000E-02 Slag rim thickness above heat flux peak (m)

(6) Interface Heat Transfer Variables:
1 Number of distance-ratio data points
(1=constant ratio of solid flux velocity
to casting speed)
Next 2 lines contain z(mm) and vratio (-) data
0. 120. 220. 315. 440. 660. 870.
0.1 0.05 .05 .05 .1 .05 .07
4.3000E-09 Flux/mold contact resistance(m^2K/W)
0.500000 Mold surface emissivity(-)
5.99999E-02 Air conductivity(W/mK)
0.00000000 Oscillation mark depth (mm)
0.000000 Width of oscillation mark (mm)
3.942 Oscillation frequency (cps)
(-1 = take default cpm=2*ipm casting speed)
5.130000 Oscillation stroke (mm)

(7) Mold Water Properties:
0.6403700 Water thermal conductivity (W/mK)(-1 = default = f(T))
4.000E-04 Water viscosity (Pa-s)(-1 = default = f(T))
4186.800 Water heat capacity (J/kgK)(-1 = default = f(T))
990.0000 Water density (kg/m3)(-1 = default = f(T))

(8) Mold Geometry:
35.00000 Mold thickness including water channel (mm),(outer rad.,top)
35.00000 Mold thickness including water channel (mm),(inner rad.,top)
104.0000 Distance of meniscus from top of mold (mm)
31.00000 Distance between cooling water channels(center to center)(mm)
315.0000 Mold thermal conductivity(W/mK)
37.75000 Cooling water temperature at mold top(C)
0.620000 Cooling water pressure(MPa)
10.000000 Cooling water channel depth(mm)
6.00000 Cooling water channel width(mm)
1 Form of cooling water flowrate/velocity(1=m/s ; 2=L/s)
-11.6690 Cooling water flowrate per channel / velocity
(> 0 cooling water from mold top to bottom
< 0 cooling water from mold bottom to top)
1.000000E+04 1.00000E+04 Machine radius(m) (outer &inner radius)

11 Number of mold coating/plating thickness changes down mold

No.	Scale	Ni	Cr	Others	*Air gap	Z-positions	unit
1	0.000	1.000	0.100	0.000	0.000	0.000	(mm)
2	0.000	1.050	0.100	0.000	0.000	100.000	(mm)
3	0.000	1.100	0.100	0.000	0.000	200.000	(mm)
4	0.000	1.150	0.100	0.000	0.00	300.000	(mm)
5	0.000	1.200	0.100	0.000	0.0	400.000	(mm)
6	0.000	1.250	0.100	0.000	0.00	500.000	(mm)
7	0.000	1.300	0.100	0.000	0.0	600.000	(mm)
8	0.000	1.350	0.100	0.000	0.00	700.000	(mm)
9	0.000	1.400	0.100	0.000	0.0	800.000	(mm)
10	0.000	1.450	0.100	0.000	0.00	900.000	(mm)
11	0.000	1.500	0.100	0.000	0.0	1096.000	(mm)
0.550	72.100	67.000	1.000	0.060	Conductivity	(W/mK)	

0.250000 *Factor to approximate nonlinear heat flow at meniscus,(first guess for 2d analysis)
4.9999999E-03 6.4999998E-02 Equivalent inner and outer radius for meniscus heatflow aprox. (mm)

(9) Mold Thermocouples:
6 Total number of thermocouples (space here for t.c. location)

No.	Distance beneath hot surface(mm)	Distance below meniscus(mm)
1	24	121
2	24	226
3	24	321
4	24	446
5	24	666
6	24	876

REFERENCES

1. Huang, X. and B.G. Thomas, *Modeling of Steel Grade Transition in Continuous Slab Casting Processes.* Metall. Trans., 1993. **24B**: p. 379-393.
2. Thomas, B.G., D. Lui, and B. Ho, *Effect of Transverse and Oscillation Marks on Heat Transfer in the Continuous Casting Mold*, in *Applications of Sensors in Materials Processing*, V. Viswanathan, Editor. 1997, TMS, Warrendale, PA: Orlando, FL. p. 117-142.
3. Jenkins, M.S., *Characterisation of Heat Transfer in a Continuous Casting Mold*, in *Steelmaking Conference Proceedings*. 1995, Iron and Steel Society: Warrendale, PA. p. 315-320.
4. Wolf, M.M., *Mold Heat Transfer and Lubrication Control - Two Major Functions of Caster Productivity and Quality Assurance*, in *Continuous Casting*. 1997, Iron and Steel Society: Warrendale, PA. p. 211-229.
5. Emi, M., *The Mechanisms for Sticking Type Breakouts and New Developments in Continuous Casting Mold Fluxes*, in *Steelmaking Conference Proceedings*. 1991, Iron and Steel Society: Warrendale, PA. p. 639-646.
6. Susa, M., *et al.*, *Thermal properties of slag films taken from continuous casting mould.* Ironmaking and Steelmaking, 1994. **21**(4): p. 279-286.
7. Stewart, D., P.N. Hewitt, and L. Peeters, *The Prediction of Longitudinal Cracking During Slab Casting*, in *Steelmaking Conference Proceedings*. 1996, ISS, Warrendale, PA: Pittsburgh, PA. p. 207-214.

8. Kumar, S., I.V. Samarasekera, and J.K. Brimacombe, *Mold Thermal Response and Formation of Defects in the Continuous Casting of Steel Billets, Part 2: Rhomboidity.* Iron and Steelmaker (ISS Transactions), 1998. **25**(12): p. 51-66.

9. Hiraki, S., *et al.*, *Influence of Mold Heat Fluxes on Longitudinal Surface Cracks During High Speed Continuous Casting of Steel Slab*, in *Steelmaking Conference Proceedings*. 1994, Iron and Steel Society: Warrendale, PA. p. 397-403.

10. Bommaraju, R. and E. Saad, *Mathematical modelling of lubrication capacity of mold fluxes*, in *Steelmaking Proceedings*. 1990, Iron and Steel Society: Warrendale, PA. p. 281-296.

11. DiLellio, J.A. and G.W. Young, *An Asymptotic Model of the Mold Region in a Continuous Steel Caster.* Metallurgical and Materials Transactions B, 1995. **26B**(6): p. 1225-1241.

12. Thomas, B.G., B. Ho, and G. Li, *CON1D User's Manual*, . 1994, University of Illinois.

13. Gittler, P. and M. Brummayer, *Numerische Simulation der Stromungsverhaltnisse in Einer Kikille*, . 1997, Johannes Kepler Universitat, Linz, Austria.

14. Sleicher, C.A. and M.W. Rouse, *A convenient correlation for heat transfer to constant and variable property fluids in turbulent pipe flow.* Int. J. Heat Mass Transfer, 1975. **18**: p. 677-683.

15. Ho, B., *Characterization of Interfacial Heat Transfer in the Continuous Slab Casting Process*, . 1992, University of Illinois at Urbana-Champaign.

16. Susa, M., K. Nagata, and K.C. Mills, *Absorption coefficients and refractive indices of synthetic glassy slags containing transition metal oxides.* Ironmaking and Steelmaking, 1993. **20**(5): p. 372-378.

17. Hills, A.W.D., *Simplified theoretical treatment for the transfer of heat in continuous-casting machine moulds.* Journal of The Iron and Steel Institute, 1965: p. 18-26.

18. Mikrovas, A.C., S.A. Argyropoulos, and I.D. Sommerville, *Heat transfer characteristics of molten slags.* Ironmaking and Steelmaking, 1991. **18**(3): p. 169-181.

19. Mills, K.C., *et al.*, *Physical properties of casting powders: Part 4 Physical properties relevant to fluid and thermal flow.* Ironmaking and Steelmaking, 1988. **15**(5): p. 257-264.

20. Stone, D.T. and B.G. Thomas, *Measurement and Modeling of Heat Transfer Across Interfacial Mold Flux Layers.* Canadian Metallurgical Quarterly, 1999. **38**(5): p. 363-375.

21. Ohmiya, S., K.-H. Tacke, and K. Schwerdtfeger, *Heat Transfer through layers of casting fluxes.* Ironmaking Steelmaking, 1983. **10**(1): p. 24-30.

22. Taylor, R. and K.C. Mills, Archive fur Eissenhuttenwessen, 1982. **53**: p. 55-63.

23. Susa, M., F. Li, and K. Nagata, *Thermal conductivity, thermal diffusivity, and specific heat of slags containing iron oxides.* Ironmaking and Steelmaking, 1993. **20**(3): p. 201-206.

24. Jenkins, M.S., *Characterisation and Modification of the Heat Transfer Performance of Mold Powders*, in *Steelmaking Conference Proceedings*. 1995, Iron and Steel Society: Warrendale, PA. p. 669-677.

25. Yamauchi, A., *et al.*, *Heat Transfer between Mold and Strand through Mold Flux Film in Continuous Casting of Steel.* ISIJ International, 1993. **33**(1): p. 140-147.

26. Rohsenow, W.M., *Handbook of Heat Transfer*. 3rd ed. 1998: McGraw-Hill.

27. DeSalvo, G.J. and R.W. Gorman, *ANSYS, Rev. 4.3*, . 1987, Swanson Analysis Systems, Inc.: Evanston, IL.

28. Kashiwaya, Y., C. Cicutti, and A.W. Cramb, *Crystallization Behavior of Mold Slags*, in *Steelmaking Conference Proceedings*. 1998, Iron and Steel Society: Warrendale, PA. p. 185-191.

29. Thomas, B.G. *Measurement of Temperature, Solidification, and Microstructure in a Continuous Cast Thin Slab*. in *Modeling of Casting, Welding, and Advanced Solidification Processes VII*. 1997. San Diego, CA.

30. Callmer, B. and O. Grinder, *On the Solidification of Low Interstitial Ferritic Chromium Steels.* Scand. J. Metallurgy, 1980. **9**.

31. Moitra, A. and B.G. Thomas, *Application of a Thermo-Mechanical Finite Element Model of Steel Shell Behavior in the Continuous Slab Casting Mold*, in *Steelmaking Proceedings*. 1993, Iron and Steel Society: Dallas, TX. p. 657-667.

32. Creech, D., *Computational Modeling of Multiphase Turbulent Fluid Flow and Heat Transfer in the Continuous Slab Casting Mold*, in *Mechanical Engineering*. 1998, University of Illinois at Urbana-Champaign.